



# Advances in Optics and Photonics

## Computational imaging

JOSEPH N. MAIT,<sup>1,\*</sup> GARY W. EULISS,<sup>2</sup> AND RAVINDRA A. ATHALE<sup>3</sup>

<sup>1</sup>U.S. Army Research Laboratory, RDRL-D, 2800 Powder Mill Road, Adelphi, Maryland 20783, USA

<sup>2</sup>The MITRE Corporation, 7515 Colshire Drive, McLean, Virginia 22102, USA

<sup>3</sup>Office of Naval Research, 875 N. Randolph Street, Suite 1425, Arlington, Virginia 22203-1995, USA

\*Corresponding author: joseph.n.mait2.civ@mail.mil

Received January 2, 2018; revised April 27, 2018; accepted April 30, 2018; published May 22, 2018 (Doc. ID 318379)

We review advances in Computational Imaging that have occurred since the mid-1990s. The advent of highly integrated platforms, such as the smartphone, has made the linkage between optics and processing intimate and natural. This review covers key technological developments and insights over the past two decades and examines current trends to predict future capabilities.

OCIS codes: (110.1758) Computational imaging; (110.0110) Imaging systems  
<https://doi.org/10.1364/AOP.10.000409>

1. Introduction . . . . .	411
2. Sensing, Imaging, and Photography . . . . .	411
3. Short History of Imaging . . . . .	412
3.1. Antiquity . . . . .	413
3.2. Aided Human Imaging: the Beginning of Image Science . . . . .	413
3.3. Recorded Imaging: Image Science Matures and Imaging Applications Multiply . . . . .	414
3.4. Electronic Imaging . . . . .	415
4. Computational Imaging . . . . .	416
4.1. Definition . . . . .	416
4.2. Physical and Mathematical Essentials . . . . .	418
4.3. Optical Design . . . . .	423
4.3a. Decoupled . . . . .	423
4.3b. Collaborative . . . . .	424
4.3c. Integrated . . . . .	424
4.4. Information Essentials . . . . .	425
4.5. Motivations . . . . .	428
5. Motivation 1: Conventional Imaging Is Impossible . . . . .	428
5.1. Phase Imaging . . . . .	428
5.1a. Phase Contrast Microscope . . . . .	429
5.1b. Interferometry and Holography . . . . .	430
5.1c. Phase Retrieval from Magnitude . . . . .	431
5.2. Quantum Imaging . . . . .	433
5.3. Volumetric Imaging . . . . .	434
5.3a. Computed Tomography . . . . .	435

5.3b. Magnetic Resonance Imaging . . . . .	436
6. Motivation 2: Dimensionality Mismatch . . . . .	437
6.1. Spatial–Spectral Imaging . . . . .	437
6.2. Three-Dimensional Imaging . . . . .	441
6.2a. Depth-Invariant Imaging . . . . .	441
6.2b. Depth Measurement . . . . .	443
6.3. Polarization Imaging . . . . .	446
7. Motivation 3: Reducing Measurement Marginal Costs . . . . .	448
7.1. Possible but Impractical . . . . .	449
7.1a. Synthetic Aperture Radar . . . . .	449
7.1b. Coded-Aperture Imaging . . . . .	450
7.2. Possible but Not Optimal . . . . .	451
7.2a. Superresolution . . . . .	452
7.2b. Increased Temporal Resolution . . . . .	455
7.2c. Form Factor Constraints . . . . .	456
7.2d. Feature-Specific and Compressive Imaging . . . . .	459
7.3. Adaptive Systems . . . . .	463
7.3a. Adaptive Optics . . . . .	463
7.3b. Adaptation-Based on Information . . . . .	465
7.3c. Adaptive Lidar . . . . .	465
8. Future of Computational Imaging . . . . .	466
8.1. Strengths . . . . .	466
8.2. Weaknesses . . . . .	466
8.3. Opportunities . . . . .	468
8.4. Threats . . . . .	470
9. Conclusion and Summary Remarks . . . . .	470
Acknowledgment . . . . .	471
References . . . . .	472

# Computational imaging

JOSEPH N. MAIT, GARY W. EULISS, AND RAVINDRA A. ATHALE

## 1. INTRODUCTION

In the past decade, smartphone technology has placed more cameras in hands across the globe than were ever available in the previous four centuries. For good or ill, it is now possible to live-stream any event with the click of a button. Consider the unique circumstances of Zapruder's filming the Kennedy assassination over 50 years ago in comparison to how citizens capture breaking news events today. The advancements in imaging witnessed over the past 50 years have resulted from a more intimate coupling between physics and technology than had previously been possible.

In the mid-1990s, this integration revealed to many researchers in the optics and image processing community (including us) a new paradigm in imaging, one in which the burden of image formation was no longer borne solely by optical physics. A key feature of this paradigm, now referred to as Computational Imaging, is the joint design of the front-end optics and post-detection signal processing. In some instances, the measurements made by the optics may not even resemble an image. Using principles of Computational Imaging, one can design an instrument to make optical measurements from which images, and other scene information, can be derived with a capacity that far exceeds the physical limits of the optics. Equivalently, Computational Imaging enables the design of instruments that, when compared to a conventional approach, provide a desired capability with reduced requirements in size, weight, power, or cost.

In this paper, we review the expanding field of computational imaging. We begin our review in Section 2 with basic information about sensing and imaging. This provides definitions that delineate computational imaging from other closely related disciplines, such as remote sensing, photography, and image enhancement and recovery. We follow this in Section 3 with a brief history of imaging up to 1990. Most of the material in this section is from Ref. [1]. We introduce the essentials of computational imaging in Section 4. We begin with the physics of image formation, consider detection and post-processing, and close with an information theory perspective of imaging. This perspective leads us to introduce three categories of Computational Imaging systems in Sections 5–7. The systems are distinguished by their motivations for relying upon computation to create an image. In each section, we present imagers that exemplify the particular motivation and illustrate a Computational Imaging principle. Our examples are selected to be representative and not exhaustive. We also do not attempt to assess the value of one implementation against another. Section 8 assesses computational imaging in terms of its present strengths and weaknesses, and its future opportunities and threats. We present our summary and concluding remarks in Section 9.

## 2. SENSING, IMAGING, AND PHOTOGRAPHY

The broad field in which Computational Imaging resides is sensing. Sensing is the measurement and estimation of some physical property in an environment. Consider, for example, a thermometer placed outside a window. The thermometer measures (senses) the temperature of the air at a single point. Whereas lay people have no problem extrapolating that measurement to the large space outside their window, a meteorologist may want more information. Meteorologists know that a temperature differential between two points produces air currents. If the differential is sufficiently large, the currents could be harmful to life and property. Thus, the meteorologist needs

to know the spatial distribution of temperatures over a region. We refer to this spatial map of temperature as a thermal image.

We categorize measurements made without reference to a spatial map as sensing. In contrast, we refer to the measurement and estimation of an environmental property in multiple locations as imaging. One forms an image for one of two reasons. Either, as just described, one wishes to estimate the spatial map of a physical property, or one wishes to classify elements of the environment into categories (e.g., stationary versus mobile, friend or foe, members of my family) [2].

With regard to the latter objective, we note that sometimes classification is meant to be evocative, for example, documenting an event or eliciting an emotion. We refer to such applications as photography or cinematography to distinguish them from more objective applications and to distinguish Computational Imaging from Computational Photography, a field of research unto itself [3,4]. The distinction between imaging and cinematography was made poignantly clear in a presentation by Hollywood cinematographer John Schwartzman at The Optical Society's (OSA) 2017 Imaging Congress [5].

We note that in photography, the optics always maps the luminance or chrominance at every point in object space to a point in image space. Further, the mapping maintains the spatial relationship between object points in the image. For other imaging applications, the optics may perform a one-to-one mapping but is not required to do so.

These definitions delineate and narrow the applications that belong to computational imaging. In the next section, we present a brief history of imaging and image science to provide perspective for our review. We note that the Eurocentric focus of our history reflects the historical evidence that the microscope and telescope were invented in Europe.

### 3. SHORT HISTORY OF IMAGING

Image science is grounded in the scientific principle of refraction, first reported by Snell in 1621. It is also grounded in two engineering principles, the Lensmaker's Formula derived by Cavalieri in 1647 and the Imaging Equation derived by Newton in 1670.

We ground image science exclusively on refraction, and not reflection, deliberately. Although the Romans knew how to make mirrors and knew also that the angle of reflection is equal to the angle of incidence, this understanding did not lead to the wide-scale development of multi-element imaging systems. Understanding how light refracts through glass led to an understanding of the lens and its critical importance to imaging. Only subsequently did Newton and others consider imaging systems based on reflection.

Since these beginnings, imaging has progressed through advances in four essential technologies: optical materials, such as glass and polymers; transducers other than the human eye, which include film and electronic detectors; sources, ranging from candles, arc lamps, and incandescent bulbs to LEDs and lasers; and, finally, processing via biology, electronics, or some other technology. All imagers produced today are built on the foundations of these technologies.

In this section, we identify five imaging periods. We delineate them by the level of understanding existent in the technical community at the time and the availability of technology. Four of these we discuss here. The last, Computational Imaging, is the focus of this article. Our proposed dates for each era are rough demarcations and are not meant to be hard and fast.

The first period is Antiquity. During this period, even though glass was available, artisans lacked the knowledge and understanding of how to use it for more than decoration, windows, or structural items like plates and cups.

The next period, which extends approximately from 1600 to 1840, represents the beginnings of optical science and engineering. This is when multi-lens microscopes and telescopes extended human vision into the macro- and microcosms of our universe. This is the period of aided human imaging.

We refer to the period between 1840 and 1970 as the era of photochemical-based recorded imaging and that between 1970 and 1990 as the era of digital-electronic recorded imaging. As a shorthand, we refer to the former as the period of recorded imaging and the latter as the period of electronic imaging. It is during the period of recorded imaging that the nature of light was revealed and the limitations physics imposes on image formation were understood. The most fundamental of these is the resolution limit, and many advances in imaging during this period were driven by a desire to meet or exceed this limit using optical means.

Finally, we refer to the period beyond 1990 as that of Computational Imaging. This is when computation is included in the design of optical imaging systems as a general matter of course. To aid in the co-design of optics and post-detection signal processing, resolution was re-interpreted as a measure of the information a wavefront can convey through a finite aperture. This led to new methods of optical encoding and post-processing.

### 3.1. Antiquity

Reflection, refraction, and the ability of an appropriately shaped crystal to magnify an image were all observed in antiquity. Euclid's *Catoptrics*, written circa 300 Before Common Era (BCE), correctly notes the angle of reflection is equal to the angle of incidence. Refraction, on the other hand, was observed but not understood.

Spectacles, the first practical optical instrument, appeared in 1270 in Florence, Italy. However, spectacles do not represent an advancement in optics as much they do an advancement in packaging. As evidenced by the writings of Bacon, Europeans were aware of a lens' ability to magnify images. Spectacles are unique for their application of a metal frame to hold two lenses in front of a person's eyes.

The appearance in 1270 of a Latin translation of Alhazen's *Opticae Thesaurus*, written at the turn of the first millennium, provided comments on imaging phenomena but a clear understanding of refraction eluded the Europeans. For example, Vitello, a Polish mathematician studying in Italy, published a compendium of measured refracted angles in 1270. Unfortunately, his work was fraught with errors.

Given the presence of spectacles and projectors like the magic lantern in the early renaissance, it is puzzling that the development of the first multi-element optical instrument did not occur before the 16th century.

### 3.2. Aided Human Imaging: the Beginning of Image Science

In 1590, the father and son team Hans and Zacharias Janssen introduced the compound microscope, a two-element optical system. Within 20 years of the microscope's invention, Lippershey and Galileo introduced two different telescope types, and Lippershey developed the binocular as well.

Kepler's *Dioptre*, published in 1611, and Antonio Neri's *L'arte vetraria* (The Art of Glass), published in 1612, provided the means and motivation for widespread optical design. Kepler provided the basics of first-order optics. Neri revealed the proper proportions of sodium, lime, and silicates needed to manufacture high-quality glass.

Kepler's publication contains the first analysis of multi-lens systems. It also reveals a fundamental lack of understanding of refraction. Lacking a general law of refraction, Kepler restricted his analysis to small angles.

Snell's Law of Refraction, established in 1621, is the key that unlocked optical design. With it, Descartes derived the shape of a lens capable of correcting spherical aberration. In 1647, Cavalieri linked the focal length of a lens to the curvatures of the lens' surfaces and refractive index in what we now refer to as the Lensmaker's Formula. Finally, around 1670, Newton derived the Imaging Equation, a keystone in optical design that relates the focal length of a lens to the distance between it and its object and image planes.

The appearance in 1662 of an English translation of Neri's book may have affected the work of British glassmaker George Ravenscroft, whose decision to add lead to the chemical composition of glass had a significant impact on optical glass. In 1674, Ravenscroft patented a method for making flint glass. In 1733, amateur astronomer Hall used the disparate dispersion properties of crown and flint glasses to correct chromatic aberrations.

Much later, in 1809, Fraunhofer experimented with the material composition of glass while working at a Bavarian glass melting workshop. Consequently, Fraunhofer not only produced high-quality achromats, he characterized the dispersive properties of different glass compositions using his nascent spectroscopic techniques.

In 1800, using a thermometer to measure the temperature of colors dispersed by a prism, Herschel discovered warm radiation (calorific rays) beyond the red spectrum. Further, presaging the invention of film, in 1801, Ritter exposed silver chloride to dispersed sunlight and detected so-called chemical rays beyond blue. Thus, Herschel and Ritter established the existence of radiation beyond what is visible to the human eye.

### 3.3. Recorded Imaging: Image Science Matures and Imaging Applications Multiply

The invention of recorded imaging in 1837 by Daguerre had a significant impact on imaging applications. Images from the aftermath of American Civil War battles established dramatically the power of photography to be evocative, not just narrative. Film led not just to the development of photography but also to cinematography.

From our perspective, the invention of film allowed images to be captured without the need for a human observer. This is especially true of the first examples of remote sensing, namely, the kite-borne aerial photographs taken by British meteorologist Douglas Archibald in 1887 and the Frenchman Arthur Batut in 1888.

The invention of film allowed others to record events too fast and too slow for human perception. In 1872, Eadweard Muybridge settled the question put to him by Leland Stanford about horse motion. Using an array of 12 cameras, Muybridge showed that, at one point during a trot, all four feet of a horse are off the ground at the same time. Time-lapse photography was pioneered by F. Percy Smith in 1910 to document the progression of flowers as they bloom.

During this period, physicists established the nature of light. The question had vexed philosophers for millennia and had been a controversial topic within the technical community for nearly two and a half centuries. In the 17th century, Newton, on one side, proclaimed that light was a particle, which influenced the community for many years. However, Huygens believed it was a wave. Grimaldi's diffraction experiments published in 1665 and Young's demonstration of light interference in 1801 bolstered the wave nature of light. This was validated with mathematical models for diffraction and polarization, and culminated in 1865 with Maxwell's Equations.

The wave nature of light held sway until physicists revealed the quantum nature of matter and turned the argument of waves versus particles on its head. This eventually yielded the Copenhagen Interpretation of Quantum Mechanics.

It is also during this period that optical science developed into optical engineering. Armed with a deeper understanding of optical physics, the optics community was poised in the 1870s to make significant strides in imaging. These advances were realized through a partnership of theory, application, and materials expertise embodied by Abbe, Zeiss, and Schott. Abbe's 1873 wave optical interpretation of image formation established limits on imaging performance but also enabled a non-materials-based improvement to optical imaging [6].

At the same time, Abbe and Schott studied the relationship among materials, their proportions, and their influence on optical properties. Consequently, 19 of the 44 glasses described in the first Schott catalog in 1886 were new. Two years later, their first catalog supplement included 24 more new glass types. The confluence of physical understanding and materials moved optics into the realm of engineering and made Zeiss an international leader in optical instruments.

### 3.4. Electronic Imaging

Perhaps the most powerful advance in the 20th century was the marriage of the physicist's elementary particles (the electron and the photon) with Shannon's elementary particle of information (the bit). Shannon's theory of information [7], which emerged in the late 1940s, did much to influence how people thought about images, the imaging process, and optical systems in general [8–12]. At the same time, the application of Fourier analysis to optical systems had recently been introduced by Duffieux [13]. The melding of optics and information theory was prominently represented in Goodman's classic text on Fourier Optics, which appeared in 1968 [14].

In the early 1960s, when electronic processing was analog, one-dimensional, and was still realized primarily using discrete components, optics offered considerable advantages in throughput and parallel processing. The invention of the laser in combination with off-axis holography heralded the dominance of optics over electronics for imaging and image processing [15–17].

This dominance was short-lived. The invention of the charged coupled device (CCD) detector in 1969 contributed to a shift away from optical processing [18,19]. Electronic transduction allowed optical images to be transformed in real time into an electronic format, to which one can apply analog and digital electronic processing. The electronic format also facilitated image transmission and storage.

The impact of the near contemporaneous release of Cooley and Tukey's Fast Fourier Transform algorithm [20], the CCD [18,19], and the Intel 4004 microprocessor [21] is comparable to that of Kepler's *Dioptrice* and Neri's *L'arte vetraria*. Together, the three provide the motivation, means, and method to perform digital electronic processing of images. For the first time, images were formed that could be consumed strictly by computers and never viewed by a human.

The potential for further advances in digital imaging is often referenced to Moore's law—that the number of transistors per area in an integrated circuit doubles every 18 months. However, the fervor with which Moore's Law is so often repeated can lead to a skewed view of the future of imaging and imaging systems. What do the optics provide? Are they necessary at all? Naturally, we feel optics are necessary, and, in the remainder of this article, we address how optics and electronics can be used together to create instruments that are more powerful than either alone.

#### 4. COMPUTATIONAL IMAGING

Computational Imaging attempts to balance the processing capabilities of optics and electronics through concurrent design and joint optimization of all elements. The individual elements are not considered independent of one another.

We acknowledge in our prior work [22], and again in this review, that antecedents to Computational Imaging existed prior to 1990. Thus, setting 1990 as the beginning of the field appears arbitrary and contradictory to the facts. However, despite the existence of earlier work that applied some of the fundamental concepts we highlight here, it was not until the 1990s that the imaging community began to see these individual solutions to imaging problems as reflective of a fundamental shift in approach. Computation was becoming an explicit and integral part of imaging.

One of the first references to a general joint optical–computational approach to imaging is the seminal work of Cathey *et al.* [23], which discusses how one can increase the resolution or otherwise enhance an electronically detected image through joint design of the optics and signal processing. One of the first demonstrations of the advantages of such an approach was presented by Matic and Goodman [24–26]. When filtering an image, they showed an improvement in noise performance when the filter function was distributed across the optics and post-detection processing. A paper by Veldkamp [27] attempted to give this field a name, amacronics, based on the amacrine layer in the human eye. The amacrine layer pre-processes visual information before it is launched onto the optic nerve. The name did not catch on. Perhaps it was too early for the field to be recognized as something new.

Nonetheless, as exemplified by the pioneering work of Cathey and Dowski to increase imager depth-of-field [28–30], a small community of researchers in the mid-1990s started publishing work in which optical information is formatted or encoded explicitly with post-detection processing in mind [31–34].

This activity prompted one of us (JNM) to organize an Army-sponsored workshop [35] and, subsequently, The Optical Society’s first topical meeting on Computational Imaging [36]. Growth in the nascent Computational Imaging community was also assisted by workshops sponsored by Prof. David Brady of Duke University in 1998 and 2000.

What to call this approach to imaging was discussed in those first meetings [35,36], and reference to image gathering in their names reflects the influence of [23]. Our first use of the term Computational Imaging appears in Ref. [37], “an integrated computational imaging system … is one whose design integrally incorporates optics, optoelectronics, and signal processing. System performance is controlled through concurrent design and joint optimization, as opposed to sequential design and independent optimization of the optics, focal plane optoelectronics, and post-detection algorithm.” In the next two sections we attempt to put this definition on firmer ground.

##### 4.1. Definition

In Section 2, we distinguished sensing from imaging. Imaging connotes a spatial map, whereas sensing does not. To define Computational Imaging, we need to make an additional distinction that depends upon the relationship between the location at which a measurement is made and the location of the source information one wishes to measure.

When these two locations are coincident, we refer to the sensing as embedded or proximate. Proximate sensing employs transduction mechanisms to sense and measure the physical parameters of interest at the location of the transducer. Examples include thermocouples to measure temperature at a point in space and surface profilers that scan probes in contact with a sample.

When the locations of the source information and the measurement are not coincident, we refer to the sensing or imaging as standoff or remote. Standoff imaging involves wave phenomena to convey energy and information through space without material movement. Although our review considers only electromagnetic wave phenomena, mechanical waves (e.g., acoustic and seismic waves) and, as shown recently, gravitational waves can also convey information remotely.

Since electromagnetic wave propagation through free space intrinsically involves diffraction, information about the spatial location of physical parameters we wish to measure are scrambled. Consequently, recovering this information requires processing, which, as shown in Fig. 1, can occur in a front-end system prior to transduction or in post-transduction.

As defined above, sensing and imaging systems with no pre- or post-detection processing are proximate. We do not consider these. Instead, we consider systems that employ pre-transduction processing, post-transduction processing, or both to form images.

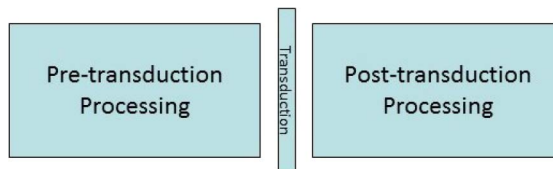
Systems that employ only pre-transduction processing are traditional imagers that use optics to transform incoming wavefronts. The transformations attempt to account for the effects of diffraction and recover the spatial organization of information in the object plane. As discussed in the previous section, this is historically the earliest form of an imaging system.

A second class of imagers has no engineered front-end yet still employ post-detection processing. The best example of such a system is a radar antenna array that operates in the radio frequency (RF) band of the electromagnetic spectrum. The scale of RF wavelengths makes lenses expensive to build and control mechanically. However, high-speed electronic amplifiers allow signals from an antenna array to be transduced and processed directly. Thus, spatial information can be recovered using analog and digital signal processing in post-detection. Ultrasonic imaging in biomedicine and seismic imaging in geology are other examples of systems that form images by processing signals directly from transducers.

The final class of imagers we consider employ both pre- and post-transduction processing. One can argue that imaging systems designed to aid human vision employ visual processing in the brain after transduction by the retina. However, we limit our discussion to systems whose post-transduction processing is designed and engineered by humans.

This class of imagers traces its origins to the period when photographic emulsion replaced the human retina as a transduction mechanism. In photography, by controlling the contrast and dynamic range of an emulsion via chemical processing, one can implement a degree of image processing. Opto-electronic transduction enables similar operations to be performed in real time. However, advancements in semiconductor

Figure 1



Representation of an imager from the perspective of pre- and post-transduction processing.

integrated technology improved both detector technology and the sophistication of post-transduction computation.

In the 1970s and 1980s, the communities interested in wavefront processing and in image processing were largely decoupled from one another. As noted in the introduction to this section, only later was the notion of joint design of wavefront processing and post-transduction computation recognized as a unique approach to extracting information from wavefronts.

The assumptions on the detected wavefront and the relationship these assumptions have to post-detection processing distinguish Computational Imaging from Electronic Imaging. The distinction is revealed in the constraints and *a priori* information applied post-detection. Post-detection processing that is agnostic to the physics that generated the measurements falls under Electronic Imaging and we label it image processing. In Computational Imaging, physics is integral to the measurement process and post-detection processing. The nature of priors is why we include phase retrieval [38–40] and compressive imaging [41] in Computational Imaging and do not include, for example, image segmentation algorithms that extract averages and variances without reference to how the measurements were made.

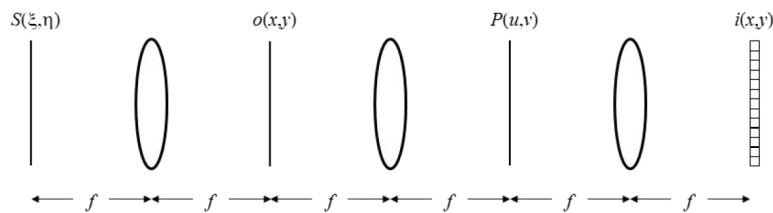
We reiterate that a distinguishing feature of a computational imager is its application of both pre- and post-transduction processing. Pre-transduction processing encodes or formats information we desire in a manner that simplifies its extraction post-transduction. Stating this another way, computational imagers make indirect measurements of a desired quantity as opposed to a direct one. We use this terminology, indirect versus direct measurements, in our review as a shorthand for Computational Imaging.

#### 4.2. Physical and Mathematical Essentials

A discussion of imaging requires a physical foundation and we present Fig. 2 as a canonical model of an imaging system with pre-transduction processing. The optical train includes both wavefront propagation from the object to the imager and transformation of the wavefront captured by the imager's optics. The system uses lenses with focal length  $f$  to form an output image  $i(x, y)$  of the two-dimensional input object  $o(x, y)$  onto a detector. The object is either self-luminous or illuminated by an external source. Our figure represents an illuminated object. The pupil function  $P(u, v)$  represents the transformation imposed by the optical system on the object. In its simplest form, the pupil function is a clear aperture with finite extent. However, more complex structures are possible.

To analyze the system in Fig. 2, we note that weighted superposition of wavefronts at a detector is the essence of imaging. The wavefronts carry information about the spectral content of self-luminous or illuminated objects located at different spatial

**Figure 2**



Schematic representation of an imaging system with pre-transduction processing. A source illuminates an object, whose transmitted wavefront is transformed by propagation and optical processing via the pupil function  $P(u, v)$  prior to detection.

locations. The physical properties of the light source and the object determine how this information is encoded on a wavefront and transduced by a detector.

If the physical processes that generate two wavefronts are correlated, the wavefronts can add coherently, i.e., in both amplitude and phase. If the processes are uncorrelated, the wavefronts are incoherent and it is their energies that add.

Wavefronts are characterized in terms of both spatial and temporal coherence. The degree to which wavefronts emitted at the same time from different spatial locations are correlated is referred to as the spatial coherence of the source. Spatial coherence is related to the extent of the source. Spatially small sources have higher spatial coherence than extended sources. Temporal coherence refers to the correlation between wavefronts from the same point at different times.

We note that the spatial coherence of an emitted wavefront measured in a plane other than the source can be different from the source coherence. Nonetheless, in the following, we reference coherence in the source plane. For further reference on coherence, we refer readers to Refs. [42,43].

The following analysis, based in large part on [44], grounds these notions about coherence and imaging. It assumes that light can be modeled as a scalar field. Key to this is satisfying the paraxial approximations. Our analysis further assumes that the imaged wavefront is generated by an external source illuminating an object. Only small changes are required for the case when an object is self-luminous, e.g., a star that radiates across the electro-magnetic spectrum or a warm engine that radiates primarily in the infrared (IR).

For future reference, we note that imaging in which one can control the illuminating source is referred to as active. In contrast, lack of control over illumination either because the object is self-luminous or is illuminated by an external source, such as the sun, is referred to as passive imaging.

With reference to Fig. 2, we assume an object  $o(x, y; \nu)$  is illuminated by a polychromatic, spatially structured source  $\tilde{s}(x, y; \nu)$  such that the transmitted wavefront  $\tilde{o}(x, y; \nu)$  is

$$\tilde{o}(x, y; \nu) = o(x, y; \nu)\tilde{s}(x, y; \nu), \quad (1)$$

where the temporal frequency  $\nu = c/\lambda$  and  $\lambda$  is wavelength. For transilluminated objects,  $\tilde{s}(x, y; \nu)$  is related to the Fourier transform of the source  $S(\xi, \eta; \nu)$  in Fig. 2. For self-luminous objects,  $\tilde{o}(x, y; \nu)$  remains an appropriate representation. The function  $\tilde{s}(x, y; \nu)$  represents the stochastic source of wavelength-dependent energy, e.g., thermal processes that regulate the temporal and spectral emission of photons, and  $o(x, y; \nu)$  is a deterministic function that describes the object's physical and geometric properties as a function of frequency.

Given the transmissive function  $P(u, v; \nu)$  in the pupil plane, the field in the image plane is a convolution between the transmitted wavefront and the coherent spread function (CSF)  $p(x, y)$ , which is the inverse Fourier transform of  $P(u, v; \nu)$ :

$$\begin{aligned} \tilde{i}(x, y; \nu) &= \tilde{o}(x, y; \nu) * p(x, y; \nu), \\ &= \int_{-\infty}^{\infty} \int_{-\infty}^{\infty} \tilde{o}(x', y'; \nu) p(x - x', y - y'; \nu) dx' dy', \end{aligned} \quad (2)$$

where  $*$  represents two-dimensional convolution. If we assume reduced coordinates, i.e.,  $f\lambda = 1$ , where  $f$  is the focal length of the lenses in Fig. 2,  $u$  and  $v$  are normalized spatial frequencies and

$$p(x, y; \nu) = \mathcal{F}^{-1}[P(u, v; \nu)]. \quad (3)$$

The temporal signal  $\tilde{i}(x, y; t)$  incident upon the detector is the sum of all frequency components contained in the source:

$$\tilde{i}(x, y; t) = \int_{-\infty}^{\infty} [\tilde{o}(x, y; \nu) * *p(x, y; \nu)] \exp(-j2\pi\nu t) d\nu. \quad (4)$$

An infinitesimal detector at a point  $(x, y)$  in space responds to the irradiance of the signal measured during an exposure time  $\tau$ :

$$\begin{aligned} i(x, y) &= \kappa \int_0^\tau |\tilde{i}(x, y; t)|^2 dt, \\ &= \kappa \int_0^\tau \left[ \int_{-\infty}^{\infty} \int_{-\infty}^{\infty} \int_{-\infty}^{\infty} \tilde{o}(x_1, y_1; \nu_1) p(x - x_1, y - y_1; \nu_1) R(\nu_1) \exp(-j2\pi\nu_1 t) dx_1 dy_1 d\nu_1 \right] \\ &\quad \times \left[ \int_{-\infty}^{\infty} \int_{-\infty}^{\infty} \int_{-\infty}^{\infty} \tilde{o}^*(x_2, y_2; \nu_2) p^*(x - x_2, y - y_2; \nu_2) R(\nu_2) \exp(j2\pi\nu_2 t) dx_2 dy_2 d\nu_2 \right] dt, \end{aligned} \quad (5)$$

where  $R(\nu)$  is the spectral response of the detector, which is real valued. The constant  $\kappa$  is a scale factor necessary to convert the incident electromagnetic field quantity represented in the integrand to an electronic quantity output by the detector.

We made only two assumptions to derive Eq. (5): that the wavefront is a scalar field and the object is planar. If we assume the object and pupil function are not frequency dependent and that the detector response is constant over the band of interest, then

$$\begin{aligned} i(x, y) &= \kappa \tau R^2 \int_{-\infty}^{\infty} \int_{-\infty}^{\infty} \int_{-\infty}^{\infty} \int_{-\infty}^{\infty} [\Gamma(x_1, y_1; x_2, y_2) o(x_1, y_1) p(x - x_1, y - y_1) \\ &\quad \times o^*(x_2, y_2) p^*(x - x_2, y - y_2)] dx_1 dy_1 dx_2 dy_2, \end{aligned} \quad (6)$$

where the function  $\Gamma(x_1, y_1; x_2, y_2)$  is the coherence function:

$$\Gamma(x_1, y_1; x_2, y_2) = \frac{1}{\tau} \int_0^\tau s(x_1, y_1; t) s^*(x_2, y_2; t) dt, \quad (7)$$

which measures the ability of light from across a source to interfere.

We now consider two extreme cases of coherence. Sources for which interference fringe visibility is always maximum regardless of their spatial separation are spatially coherent. This is represented by

$$\Gamma(x_1, y_1; x_2, y_2) = I_0, \quad (8)$$

in which case Eq. (6) reduces to

$$i_{coh}(x, y) = \kappa \tau R^2 I_0 |o(x, y) * *p(x, y)|^2. \quad (9)$$

Equation (9) indicates that spatially coherent imaging adds wavefronts in terms of complex wave amplitudes.

In contrast, sources for which interference fringe visibility is always minimum regardless of their spatial separation are referred to as spatially incoherent. In this case, the coherence function is

$$\Gamma(x_1, y_1; x_2, y_2) = I_0 \delta(x_1 - x_2, y_1 - y_2), \quad (10)$$

and Eq. (6) is

$$i_{\text{inc}}(x, y) = \kappa \tau R^2 I_0 |o(x, y)|^2 * * |p(x, y)|^2. \quad (11)$$

Thus, spatially incoherent imaging adds wavefront irradiances. The system response,  $|p(x, y)|^2$ , is the point spread function (PSF). Its Fourier transform  $H(u, v)$  is the optical transfer function (OTF), which is proportional to the two-dimensional autocorrelation of the pupil function  $P(u, v)$ :

$$\begin{aligned} H(u, v) &= P(u, v) \star \star P(u, v), \\ &= \int_{-\infty}^{\infty} \int_{-\infty}^{\infty} P(u', v') P^*(u + u', v + v') du' dv'. \end{aligned} \quad (12)$$

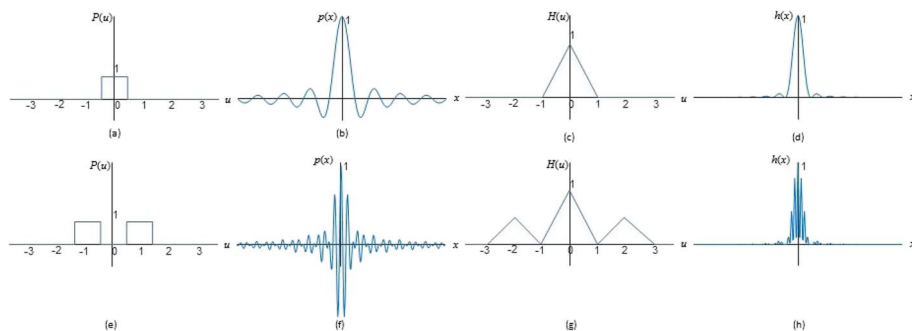
For simplicity, we omitted the constant of proportionality, which has minimal impact on our analysis. The OTF is, nonetheless, represented with unity maximum value at its origin.

We note that all real sources are partially coherent. Some tend more toward one extreme than the other. Most passive imaging is spatially incoherent. As shown above, the nature of active imaging depends upon the source used. Microscopy, metrology, and lithography are applications in which understanding and controlling the source and its coherence are particularly critical.

The impact of coherence on an imager's response is represented in Fig. 3. An imaging system with a one-dimensional clear aperture represented by the pupil function  $P(u)$  in Fig. 3(a) generates the sinc-function coherent response  $p(x)$  in Fig. 3(b). The incoherent response is represented by the OTF and PSF in Fig. 3(c) and 3(d), respectively. Figures 3(e)–3(h) represent the pupil function, CSF, OTF, and PSF, respectively, for two clear apertures.

Note that the incoherent response is marked by the dominance of low-pass structure. It is, in fact, impossible to generate a bandpass response in an incoherent system. The image will always contain a large low-pass bias. This increases noise and reduces dynamic range in systems that combine multiple images incoherently to create a single output image. Noise in the final image is proportional to the total image bias, which is

**Figure 3**



Optical response of an imaging system with a one-dimensional aperture in the pupil plane. (a) Pupil function for a single open aperture. (b) CSF. (c) Incoherent OTF. (d) Incoherent PSF. (e) Pupil function for two open apertures. (f)–(h) Corresponding CSF, OTF, and PSF, respectively.

the sum of individual bias terms [45]. As we discuss in the Section 4.3, the relative levels of signal and noise affect image resolution.

Since electronic detectors are not continuous but discrete, the continuous wavefronts of Eqs. (9) and (11) are converted into a digital representation  $i_d(x, y)$  via sampling and quantization:

$$i_d(x, y) = \sum_{m=-\infty}^{\infty} Q[i(x_m, y_m)]\delta(x - x_m, y - y_m), \quad (13)$$

where the measurement  $i(x_m, y_m)$  is the total energy incident upon a single detector pixel of area  $A_d$  during an exposure, the set of points  $(x_m, y_m)$  defines the sampling lattice, and  $Q[\cdot]$  quantizes the continuous values at each sample point. The sampling lattice for most detector arrays is rectilinear, i.e.,

$$\sum_{m=-\infty}^{\infty} \delta(x - x_m, y - y_m) = \sum_{k=-\infty}^{\infty} \sum_{\ell=-\infty}^{\infty} \delta\left(x - \frac{k}{\Delta_x}, y - \frac{\ell}{\Delta_y}\right), \quad (14)$$

where  $\Delta_x$  and  $\Delta_y$  represent the spacing between detector pixels along the  $x$  and  $y$  directions, respectively.

If we represent the noise-free measurements from the detector as a matrix  $\mathbf{I}$ , its matrix elements are

$$I_m = Q[i(x_m, y_m)], \quad (15)$$

and the sampled and quantized irradiances from coherent and incoherent imagers are

$$\mathbf{I}_{\text{coh}} = |\mathbf{PO}|^2, \quad (16)$$

$$\begin{aligned} \mathbf{I}_{\text{inc}} &= |\mathbf{P}|^2 |\mathbf{O}|^2, \\ &= \mathbf{H} |\mathbf{O}|^2, \end{aligned} \quad (17)$$

where the operator  $|\cdot|^2$  replaces each matrix element with its squared magnitude.

The functions represented in bold font in Eqs. (16) and (17) are matrix representations of spatial domain quantities. The vector  $\mathbf{O}$  represents the complex-wave amplitude of a sampled and lexicographically ordered representation of the object  $o(x, y)$ . If the object contains  $N_x \times N_y$  elements,  $\mathbf{O}$  is a  $N_x N_y \times 1$  vector. The operator  $\mathbf{P}$  is a matrix that represents the coherent optical response. That is, each column in  $\mathbf{P}$  contains the spatial response to a point object at a distinct location in object space. Thus, the matrix multiplications in Eqs. (16) and (17) realize the convolution between an input object and the system response. If the system is linear and shift-invariant, the columns of  $\mathbf{P}$  are shifted representations of each other, where the shift is determined by the column number. If the optical response has finite size, when sampled, there will be  $N_p$  non-zero elements and  $\mathbf{P}$  is  $(N_x N_y + N_p - 1) \times (N_x N_y)$ . The detected image  $\mathbf{I}$  is  $(N_x N_y + N_p - 1) \times 1$ .

The measurements of irradiance  $\mathbf{M}$  that the detector produces are not noise free and, in fact, contain artifacts from sampling, quantization, and the transduction from photons to electrons. If we combine these artifacts into a single noise term, the imaging measurements are

$$\mathbf{M} = \mathbf{I} + \mathbf{n}, \quad (18)$$

where  $\mathbf{n}$  represents noise introduced into the system by detection.

These measurements are processed by an operator  $\mathbf{T}$  to obtain processed information  $\mathbf{I}'$ :

$$\begin{aligned}\mathbf{I}' &= \mathbf{T}[\mathbf{M} + \mathbf{n}] + \mathbf{n}_T, \\ &= \mathbf{T}[\mathbf{M}] + \mathbf{n}',\end{aligned}\tag{19}$$

where  $\mathbf{n}_T$  is noise generated by post-detection processing and  $\mathbf{n}'$  is noise generated during the overall imaging process. The operator  $\mathbf{T}$  can be linear or nonlinear.

To derive the relationship between object and image we made several assumptions, including that the object can be represented by a planar, quasi-monochromatic scalar wavefront. As we show in this review, computation can be used to overcome the limitations of these assumptions to image, for example, objects that are polychromatic, three-dimensional, or polarized. Computation can also be used to improve the resolving power of an imager and to image non-classical optical properties, such as photon entanglement. In the next section, we discuss the impact of computation on optical design.

#### 4.3. Optical Design

Given the essentials presented in Section 4.2, we ground further our discussion on Computational Imaging by defining an ideal image as an exact geometric representation of the object. That is, ignoring magnification,  $p(x,y) = \delta(x,y)$  and  $\mathbf{P}$  is the identity matrix.

But we know that any image acquired under real conditions contains artifacts of blurring. The response due to a finite aperture produces a non-ideal image given by the PSF in Eq. (11). For a clear aperture, the OTF and PSF in Figs. 3(c) and 3(d), respectively, represent the best possible imaging conditions. However, blur is also generated by a variety of causes, including defocus and other geometric aberrations, chromatic effects, camera jitter, and atmospheric turbulence.

One of the first high-profile examples of using computation to correct optical aberrations was in the Hubble telescope [46]. (The conventional approach, i.e., replacing the optics, was eventually implemented.) The results provided dramatic evidence of computation's potential to improve image quality and spurred some of the community's initial efforts. In this section, we designate the methods an optical designer can use to compensate for the imperfections in imaging, in light of computation, as decoupled, collaborative, and integrated.

##### 4.3a. Decoupled

Decoupled design is another way of saying that optical design and post-detection processing are performed independent of one another. A conventional optical design is performed that minimizes geometric and chromatic aberrations to yield a PSF  $\mathbf{H}$  that is as close to the identity matrix as possible. Post-detection processing is used to create a better estimate of the geometric image.

In image estimation, one assumes the optics represented by  $\mathbf{H}$  are fixed and the goal is to determine a processing algorithm  $\mathbf{T}$  such that the difference between the image  $\mathbf{I}'$  and the object irradiance  $|\mathbf{O}|^2$  is minimal, for example, in a mean-squared sense.

Combining Eqs. (17) and (18), the spatial domain measurement  $\mathbf{M}$  is

$$\mathbf{M} = \mathbf{H}|\mathbf{O}|^2 + \mathbf{n},\tag{20}$$

and the processed measurement  $\mathbf{I}'$  is

$$\mathbf{I}' = \mathbf{T}[\mathbf{H}|\mathbf{O}|^2 + \mathbf{n}]. \quad (21)$$

In the noise-free case, if  $\mathbf{H}$  is invertible, the solution to Eq. (21) is

$$\mathbf{T} = \mathbf{H}^{-1}. \quad (22)$$

However, sometimes  $\mathbf{H}$  cannot be measured and inverted directly, e.g., in surveillance applications, in which case Eq. (22) is ill-conditioned. Furthermore, small amounts of noise in the measurements can significantly affect the solution.

If one assumes the noise is white and Gaussian, the optimal solution for  $\mathbf{T}$  is the Wiener filter [47]:

$$\mathbf{T} = (|\mathbf{H}|^2 + \hat{\Phi}_n)^{-1}\mathbf{H}, \quad (23)$$

where  $\hat{\Phi}_n$  is the power spectral density of the noise. Other enhancement methods include iterative algorithms, such as Richardson–Lucy [48] when the PSF is known, and blind de-convolution when the PSF is unknown [49]. For an extensive survey of image de-blurring algorithms from the last 40 years, see Ref. [50].

For applications in which the quality of imaging optics is inherently poor but the imaging environment can be controlled, for example, imaging through thin scattering media like biological tissue [51] or through multimode fibers in endoscopy [52], it is possible to measure the system response to inputs from all possible spatial locations and build up  $\mathbf{H}$  through calibration. Some researchers have taken this approach to the extreme by removing conventional optical elements altogether [53] or deliberately replacing them with random elements [54].

#### 4.3b. Collaborative

In a collaborative approach, a designer uses his or her knowledge of optics and processing to exploit each to their best advantage. For example, since post-detection processing is an effective method to invert geometric distortions, a designer can expend minimal design resources to remove distortions optically and apply more resources to correct spatio-chromatic aberrations. That is, the solutions to achieve a desired performance are conventional; the designer chooses an optical or a computational approach depending upon which provides the best performance at the lowest cost.

#### 4.3c. Integrated

An integrated design considers explicitly the interplay between optics and computation in imaging. The objective is to use computation to improve the imaging performance of the optics or to replace optical elements while maintaining or improving imaging performance. In either case, the optics are designed to achieve something other than a conventional PSF so that after processing, a PSF with improved properties of some kind is obtained.

With respect to Eq. (21), the goal is to design the optics  $\mathbf{H}$  and the processing  $\mathbf{T}$  such that their combination yields a desired response  $\mathbf{Z}$ . If  $\mathbf{T}$  is linear,

$$\mathbf{Z} = \mathbf{T}\mathbf{H}. \quad (24)$$

This joint optical–digital design approach, discussed in Refs. [55–59], reflects the philosophy first espoused in Refs. [23–26], wherein the burden of image formation is shared across domains.

In one example [56], computation is used to insure the modulation transfer function (MTF) (the magnitude of the OTF) of an IR imaging system is above a set threshold across the band of spatial frequencies. A conventional optical design requires two

optical elements to meet these constraints. The performance of a single optical element is limited by spherical aberration, astigmatism, and field curvature. However, if a single element is designed in conjunction with the post-detection processing, it is possible to produce imagery that meets the MTF specifications with only a slight noise penalty. By reducing the element count, the wavefront engineered design reduces weight and additional costs related to housing and assembly.

A similar approach to optical design was used in Ref. [60] to improve the noise performance of an imaging system. Ray tracing software was used in an iterative design algorithm that applied a Wiener filter in post-detection. Mean-squared-error was used as the objective measure to drive the design. Figure 4 compares results generated after Wiener filtering images produced by a conventionally designed optical element to those produced through joint design. The subjective improvement visible in the final image of the joint design is substantiated by objective measures.

In these two examples, the desired response  $\mathbf{Z}$  approximates a one-to-one mapping from object to image. However, this is not a requirement. For example, [61] discusses the realization of a bandpass filter for a millimeter wave imager.

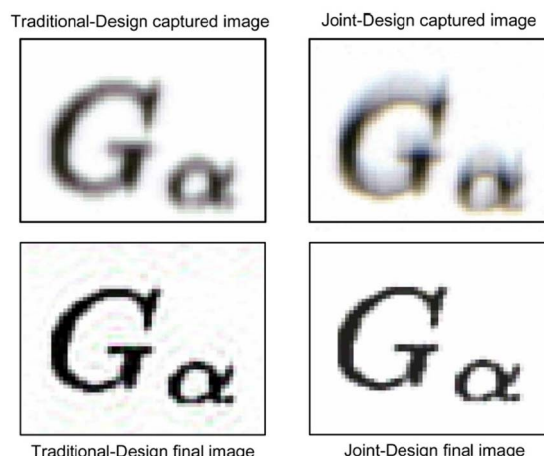
Further, the conditions under which computation offers an advantage in joint design have been investigated in a preliminary fashion [62–64]. The results indicate that computation such as this offers an advantage in low signal-to-noise ratio (SNR) conditions. For scenes that are well illuminated, the advantage from computation is low.

The essential point is that the optics are designed deliberately not to approximate a point response or, equivalently, not to produce the OTF that corresponds to a clear aperture. Instead, the optics are designed to encode information onto the wavefront so that it can be readily extracted through processing after measurement. The desired information is not measured directly. Given the emphasis on information, we present some essential concepts on information theory before we end this section.

#### 4.4. Information Essentials

Information about an object is embedded in the wavefront it emits or reflects. However, Eqs. (9) and (11) indicate that no imager with a finite entrance aperture

Figure 4



Joint optical–digital design. Left column: image produced by conventionally designed optics and results after Wiener filtering. Right column: same as the left column except the optics were designed by incorporating Wiener filtering. Reprinted with permission from [60]. Copyright 2008 Optical Society of America.

can pass all information incident upon it [6,65,66]. Given Eq. (3), an imager with a focal length  $f$  and a clear, circular aperture of diameter  $D$  produces an Airy disk when imaging a point source at wavelength  $\lambda$  [14]. The first zero of this function,  $1.22\lambda f/\#$  is the source of the Rayleigh resolution limit, where the  $f$ -number  $f/\#$  is

$$f/\# = \frac{f}{D}. \quad (25)$$

Although Rayleigh resolution is conventionally interpreted as a physical limit on the resolution of an imager, we use it as a measure of the degrees of freedom within an imager. If a coherent imager has a detector plane with a maximum linear dimension  $W_d$ , the number of resolvable points  $S$  in the image is proportional to

$$S = \left( \frac{W_d D}{\lambda f} \right)^2. \quad (26)$$

Thus,  $S$  is a fundamental limit on the capacity for information transfer, which we refer to as the space-bandwidth product (SBWP) [8–12,32,67,68].

For a given system,  $S$  is a fixed parameter. Since the OTF of an incoherent imager is the autocorrelation of the pupil function  $P(u, v)$ , the SBWP of an incoherent imager is  $4S$ . Although fundamentally important, we are not strict about the factor of 4 when referring to SBWP since it has minimal impact on the development of Computational Imaging concepts. It is important to the forthcoming discussion to recognize that using resources in one plane to encode information reduces the availability of resources in the complementary domain.

Equation (26) illustrates how optics and measurement limit information and, at best, represents an upper bound on information content. During wavefront measurement, random and deterministic processes introduce noise, which, along with detector sampling, introduces measurement error and reduces information.

Optical noise is a function of photon statistics, which can be represented as a Poisson process. For large signals, the Poisson process is approximately Gaussian with equal and signal-dependent mean and variance. Since this noise scales as the square root of the number of photons, one can increase the number of photons measured and, thereby, increase SNR using large apertures, long detector integration times, or both. However, long integration times reduce information contained in high temporal frequencies and large apertures increase the size, weight, and cost of a system.

Electronic noise is added to the measurement by the random generation of electrons within the detector and associated electronics. In addition, as indicated in Eq. (13), a detector array spatially samples the wavefront at a rate determined by the pixel spacing. Photons incident upon a single detector pixel are spatially and temporally integrated to produce an electrical signal associated within that spatial sample. If the spatial sampling rate is not sufficiently high, aliasing is present in the measurements, which can be modeled as signal-dependent additive noise [69,70].

A variety of methods have been applied to the assessment of image quality. In an effort to define image quality in terms of information metrics, some imaging researchers have looked to communications theory for insight and guidance. From Shannon, the information capacity of a communication channel with bandwidth  $B_w$  and signal-to-noise ratio SNR is

$$C_p = B_w \log_2(1 + \text{SNR}). \quad (27)$$

The operand of the logarithm represents the number of bits of information contained within a measurement of signal plus noise.

Fellgett and Linfoot proposed Shannon-information-based metrics as an alternative to conventional image fidelity metrics as early as 1955 [71]. In 1970, Frieden, motivated by a desire to understand the impact of noise on image restoration, developed a relationship between information and the ability to restore images [72]. One can even derive an information-theoretic model of imaging analogous to Eq. (27) [34]. Heuristically, one uses the spatial sampling rate of the detector array to determine bandwidth, object power spectral density, and system OTF to determine signal, and measurement noise and aliasing to determine noise. Subsequently, researchers have analyzed imaging systems using information theory to explore topics such as degrees of freedom, channel capacity, and optimum coding [73–78].

Given the definition of Computational Imaging as the indirect measurement of a desired quantity, conventional fidelity metrics of imaging are often inadequate to assess performance. Instead, a key element of Computational Imaging is designing a measurement  $X$  and post-detection processing to estimate a desired parameter  $\theta$ . For a given  $\theta$ , the probability that a particular sample  $X$  results from the measurement is  $f(X; \theta)$ .

When one designs an estimator  $\hat{\theta}(X)$  for  $\theta$ , one would like to know how well it performs. If the estimator is unbiased, i.e., its expected value is  $\theta$ , the Cramer–Rao inequality places a lower bound on the estimator uncertainty  $\Delta\hat{\theta}(X)$ ,

$$\Delta\hat{\theta}^2 \geq \frac{1}{F(\theta)}, \quad (28)$$

where  $F(\theta)$  is the Fisher information,

$$\begin{aligned} F(\theta) &= E\left[\left(\frac{\partial}{\partial\theta} \log f(X; \theta)\right)^2\right], \\ &= \int \left(\frac{\partial}{\partial\theta} \log f(x; \theta)\right)^2 f(x; \theta) dx, \end{aligned} \quad (29)$$

and  $E[\cdot]$  denotes expected value. This bound on system performance provides a means to assess performance quantitatively. A detailed discussion of Fisher information and its relevance across multiple scientific disciplines can be found in Ref. [79].

Thus, Fisher information is a measure of parameter estimation accuracy that depends on the choice of observables and their measurement. This is particularly germane to Computational Imaging. Fisher information can be used to evaluate the advantages of a coded measurement and can inform designs to perform the measurements. For example, Fisher information has been used in imaging to estimate a finite set of Fourier coefficients from image data [80].

This insight allows us to make general statements about Computational Imaging that inform the remainder of this review. The goal in Computational Imaging is to optimize information in each measurement relative to a parameter of interest. This does not mean that one increases the information contained in a wavefront. Instead, it means that one can encode wavefront information in such a way that uncertainty in parameter estimation is minimized after measurement. Thus, benefits can be gained by designing the measurement and the post-processing algorithms in unison. Important considerations in the co-design of optics and post-detection processing are the ease with which the encoding can be inverted, its sensitivity to noise, and identifying its associated null

spaces. In the next section, we categorize the motivations for Computational Imaging before reviewing examples of Computational Imagers.

#### 4.5. Motivations

Having identified the elements of Computational Imaging, we now define three distinct categories of computational imagers that fit our definition of indirect measurements. The categories are distinguished by their different motivations for employing computation, namely, providing an operational capability that:

1. is impossible to realize using conventional means,
2. addresses a dimensionality mismatch, and
3. reduces the cost of making measurements in comparison to conventional means.

A review of the imaging literature with these motivations in mind reveals that the philosophy behind Computational Imaging is not new. One of the earliest examples of Motivation 3 is the Michelson Stellar Interferometer [81]. Michelson recognized that to measure the diameter of an astronomical object via imaging requires a telescope with an extremely large aperture. To overcome this practical constraint, he developed an alternative means to measure diameter. The interferometric approach that he developed changes the nature of the measurement from one that is difficult to obtain to one that simplifies the derivation of the desired information. (The computation required was fringe counting.) As we show below, other antecedents to Computational Imaging include holography, synthetic aperture radar, coded-aperture imaging, magnetic resonance imaging, and computed tomography.

In the remainder of the review, we present numerous examples of systems that fall under these different motivations. In each, we highlight how pre-transduction encoding simplifies post-transduction information extraction. In some instances, we present imaging systems that are not computational to provide contrast and underscore the distinguishing attributes of Computational Imaging.

We note that the encoding can occur in three planes (source, pupil, and detector) or combinations thereof. Some researchers have used these distinctions to develop a taxonomy to delineate computational approaches. However, such taxonomies address implementation and not motivation. Since our goal is not to compare the merits of one implementation over another, we use this taxonomy implicitly, and not explicitly, by indicating in which domain encoding is deployed.

### 5. MOTIVATION 1: CONVENTIONAL IMAGING IS IMPOSSIBLE

There exist circumstances in which it is physically impossible to form an image using conventional means. Some examples include imaging optical properties such as coherence or quantum entanglement, or even the optical phase of an object. Other examples are from medical imaging, where indirect measurements are an alternative to invasive surgery to examine a body's internal organs. None of these images can be created without modifying the measurement schema and all require computation to generate the desired image. Further, the operation of these computational imagers is grounded in physics. Although technology is required to enable the required measurement and necessary processing, no technology can be conceived that is capable of measuring the parameters of interest directly.

#### 5.1. Phase Imaging

Electromagnetic waves are characterized by electric and magnetic fields whose amplitude and phase are functions of space and time. Their spectrum ranges from radio

frequencies ( $10^3$  Hz) to gamma rays ( $10^{20}$  Hz). Visible and IR radiation, with which we are primarily concerned, range between  $10^{14}$  and  $10^{15}$  Hz.

Phase plays a critical role in encoding information on an electromagnetic wave about objects in a scene. In some cases, particularly in the visible spectrum, objects may be transparent and modulate only the phase of a wave. Even cases where objects modulate only the wave amplitude, propagation converts critical object information into the wavefront phase. Thus, the measurement of phase is important.

The availability of high-speed electronics enables the direct measurement of phase at radio frequencies. This is not the case at visible and IR frequencies. Since the phase of a wave cannot be measured directly and must be measured indirectly, by our definition, the measurement of phase requires a Computational Imaging approach. That is, it requires a combination of front-end wavefront manipulation and post-detection processing to extract phase. We consider classical approaches to visualizing optical phase and compare them to recent approaches that exploit *a priori* information and computation.

### 5.1a. Phase Contrast Microscope

If the imaged scene contains objects that are transparent and impose only a small amount of phase change onto an incident wave, e.g., microscopic imaging of biological cells, it is possible to visualize phase without a reference and using only optical processing. This is the principle behind Zernike's phase contrast microscope [82].

The phase contrast microscope assumes the imaged object  $o(x, y)$  is

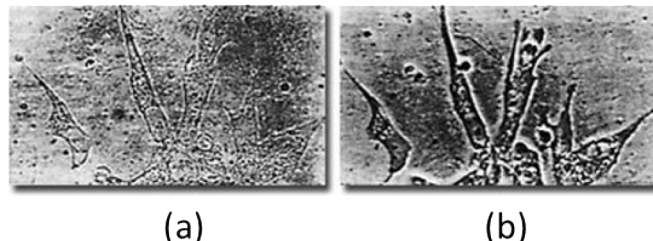
$$\begin{aligned} o(x, y) &= \exp[j\theta_s(x, y)], \\ &\approx 1 + [j\theta_s(x, y)]. \end{aligned} \tag{30}$$

If the unmodulated bias term is phase shifted by  $\pi/2$ , e.g., using an on-axis phase filter in the Fourier plane of Fig. 2, the irradiance of the detected image is

$$\begin{aligned} i(x, y) &\approx |j + [j\theta_s(x, y)]|^2, \\ &\approx 1 + 2\theta_s(x, y). \end{aligned} \tag{31}$$

Figure 5 compares a conventional image to one formed using the phase contrast method. We reiterate that, since introducing a phase plate in the pupil plane renders the object phase visible without further processing, this is an example of optical processing, not Computational Imaging.

Figure 5



Comparison of (a) brightfield versus (b) phase-contrast images. Original images recorded by Zernike. Reprinted with permission by M. W. Davidson, The Florida State University, and Molecular Expressions website [83]. Copyright 1995–2017.

### 5.1b. Interferometry and Holography

The conventional method to measure optical phase is to convert it into an intensity distribution, which is detectable. To do so, though, requires a reference that is coherent to the wavefront propagating from a scene of interest. If a reference wave  $r(x, y; t)$  in the measurement plane,

$$r(x, y; t) = \exp[j2\pi\nu t] \exp[j\theta_0(x, y)], \quad (32)$$

interferes with a signal wave  $s(x, y; t)$ ,

$$s(x, y; t) = A(x, y) \exp[j2\pi\nu t] \exp[j\theta_s(x, y)], \quad (33)$$

their superposition is

$$\tilde{r}(x, y; t) = r(x, y; t) + s(x, y; t). \quad (34)$$

The recorded signal  $h(x, y)$  is proportional to the energy in  $\tilde{r}(x, y; t)$ :

$$\begin{aligned} h(x, y) &\propto \frac{1}{T} \int_0^T |r(x, y; t) + s(x, y; t)|^2 dt, \\ &= 1 + A^2(x, y) + 2A(x, y) \cos[\theta_0(x, y) - \theta_s(x, y)]. \end{aligned} \quad (35)$$

The fringe pattern described by Eq. (35) is a coded representation of the scene phase  $\theta_s(x, y)$ , which can be obtained via phase unwrapping in post-detection.

Before phase-unwrapping algorithms were made routine by electronic computers, holography provided a means to visualize not just the phase of a scene, but the scene that gave rise to the phase. Dennis Gabor invented holography in 1948 to increase the resolution of nascent electron microscopy technology [84]. Gabor's approach, true to the philosophy of Computational Imaging, was to change the measurement. He proposed measuring the entire field against a reference. (Hologram is from the Greek for “whole picture.”)

An image of the object scene  $o'(x, y)$  is formed by illuminating the recording  $h(x, y)$  with the conjugate of the reference beam:

$$\begin{aligned} o'(x, y; t) &= r^*(x, y; t)h(x, y), \\ &= \{[1 + A^2(x, y)] \exp[-j\theta_0(x, y)] + A(x, y) \exp[-j\theta_s(x, y)] \\ &\quad + A(x, y) \exp[j\theta_s(x, y)] \exp[-j2\theta_0(x, y)]\} \exp[j2\pi\nu t]. \end{aligned} \quad (36)$$

The phase conjugate nature of the on-axis image (the last term in the second line) indicates the image is real. Waves diverging from the scene are now converging to the image. The other image elements contain high spatial frequencies.

As represented in Fig. 6, Gabor's approach relied on self-interference. Thus, the three images lie on top of each other. The invention of off-axis holography [15–17] allows one to separate the images. See Fig. 7.

As an aside, the development of digital electronic processing allows one to replace either the optical recording or the playback of an off-axis hologram with processing. Replacement of the recording process led to the development of computer-generated holography or, more generally, diffractive optics [85]. Replacement of the optical playback led to the development of digital holography [86–90]. The first computationally reconstructed hologram was detected by a vidicon, sampled in a  $256 \times 256$  array, and Fourier transformed on a PDP-6 computer using the fast Fourier transform

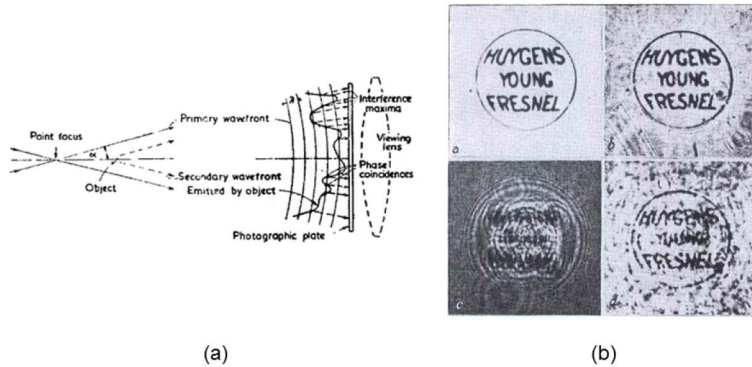
algorithm [86]. The further development of detector arrays whose performance matched that of film established digital holography as a critically important imaging technique.

### 5.1c. Phase Retrieval from Magnitude

Computation has had significant impact on the estimation of optical phase from measurements. In the 1950s, as information theory began to influence image science, researchers enumerated the degrees of freedom contained in an image as a consequence of a finite entrance aperture [8–12]. This approach differed from the conventional, more physical, approach that yields the Rayleigh resolution limit. Although finite extent objects theoretically have infinite bandwidth, their images have bandwidths that are limited by free-space propagation and the aperture of the imaging optics. Consequently, although an aperture can pass a large number of basis functions, the most significant image information is contained in a small number of functions with dominant eigenfunctions.

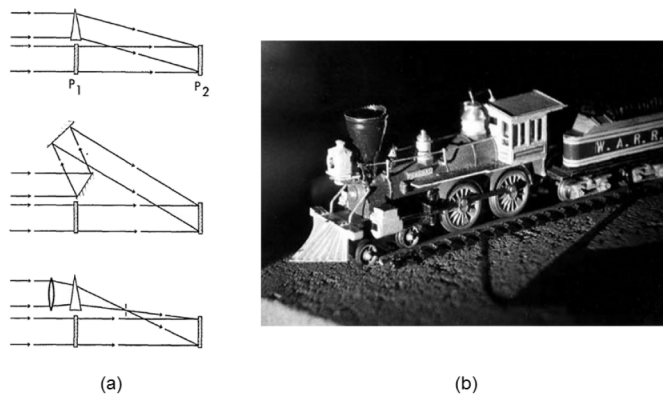
Originally, such results were mathematical constructs only. However, the development of computational tools turned mathematical constructs into algorithmic constraints.

**Figure 6**



Gabor hologram. (a) Recording geometry. (b) Reconstruction. Reprinted by permission from Macmillan Publishers Ltd.: D. Gabor, Nature **161**, 777–778 (1948) [84]. Copyright 1948.

**Figure 7**



Off-axis hologram. (a) Options for recording an off-axis hologram. (b) Reconstruction. Reprinted with permission from [17]. Copyright 1964 Optical Society of America.

The constraints defined a set of functions within which one could search for a solution. This approach led to the development of the first practical phase retrieval algorithm [38–40]. The error-reduction approach, represented in Fig. 8(a), uses a single intensity measurement (typically the Fourier magnitude) and the iterative application of constraints in both the image and Fourier domains to generate a Fourier phase that satisfies all the physical constraints.

At the  $k$ th iteration, an estimate of the object,  $g_k(x, y)$ , is Fourier transformed. The Fourier transform is forced to conform to the known Fourier modulus, and the result is inverse transformed to produce the image  $g'_k(x, y)$ . The iteration is completed by forming a new estimate of the object that conforms to the object-domain constraints:

$$g_{k+l}(x, y) = \begin{cases} g'_k(x, y), & (x, y) \in R \\ 0 & (x, y) \notin R, \end{cases} \quad (37)$$

where the region  $R$  includes all points at which  $g'_k(x, y)$  satisfies the constraints.

The philosophy of the input–output algorithm represented in Fig. 8(b) differs slightly from that of the error-reduction algorithm. Strict satisfaction of the object constraints is not required. Instead, one alters the object estimate in a manner that reduces error in the output  $g'(x, y)$  in the image domain:

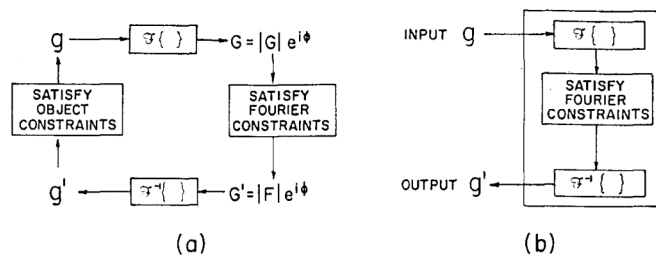
$$g_{k+l}(x, y) = \begin{cases} g'_k(x, y), & (x, y) \in R \\ g_k(x, y) - \beta g'_k(x, y) & (x, y) \notin R, \end{cases} \quad (38)$$

where  $\beta$  is a constant. Results from two different input–output reconstructions are presented in Fig. 9.

Specification of *a priori* information and the constraints is key [38,91,92]. A principal constraint is that the object has finite extent, and its intensity must be nonnegative. The maximum object extent is half the extent of the image autocorrelation. Recent reviews of phase retrieval and its applications are in Refs. [93,94]. One particular field that has benefited significantly from advances in phase retrieval is x-ray coherent diffraction imaging [95].

We note that each technique presented in this section attempts to solve an ill-posed inverse problem by incorporating *a priori* information or domain specific constraints. In phase contrast microscopy, one limits the class of objects imaged. They are assumed to be transparent and impose only small phase perturbations. In holography, constraints on the object are less restrictive. Instead, one uses a reference beam that is spatially and temporally coherent with respect to the field whose phase is unknown and uses either optical or digital reconstruction to reconstruct the phase. Finally,

**Figure 8**



Phase retrieval algorithms. (a) Error-reduction algorithm. (b) Input–output algorithm. Reprinted with permission from [38]. Copyright 1978 Optical Society of America.

in phase retrieval, an intensity measurement is made with a coherent source and one applies constraints based on physics in post-processing (e.g., support constraints, non-negativity, and sparsity) to estimate phase.

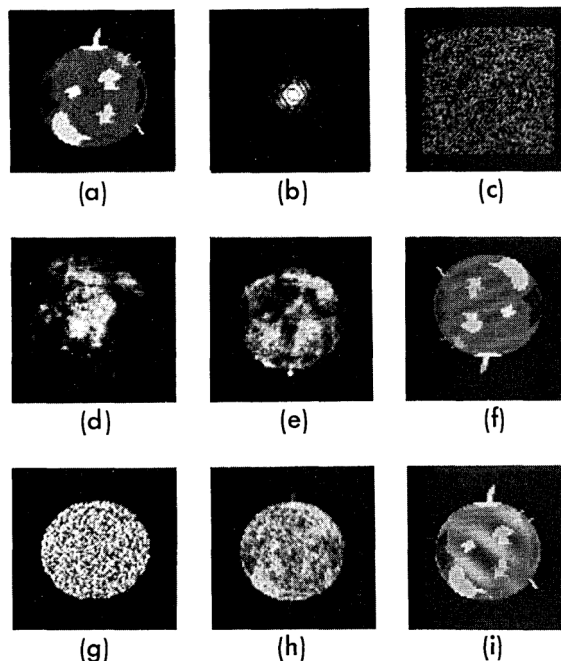
### 5.2. Quantum Imaging

Our discussion in Section 4 assumed we image using a classical electromagnetic property. All imagers we discuss in this review satisfy this assumption except the one addressed in this section. When one considers non-classical properties of light, new imaging opportunities emerge.

Quantum photon entanglement occurs when photons are generated in such a manner that the quantum state of one photon is dependent on the state of the other photons. Analogous to the correlation between classical wavefronts that form the foundation of coherent and incoherent imaging, the correlations between quantum states can be exploited to create new imagers and can also be exploited to image these quantum states [96–99]. It has recently been shown that conventional properties of optical fields, such as coherence and polarization, also exhibit entangled properties [100–103].

Coincidence, or ghost, imaging uses correlated optical fields to image an object that is not present within the imaging system itself. As shown in Fig. 10(a), a source produces a pair of photons, which are transmitted through different optical paths. One photon illuminates an object in a path that contains no imaging optics. Instead, it contains a large single pixel detector, referred to as a bucket. If the object transmits the photon, it is detected by the bucket detector. The other photon travels through an imaging system in which the object is not present. The imaging system contains a two-dimensional detector array. An image of the object is created by keeping only those

Figure 9



Results from phase retrieval algorithm. (a) Test object. (b) Modulus of test object Fourier transform. (c) Initial estimate of object in one test. (d)–(f) Reconstruction results—number of iterations: (d) 20, (e) 230, (f) 600; (g) initial estimate of object in a second test. (h)–(i) Reconstruction results—number of iterations: (h) 2, (i) 215. Reprinted with permission from [38]. Copyright 1978 Optical Society of America.

detected photons that are coincident with a photon detection in the bucket. This is done by processing the photon statistics from the two detectors to look for correlations. In effect, the temporal output of the bucket detector labels which of the multitude of photons detected by the array actually carry image information. This produces images like the one shown in Fig. 10(b).

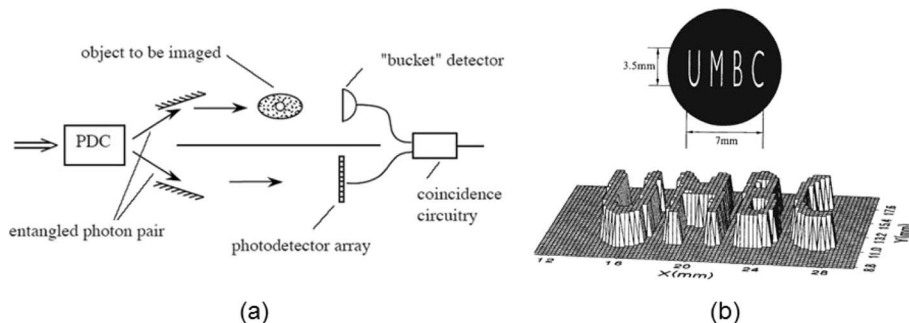
Although the first ghost imaging experiment exploited the spatial entanglement of photons generated in spontaneous parametric downconversion [96], nearly all features of ghost imaging can be replicated using thermal light [104]. Despite the similarities between quantum and thermal ghost imaging, thermal ghost images exhibit a large bias, which increases noise and degrades image quality. In fact, this distinction has since led to a test for determining the presence or absence of quantum entanglement in a wave-front [105]. Also, inspired by work in Computational Imaging, new methods of ghost imaging have been developed that exploit the power of post-detection processing to alter the measurements required and, thereby, improve imaging performance [106].

### 5.3. Volumetric Imaging

We recognize that our delineation between motivations may not be as definitive as we would like. Such is the case in our discussion of volumetric imaging and the two examples from medical imaging, computed tomography (CT) and magnetic resonance imaging (MRI). Are they computational because there exists no way to non-invasively form an *optical* image of a body's internal organs or are they computational because the images are three-dimensional? By placing the discussion of volumetric imaging last in this section, we acknowledge the ambiguity but leave it open for discussion and allow it to serve as a bridge to the next section.

A theory of three-dimensional volumetric imaging has been difficult to ascertain [107–111]. Key among these difficulties is understanding the contributions from multiple planes into the detector plane [110]. Thus, volumetric imaging has been difficult to formalize, and it has been difficult to develop measurement and reconstruction algorithms. Instead, one can image a volume using conventional methods to map an object plane onto a two-dimensional detector and scan through different object planes. In these instances, it is possible to remove artifacts from other planes optically, for example, scanning a pinhole to image point-to-point in confocal microscopy [112,113] or via

Figure 10



Coincidence imaging. (a) Optical system for coincidence imaging. PDC is a parametric down converter that produces photon pairs. Reprinted with permission from Boyd *et al.*, Proc. SPIE 7342, 73420B (2009) [97]. Copyright 2009. (b) First image produced via coincidence imaging. Figure 2 reprinted with permission from Pittman *et al.*, Phys. Rev. A 52, R3429–R3432 (1995) [96]. Copyright 1995 American Physical Society. <https://journals.aps.org/prl/abstract/10.1103/PhysRevA.52.R3429>.

post-detection processing. Scanning holographic techniques have also been used [114,115]. We do not consider such techniques computational; the image is created from a sequence of direct measurements.

The fundamental issue in volumetric imaging is the inability to image through objects at wavelengths in the visible and IR spectrum. This is particularly frustrating in medical applications. Since antiquity, visual inspection of the human body has been used to make diagnoses about medical ailments. It is most natural for organs that are directly accessible, such as the skin. But it is also possible to look inside the body through natural openings, such as the mouth, nose, ears, eyes, and anus. Indeed, modern technology has provided increasingly sophisticated instruments, such as endoscopes, bronchoscopes, and otoscopes, to acquire detailed images of internal organs that are accessible through these openings. Alternatively, one can insert imaging instruments through a surgical incision. In fact, imaging probes equipped with surgical instruments allow surgeons to perform procedures through minor incisions that previously required much larger incisions and general anesthesia.

In some instruments, images are transported optically out of the body via a series of lenses or a coherent fiber bundle. However, the miniaturization of electronic cameras has also enabled the integration of light sources, lenses, and detectors on the tip of an instrument. In such cases, electrically encoded images can be transmitted from a body's interior to its exterior via ultra-thin electrical cables or a wireless link. For the medical community, such instruments provide revolutionary capabilities. However, their operating principles rely upon direct, not indirect, measurements. Conceptually, they are only a few steps removed from a pinhole camera.

To see through the body, one must use wavelengths that penetrate the skin. Thus, x-ray radiation is the basis for CT, and RF radiation is the basis for MRI. However, such systems do not generate imagery using analogs to optical lenses. Instead, they use coded, indirect measurements and computation.

### 5.3a. Computed Tomography

X rays, discovered in 1895, can be transmitted through most materials. Their frequencies,  $3 \times 10^{16}$  to  $3 \times 10^{19}$  Hz, are such that the refractive index of most materials is approximately 1. Thus, the dominant effect on x rays as they traverse through a material is a change in amplitude, not phase, proportional to the density of material encountered. When applied to medical imaging, due to the higher density of bones and cartilage relative to soft tissue, the contrast of bones and cartilage in x-ray imagery is higher than soft tissue.

However, a single x-ray image is a projection of a three-dimensional spatially varying density function onto a two-dimensional detector. According to the Beer–Lambert Law [116], each point in the image corresponds to a line integral along the path of an x ray and is fundamentally not invertible. This can be overcome by making multiple measurements using redundant and non-redundant projections from which one reconstructs the imaged volume [117]. This is the essence of tomography, from the Greek for sliced record.

In CT, to form the image of a single two-dimensional plane in a body, an x-ray source with either a parallel or fan beam output is moved in a circular arc around the body. Measurements are made on a linear detector array that moves synchronously with the source [118,119]. To create a high-quality image of the trans-axial slice of the body, the one-dimensional projections are processed using backprojection. The backprojection algorithm is based on the 1917 mathematical work by Johann Radon [120,121], who showed that the Fourier transform of a linear projection through a two-dimensional function is equivalent to a slice through the Fourier Transform of the two-dimensional

function in a direction orthogonal to the projection. A CT scanner is represented schematically along with CT images in Fig. 11.

### 5.3b. Magnetic Resonance Imaging

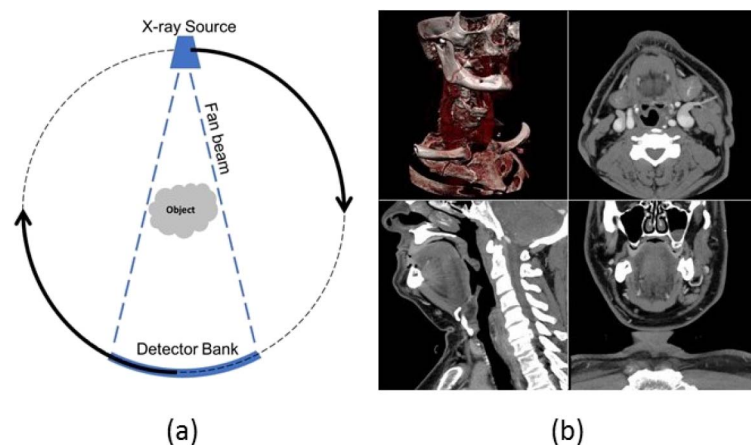
Whereas conventional imaging, including CT, is based on the volumetric material properties related to reflection, refraction, and absorption, MRI is based on the electromagnetic properties of hydrogen and, specifically, on the interaction of hydrogen nuclei in water and fat molecules with RF signals in the presence of strong static and dynamic magnetic fields [123,124].

An MRI system consists of three components: a static magnetic field, a dynamic magnetic field that produces a one-dimensional spatial gradient whose direction varies in time, and a source to produce a sequence of RF pulses. The magnetic fields encode spatial information by setting the resonant frequencies of hydrogen nuclei in the body. Each pulse of RF energy excites the nuclei briefly. The nuclei release the RF energy they absorbed, which is measured by RF detectors. The frequency at which the energy is detected indicates the spatial location from which it was transmitted, and the strength of the detected signal is proportional to the density of hydrogen nuclei at that location.

Although a three-dimensional gradient would allow one to encode an entire volume in a single measurement, practically this is difficult to achieve. Thus, scans through the volume are created using a sequence of one-dimensional gradients. The RF measurements thus correspond to a line integral in the direction of the magnetic field gradient, and post-processing techniques, such as filtered backprojection, are used to recover information about soft tissue characteristics.

The numerous degrees of freedom, e.g., in the static magnetic field, in the temporal variation of the magnetic field gradient, and in the pulse sequence of the probe RF signals, enable a variety of possible measurements. For example, one can minimize the measurement time, which is essential to create real-time video in functional MRI, or create tissue specific imaging modalities without external contrast agents. The hallmarks of MRI, the joint design of measurements and powerful reconstruction algorithms, indicate clearly MRI's computational philosophy.

**Figure 11**



Computed tomography. (a) Geometry for recording x-ray data used to generate CT images. (b) Representative CT image with cross-sectional slices and three-dimensional representation. Reprinted with permission from Wikipedia [122] Wikimedia Commons under the Creative Commons Attribution-Share Alike 3.0 license.

## 6. MOTIVATION 2: DIMENSIONALITY MISMATCH

From Section 4, the conventional relationship between object and image is a spatial mapping from one two-dimensional plane to another. In traditional systems, variations in color and object depth are treated as deviations from this base. Indeed, an aberration is defined as a deviation from the norm. Yet, natural scenes are intrinsically three-dimensional and multispectral. In this section, we discuss imaging applications in which conventional field parameters, such as wavelength, depth, and polarization, are considered information carriers instead of nuisance parameters to be ameliorated through design.

A change in perspective is appropriate at this point. A primary objective of computer graphics is rendering natural scenes realistically. Thus, as a matter of course, researchers in that field are confronted with the multidimensional and multispectral nature of optical fields. To do so in as compact a manner as possible, researchers employ a ray optics concept, the plenoptic function [125]. Given its simple and intuitive nature, we use it to introduce the applications in this section.

The plenoptic function assumes that a ray carries optical energy. At each point in three-dimensional space, a ray is characterized by its direction of propagation, encoded by azimuth and elevation angles,  $\theta$  and  $\phi$ , respectively. (These angles are related to direction cosines and spatial frequencies.) The addition of wavelength  $\lambda$  and polarization state  $\mathbf{P}$  yields a seven-dimensional plenoptic function  $L(x, y, z, \theta, \phi, \lambda, \mathbf{P})$ .

Since the plenoptic function in planes perpendicular to the optic axis are all related by geometry, we can reduce  $L$  by one spatial dimension. In fact, if one measures completely the six-dimensional plenoptic function at a single plane, it is a simple matter to propagate it computationally to any plane in free space, e.g., backward to the source or forward to the detection plane. For a fixed wavelength and polarization state, the four-dimensional plenoptic measurement known as the light field is conceptually and practically similar to the generalized radiance function defined by optical physicists who work with ray models of light. A radiance function is defined as the flux per unit area per solid angle as a function of wavelength, polarization and location in the plane transverse to propagation.

However, measuring a six-dimensional function using only a two-dimensional detector array presents numerous challenges. It is obvious that one approach to making these measurements is to record two-dimensional images as some instrument is scanned through one of the other independent variables, e.g., scan a spectrometer in two dimensions. However, in terms of resource utilization, this approach is not optimal. We, therefore, label imagers as computational if the measurements they make when scanning are indirect, as opposed to direct.

In this section, we discuss how to employ coded, indirect measurements to acquire different slices or projections of the six-dimensional plenoptic function. This includes spatial-spectral measurements  $(x, y, \lambda)$ , polarimetric measurements  $(x, y, \mathbf{P})$ , light-field measurements  $(x, y, \theta, \phi)$ , and, finally, measurements in three-dimensional space  $(x, y, z)$ .

### 6.1. Spatial-Spectral Imaging

Humans perceive their world as a panoply of color and luminance distributed spatially. Capturing this objectively is difficult. On one side, optical designers have spent centuries insuring that optical systems are chromatically insensitive so that images do not appear distorted due to color. This is in stark contrast to spectroscopists, who accentuate chromatic differences due to physics or material properties to measure the spectrum of an incident field with as high a frequency resolution as possible. Designing a

single optical system that has both high spatial resolution and high spectral resolution represents a dimensional mismatch. In this section we discuss methods to address this.

Attempts to record color began almost immediately after the invention of photographic film. In 1855, Maxwell proposed a method for color photography that used three different color filters [126]. The approach was based on the human visual system, which perceives color using three different retinal cones whose spectral responses peak in the blue, green, and red but are otherwise broad and overlapping. The photograph of “the tartan ribbon,” which Maxwell made collaboratively with Thomas Sutton in 1861, validated his approach and is acknowledged as the first color photograph.

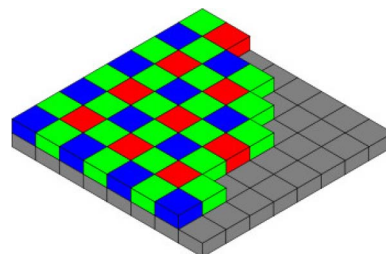
Kodachrome, introduced by Kodak in 1935, was based on a similar principle. It consisted of three layers of photographic emulsion, with each layer sensitized to the blue, green, and red spectral bands. Kodachrome was instrumental in mass marketing color photography.

With the advent of electronic detection, mimicking this layered approach electronically proved difficult to implement practically. In 1976, Bryce Bayer developed a solution by placing a mosaic of color filters in front of a semiconductor detector array [127]. See Fig. 12. Bayer assigned green filters to two photodetector pixels because human vision is more sensitive to green than it is to blue or red. The regular sampling and spatial offset between color channels in the Bayer filter introduces so-called mosaicking artifacts in measurements of objects that contain high spatial frequencies. Interpolation of the color channels in post-detection smooths out these artifacts. The design of the Bayer filter and de-mosaicking interpolation is an example of Computational Imaging, albeit simple in comparison to other coding methods.

Although the principles underlying the Bayer filter have recently been generalized for multi-band spectral imaging as well as high dynamic range measurements [129], the Bayer filter (and Kodachrome) essentially compress a scene’s spectrum into three broad color bands. To increase the frequency resolution, as opposed to collapsing the spectrum at every spatially resolvable point, requires spectral dispersion, which we discuss in the remainder of this section.

The goal of spatial-spectral imaging is to produce a data cube with two spatial dimensions and one wavelength (or spectral) dimension. If  $N_x$ ,  $N_y$ , and  $N_\lambda$  represent the number of resolvable points in the spatial dimensions  $x$  and  $y$ , and wavelength dimension  $\lambda$ , respectively, the cube has  $N_x N_y N_\lambda$  total elements. One wishes to make as few measurements as possible to fill the cube completely. As represented by line a in Fig. 13, one approach is to measure the spectrum at each point in space. That is,

Figure 12



Representation of a Bayer filter for electronic color detection. Reprinted with permission from Wikipedia [128] Wikimedia Commons under the Creative Commons Attribution-Share Alike 3.0 license.

perform a two-dimensional spatial scan with a spectrometer. This approach requires a one-dimensional detector with  $N_\lambda$  elements and  $N_x N_y$  measurement frames. The plane b indicates that one can also image spatially onto a  $N_x \times N_y$  two-dimensional detector using a sequence of  $N_\lambda$  spectral filters, such as a color wheel or an acousto-optic tunable filter (AOTF) [130]. Alternatively, plane c indicates it is possible to perform a spectral analysis of a line in one spatial dimension and scan in the orthogonal spatial dimension. In this case, the detector is  $N_\lambda \times N_x$  elements and  $N_y$  measurement frames are required. If  $N_y > N_\lambda$ , the detector for scheme b is larger than that for c but requires fewer measurement frames. We do not consider any of these scanning approaches computational.

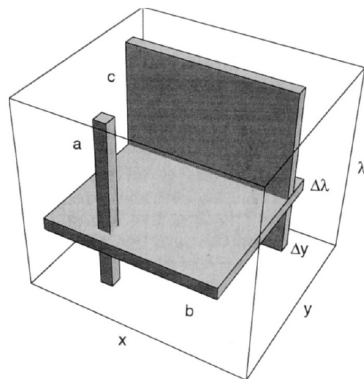
Instead, recent work shows how exploiting spectral dispersion can access information throughout the entire data cube [31,131–139]. The approaches essentially implement a polychromatic PSF,

$$i(x, y, \lambda) = |o(x, y, \lambda)|^2 * |p(x - S_x(\lambda), y - S_y(\lambda))|^2, \quad (39)$$

to reduce the number of measurement frames while improving spectral resolution. The first examples of this approach [31,131–133] exploited the highly dispersive nature of diffractive elements to generate multiple projections through the cube simultaneously. In a traditional diffraction spectrometer, diffraction is used to disperse the optical spectrum. The computed tomography imaging spectrometer (CTIS) is grounded in this capability, but, more importantly, it exploits information contained in the multiple diffracted orders generated by a diffractive element. As shown in Fig. 14(a), each diffracted order is a different projection through the spatial-spectral cube. Thus, the entire cube can be reconstructed using tomographic techniques. The data from a single CTIS measurement and subsequent reconstruction are shown in Figs. 14(b) and 14(c). The detector must be sufficiently large to detect several spatial images at once. The detector size relative to the image size,  $N_x \times N_y$ , determines the spectral resolution possible.

CTIS enhances the capabilities of conventional diffractive spectrometers by accessing additional spectral information contained in higher diffracted orders. But, without encoding, it does not use efficiently the information capacity available in the system. This is the approach taken by the research groups of Brady [134,135] and Arce [136–138]. Both coded aperture snapshot spectral imaging (CASSI) and the snapshot

**Figure 13**



Traditional approaches to filling a spatial-spectral cube. Reprinted with permission from [31]. Copyright 1995 Optical Society of America.

colored compressive spectral imager (SCCSI) use spectral encoding to improve performance. Both systems are reviewed in Ref. [139].

In CASSI, the input object spectrum is dispersed using a prism and the dispersed object is coded with a binary amplitude mask  $C(x, y)$ . The detected image is

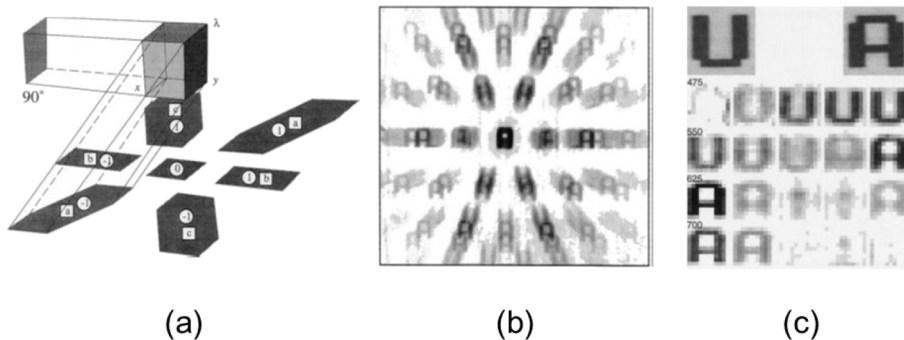
$$i(x, y) = \int [|o(x, y, \lambda)|^2 * |p(x - S(\lambda), y)|^2] C(x, y) d\lambda. \quad (40)$$

Just as coding improves the performance of communication systems in the presence of noise, spectral coding in CASSI enables a robust reconstruction of the spatial–spectral cube. The operation of SCCSI is similar to CASSI except the code spans the spatial and spectral dimensions:

$$i(x, y) = \int [|o(x, y, \lambda)|^2 * |p(x - S(\lambda), y)|^2] C(x, y, \lambda) d\lambda. \quad (41)$$

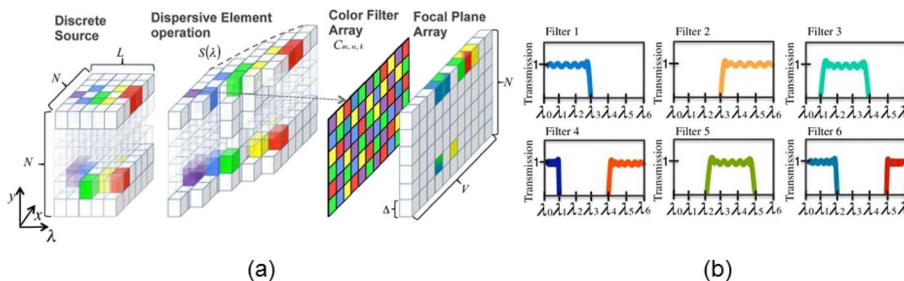
As indicated in Fig. 15, the coding mask contains a spectral filter at each spatial pixel.

Figure 14



CTIS principle and results. (a) Non-orthogonal projections of the spatial–spectral cube produced by the multiple diffracted orders. (b) Measurements and (c) spectral slices from a reconstructed spatial–spectral cube. Reprinted with permission from [31]. Copyright 1995 Optical Society of America.

Figure 15



Spatial–spectral imaging using spectral coding in combination with a dispersive element. (a) Schematic representation of operation. (b) Spectral bands used in SCCSI experiments.  $\lambda_0 = 448$  nm,  $\lambda_1 = 466$  nm,  $\lambda_2 = 487$  nm,  $\lambda_3 = 516$  nm,  $\lambda_4 = 550$  nm,  $\lambda_5 = 600$  nm,  $\lambda_6 = 663$  nm. Reprinted with permission from [137]. Copyright 2015 Optical Society of America.

The measurements recorded in a single frame are

$$\mathbf{M} = \mathbf{H}|\mathbf{O}|^2 + \mathbf{n}, \quad (42)$$

where

$$\mathbf{H} = \mathbf{P}\mathbf{\Gamma}\mathbf{D}, \quad (43)$$

with  $\mathbf{D}$  the dispersion matrix that accounts for spectral spreading induced by a prism,  $\mathbf{\Gamma}$  is the spatial–spectral coding matrix, and  $\mathbf{P}$  is the integration matrix that accounts for the spatial convolution of the imaging system. Because of dispersion, the system requires a detector that is  $N_y \times (N_x + N_\lambda + 1)$ . Consequently,  $\mathbf{H}$  is a  $N_y(N_x + N_\lambda + 1) \times N_x N_y N_\lambda$  matrix.

Experimental results from SCCSI are shown in Fig. 16. The SCCSI is shown in Fig. 16(a) and a panchromatic image of the scene used in the experiments in Fig. 16(b). The color filters used in the mask to code the input spectrum are represented in Fig. 15(b), and spectral bands reconstructed from experimental SCCSI measurements are presented in Fig. 16.

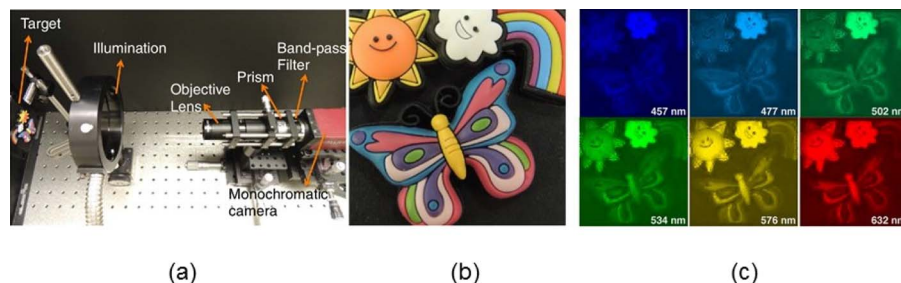
## 6.2. Three-Dimensional Imaging

Spatial–spectral imaging recognizes that resolvable points in a scene can have a complex chromatic spectrum due to the mix of materials in a small volume. In this section, we consider that these resolvable points exist in a three-dimensional world. However, one's interpretation of "three-dimensional imaging" can lead to markedly different imagers. For example, as we discussed under Motivation 1, it is not possible to image through a volume at optical wavelengths. It is possible, though, to image three-dimensional surfaces. We therefore consider two different interpretations of three-dimensional imaging, one in which the PSF is invariant to depth and one in which the variation in PSF as a function of depth produces a high-resolution measurement of a three-dimensional surface.

### 6.2a. Depth-Invariant Imaging

In conventional photography, a single plane in three-dimensional space is brought into focus. Objects in that plane are imaged with the resolution determined by the imaging optics. Objects in other planes perpendicular to the optical axis are degraded to a degree determined by the  $f\#$  of the optics. A lens with a large  $f\#$ , i.e., a small aperture, produces a gradual degradation or, equivalently, a large depth-of-field (DOF), defined

**Figure 16**



Experimental results from SCCSI. (a) Laboratory implementation. (b) Panchromatic image of scene used in experiments. (c) Experimentally recovered spectral bands from SCCSI measurements using filters 1–4 in Fig. 15(b). Reprinted with permission from [137]. Copyright 2015 Optical Society of America.

as the distances in depth between which objects are assumed in focus. However, a large  $f\#$  lens also reduces light collection and, therefore, signal information, which decreases the image SNR.

If the goal of three-dimensional imaging is to increase the DOF, one can capture multiple images as the focus is adjusted, segment each image into regions of best focus, and merge these regions into a single image. In the final image, all objects are in focus regardless of their location. This approach is best suited for a static scene. Dynamic scenes increase the likelihood of motion blur as multiple images are captured over time.

Alternatively, one can engineer the system PSF, or equivalently its OTF, so that it is invariant to misfocus over some range of object distances [28]. Consistent with the description provided in Ref. [28], a pupil function in normalized coordinates, given by

$$P(x) = \begin{cases} \frac{1}{\sqrt{2}} \exp(j\alpha x^3), & \text{for } |x| \leq 1, \\ 0, & \text{otherwise,} \end{cases} \quad (44)$$

introduces a uniform blur on the image when the constant  $\alpha$  is sufficiently large. More importantly, the corresponding OTF is relatively invariant to misfocus. This is evident in its approximate representation [28],

$$H(u, \psi) \approx \begin{cases} \left(\frac{\pi}{12|\alpha u|}\right)^{1/2} \exp\left(j\frac{\alpha u^3}{4}\right) \exp\left(-j\frac{\psi^2 u}{3\alpha}\right), & u \neq 0, \\ 1, & u = 0, \end{cases} \quad (45)$$

where  $\psi$  is the misfocus parameter,

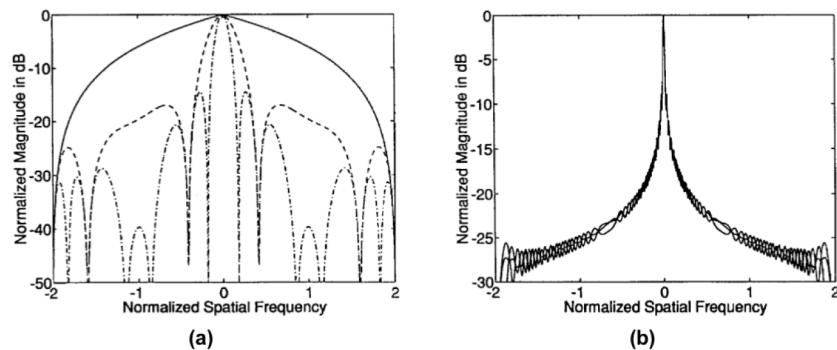
$$\psi = \frac{\pi L^2}{4\lambda} \left( \frac{1}{f} - \frac{1}{d_o} - \frac{1}{d_i} \right), \quad (46)$$

$L$  is the aperture size,  $d_o$  is the object distance, and  $d_i$  is the image distance. When  $\alpha$  is made large, the OTF becomes insensitive to  $\psi$ , and the approximation can be rewritten as

$$H(u) \approx \begin{cases} \left(\frac{\pi}{12|\alpha u|}\right)^{1/2} \exp\left(j\frac{\alpha u^3}{4}\right), & u \neq 0, \\ 1, & u = 0. \end{cases} \quad (47)$$

The focus invariance is illustrated in Fig. 17, where the MTF for a standard optical system is compared to that of a cubic phase element similar to Eq. (44) over a range of

Figure 17



Magnitude of the OTF with different amounts of defocus: (a) standard optical system with  $\psi = 0$  (solid curve),  $\psi = 15$  (dashed curve), and  $\psi = 30$  (dashed-dotted curve); (b) cubic phase element with  $\alpha = 90$  and  $\psi = 0, 15$ , and  $30$ . Reprinted with permission from [28]. Copyright 1995 Optical Society of America.

misfocus values. The blur introduced by the cubic phase element can be removed using simple image reconstruction methods. See Fig. 18.

The sensitivity to defocus can be decreased by increasing  $\alpha$ , but this reduces the SNR in the reconstruction due to suppression of high spatial frequencies. Nonetheless, regardless of the value of  $\alpha$ , the cubic phase utilizes the full aperture, which preserves light collection efficiency and the spatial cut-off frequency. Insensitivity to focus is not a property that is exclusive to the cubic phase function. Other pupil functions also exhibit similar invariance [140].

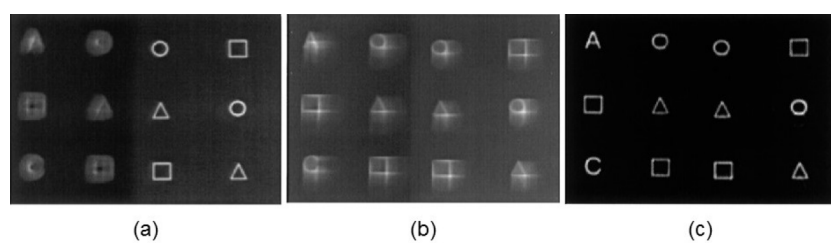
#### 6.2b. Depth Measurement

By collapsing planes over a range of depths into a single image, depth-invariant imaging essentially throws away the depth information. However, in some applications, the objective is to determine the range of objects in a three-dimensional scene. For this discussion, we do not consider methods that use proximate measurements of a surface, for example, those generated by deflections in a mechanical tip translated across a surface or even changes in electromagnetic fields measured by a near-field scanning optical microscope. Further, for natural scenes, we recognize it is possible to estimate depth using visual cues, such as shadows and perspective, contained in a single image. These methods identify physical features in the image and, knowing the camera location, use geometry to arrive at a result. Since these techniques are simply based on the forward model of a conventional imaging system, i.e., a conventional PSF and sampling function are assumed, we chose not to discuss them here. Likewise, we do not consider basic time-of-flight measurement systems, because such systems directly measure a simple temporal impulse response following a single reflection.

Instead, we consider in this section optical techniques for reconstructing a three-dimensional surface that are based on a forward model that has been engineered to enable the estimation of depth. Many of these are active because the external source provides either a phase reference [17,84,114,115] or a geometric reference [141–144]. Holography, for example, measures surface geometry by comparing the wavefront reflected by an object to a coherent reference wavefront [17,84].

One method for obtaining depth information involves controlling the spatial characteristics of the illumination. This is the approach taken in structured illumination, wherein the forward model is modified by applying a spatial code in the object plane [141–144]. Rather than relying upon time differences to determine depth, structured illumination methods determine depth from the deformations visible when a known pattern is projected onto a surface. See Fig. 19. A critical element in the processing is

Figure 18



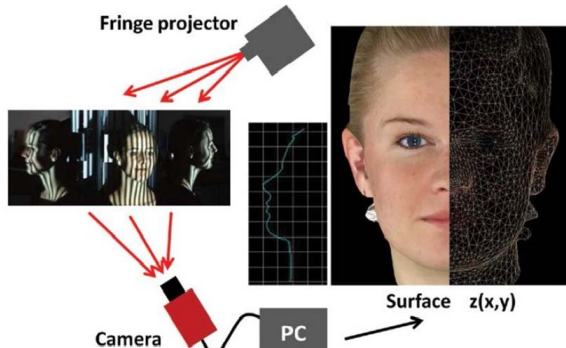
Experimental results comparing conventional imaging to cubic phase extended DOF. Images of two different object planes using (a) conventional imaging, (b) imaging with a cubic phase element and no processing, and (c) imaging with a cubic phase element and post-detection processing. Reprinted with permission from [30]. Copyright 1996 Optical Society of America.

associating each projected point to a point in the original pattern. However, such techniques are now sufficiently sophisticated that it is possible to create movies in real-time of three-dimensional surfaces [143].

Structured illumination describes an active illumination method of recovering depth. However, other methods have been demonstrated that rely only on passive or ambient illumination. With reference to conventional imaging to a single detector plane, for each object plane there exists a unique PSF. Theoretically, one can use estimates of these PSFs to determine the depth at which a specific object point yields the image recorded. Not only does this approach require precise knowledge of the PSFs, it requires considerable effort to match response estimates to measurements. These problems are reduced if one engineers a PSF to enhance depth dependence [145,146], such as the double-helix PSF represented in Fig. 20. The double-helix PSF contains two laterally separated points whose separation and angular orientation relative to the optic axis are functions of depth. By estimating the scale and angle of the optical response in an image, one can determine object depth. The double-helix PSF is significant for its optical design. It is also a good example of how to use Fisher information in optical design, as well as the Cramer–Rao bound to validate the improvement in depth precision over other PSFs [147].

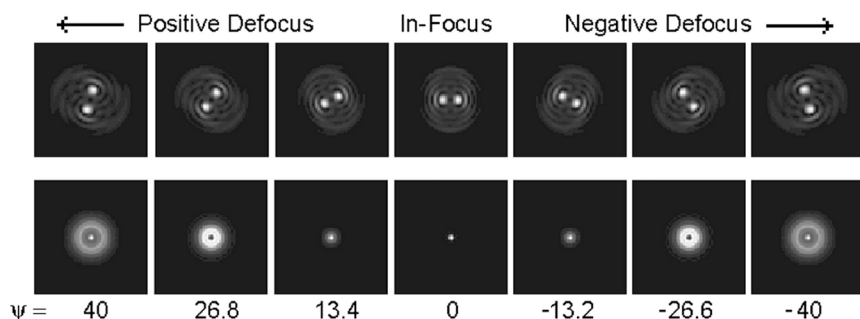
We note the complementary nature of the objectives for depth-invariant versus depth-sensitive imaging. The optical responses of the cubic phase and double-helix

**Figure 19**



Structured illumination. Reprinted with permission from Häulser and Willomitzer, Int. Commission Opt. Newsletter **104**, 1–5 (2015) [141].

**Figure 20**



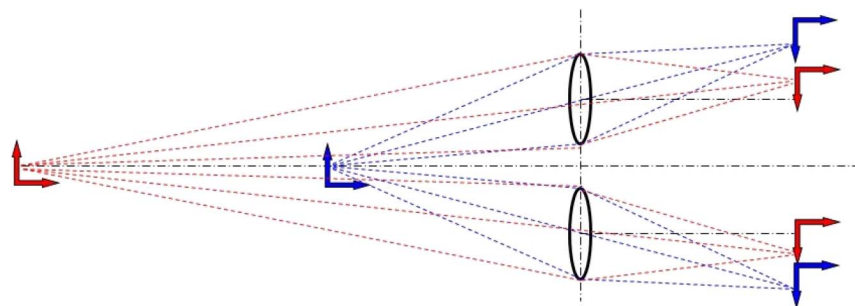
Double-helix PSF compared to the conventional PSF of a circular aperture as a function of misfocus. Reprinted with permission from [145]. Copyright 2006 Optical Society of America.

demonstrate the power of PSF engineering in Computational Imaging. In fact, using the two systems in parallel can potentially allow one to apply the double-helix to extended objects and not just to a sparse collection of discrete point sources [146].

One of the oldest passive techniques for capturing depth is stereoscopic photography. Inspired by human stereo vision, these systems record two images of a three-dimensional scene. Each image is displaced laterally by an amount proportional to the object's distance from the imagers measured along the optic axis. As shown in Fig. 21, this relationship derives from simple geometry. The precision in depth measurement depends upon the separation between the two imagers. To determine depth from these images requires that one determine the correspondence between object points in both images. It is remarkable how effortlessly humans can do this.

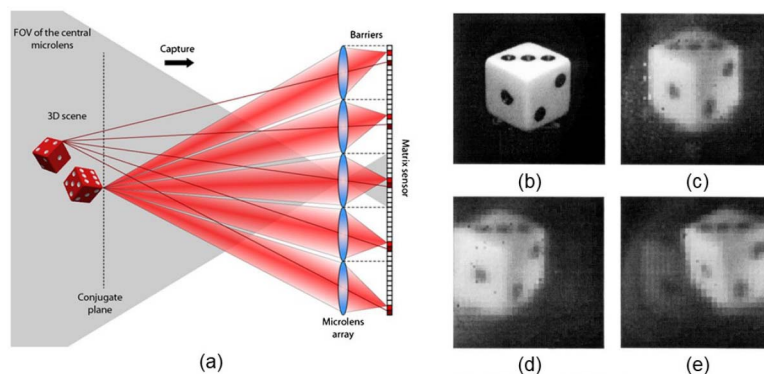
Given the difficulties in determining depth from only two images, it makes sense that they can be reduced using multiple images. This is the principle behind integral imaging [148–151]. Integral imaging uses a microlens array to form images of a single scene from many perspectives. See Fig. 22. The technique was introduced by Nobel laureate Gabriel Lippmann in 1908 [148]. Computational reconstruction is achieved via backprojection of multiple two-dimensional projections. The spatial resolution of the reconstructed image is determined by the resolution of each subimage formed by

**Figure 21**



Representation of stereoscopy.

**Figure 22**



Integral imaging. (a) Schematic representation of measurement. Reprinted with permission from [151]. Copyright 2013 Optical Society of America. (b) Original object. (c)–(e) Digital reconstructions from different angular perspectives. Figures (b)–(e) reprinted with permission from [149]. Copyright 2001 Optical Society of America.

an individual microlens. The depth resolution is determined by the pair of subimages with the longest baseline, which is a function of the array geometry and size.

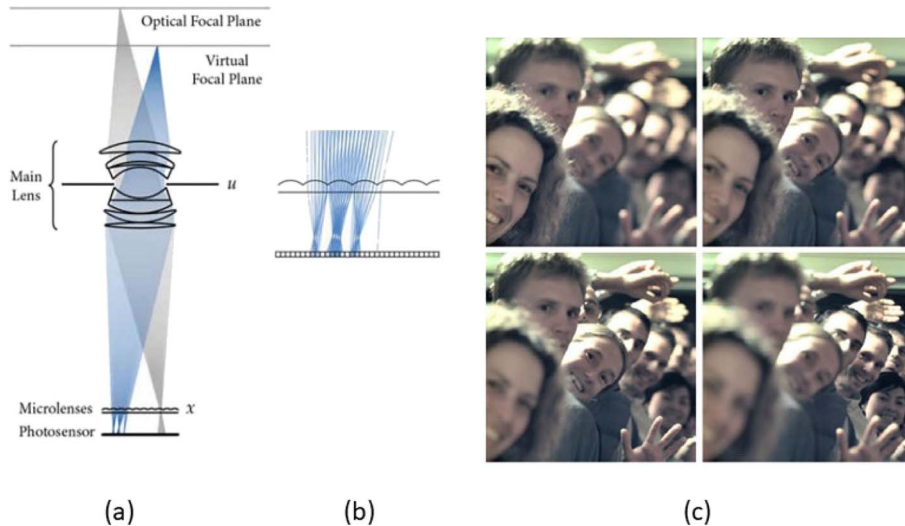
The light-field camera [152–156] depicted in Fig. 23 uses an alternate approach to encode depth. It consists of a single objective, as opposed to a microlens array in an integral camera, followed by a large format microlens array. The microlens array effectively images the pupil plane of the objective lens onto the focal plane array. Since the position of the ray on the pupil plane encodes its directional cosines, the detector pixel location underneath a microlens corresponds to the direction cosine value. The spatial format of the captured and reconstructed image is limited by the size of the microlens array and not the space-bandwidth of the objective or focal plane array. As mentioned in the introduction to this section, knowledge of the light field in a single plane allows reconstruction of the light field elsewhere. It is then possible, for example, to define computationally in post-detection the desired focal plane. This is shown in Fig. 23(c).

### 6.3. Polarization Imaging

In this last section, we consider imaging a wavefront for which the scalar assumption is no longer valid, namely, polarized fields. Polarized fields exhibit a strong dependence upon the orientation of the electric field. Fields can become polarized upon reflection by or transmission through objects.

Given the vectorial nature of polarization, one can argue that this discussion belongs under Motivation 1. Our primary reason for placing it under Motivation 2 is that polarization is a classical property of an optical field. That is, with appropriate filters, its effects can be made visible even in a single measurement of a single object point. The fact that derivation of the complete polarization state at a single point requires several measurements underscores the mismatch between measuring a three-dimensional vectorial field with a two-dimensional detector. Thus, similar to the temporal and spatial frequencies of a wavefront, we classify polarization as an independent parameter in the plenoptic function.

**Figure 23**



Light-field imaging. (a) Imaging optics. (b) Detail of imaging optics using a microlens array. (c) Computational refocusing using light-field data. Figures reprinted by permission from Ng *et al.*, “Light field photography with a hand-held plenoptic camera” (2005) [152] and R. Ng, “Digital light field photography” (2006) [153].

The polarization state of a field is commonly expressed by the Stokes vector [157]

$$\mathbf{S}(x,y) = [S_0(x,y) S_1(x,y) S_2(x,y) S_3(x,y)]^T, \quad (48)$$

where, in terms of vector field components  $E_x(x,y,t)$  and  $E_y(x,y,t)$  with a phase angle  $\gamma$  between them,

$$S_0(x,y) = \langle E_x^2(x,y,t) \rangle + \langle E_y^2(x,y,t) \rangle, \quad (49)$$

$$S_1(x,y) = \langle E_x^2(x,y,t) \rangle - \langle E_y^2(x,y,t) \rangle, \quad (50)$$

$$S_2(x,y) = 2\langle E_x(x,y,t)E_y(x,y,t) \cos \gamma \rangle, \quad (51)$$

$$S_3(x,y) = 2\langle E_x(x,y,t)E_y(x,y,t) \sin \gamma \rangle, \quad (52)$$

and angle brackets indicate time average. At a single point in space, modulation of a polarized field by an object is represented by the  $4 \times 4$  Mueller matrix  $\tilde{\mathbf{M}}$ :

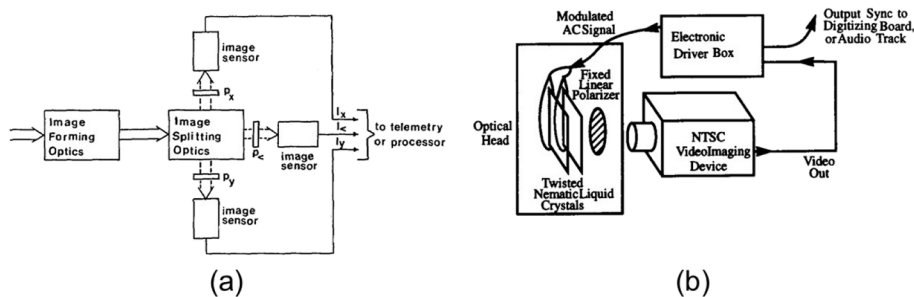
$$\mathbf{S}_{\text{out}}(x,y) = \tilde{\mathbf{M}}(x,y)\mathbf{S}_{\text{in}}(x,y). \quad (53)$$

Although the Stokes vector consists of four elements, it is possible to determine the unknown vector amplitudes and angle between them by making three measurements using a linearly polarized analyzer in an imaging system. For a polarizer oriented at an angle  $\alpha$  in front of a detector, the irradiance measurement is

$$i(x,y,\alpha) = \left(\frac{1}{2}\right)[S_0(x,y) + S_1(x,y) \cos 2\alpha + S_2(x,y) \sin 2\alpha]. \quad (54)$$

As indicated in Fig. 24, one can make the three measurements required to determine the Stokes parameters  $S_0(x,y)$ ,  $S_1(x,y)$ , and  $S_2(x,y)$  either in space [157–163] or in time [164–166]. One uses linear algebra to determine the Stokes parameters from the intensity measurements.

Figure 24



Architectures for polarization imaging. (a) Spatial multiplexing. Reprinted with permission from [157]. Copyright 1981 Optical Society of America. (b) Temporal multiplexing. Reprinted from Image Vision Comput. 15, L. B. Wolff, “Polarization vision: a new sensory approach to image understanding,” 81–93. Copyright 1997, with permission from Elsevier [165].

Reviews of imaging polarimetry appear in Refs. [167,168]. Its advantage over conventional imaging is evident in Fig. 25. Figure 25(a) is a panchromatic recording of a scene in the visible spectrum and Fig. 25(b), a recording in the IR spectrum. Figure 25(c) is an IR polarimetric recording that reveals two trucks under the foliage. In the visible spectrum, the trucks are obscured by the foliage, and, since the trucks have not been used recently, they are not evident in the IR spectrum. However, because the metal surfaces of the trucks polarize the reflected IR waves, they are visible in the imaging polarimeter.

As a vector field, polarization-based imagers are limited in their ability to make multiplexed encoded measurements. The trade-offs encountered by designers in the different designs are conventional ones. Temporal approaches use a  $N_x \times N_y$  detector array and sacrifice temporal resolution to create a single image. Spatial approaches trade resources in the space-bandwidth. One can use division of amplitude to split the imager into three channels, one for each angle of the polarized analyzer. This requires three  $N_x \times N_y$  detector arrays and the ability to register the images. Equivalently, one can use a single  $N_x \times N_y$  detector array and reduce the space-bandwidth available for imaging by one-third. One can do this using polarizers in the pupil plane [160–162], which ensures measurements are co-registered, or in the focal plane using diffraction gratings [158,159] or thin films [163] to integrate polarizers into a detector array. The former approach requires a  $2 \times 2$  super-pixel to create a single polarized image, which reduces spatial resolution. This approach is similar in spirit to the Bayer filter for spatial-spectral imaging.

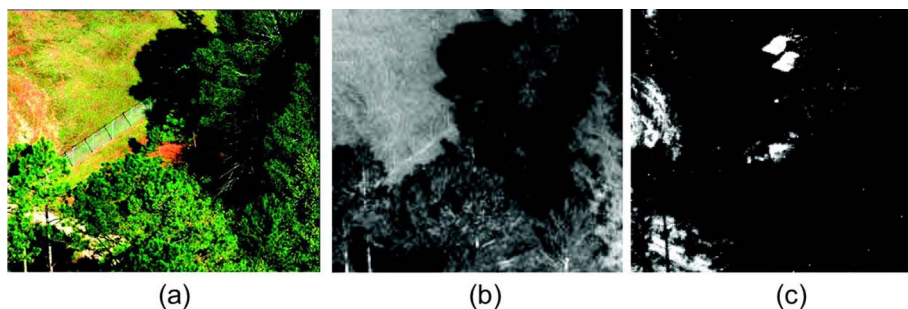
Finally, because polarization is a dimension that is orthogonal to space and temporal frequency, it is possible to include polarization channels to both three-dimensional imaging and spatial-spectral imaging. How one does this in an efficient and effective manner depends upon the imaging resources available to an optical designer.

## 7. MOTIVATION 3: REDUCING MEASUREMENT MARGINAL COSTS

The primary design goal under Motivation 3 is to reduce the costs to make a measurement, or otherwise increase its value, relative to that for a conventional measurement. In contrast to Motivations 1 and 2, Motivation 3 is driven primarily by advances in technology. The most important of these are illumination, optics, detection, processing, and integration.

The imagers presented in this section are divided into two fundamental categories. The first category includes applications that may be physically possible using conventional

**Figure 25**



Polarization imaging of trucks in foliage. (a) Panchromatic visible image. (b) Long wave IR image. (c) Polarization image of (b). Reprinted with permission from [168]. Copyright 2006 Optical Society of America.

imaging methods, but whose implementation is impractical due to challenging constraints imposed by physics. The second category includes applications in which conventional imaging is not only possible, but represents the norm. In these cases, Computational Imaging offers some advantage over a conventional approach, such as lower data rates or reductions in size, weight, power, or cost. We present representative examples of these two categories in the following subsections.

### 7.1. Possible but Impractical

In some cases, it may be physically possible to conceptualize and design a system to achieve an imaging task, but the physics governing the application yields a system too impractical to implement. Under such circumstances, changing the measurement and using computation to arrive at the result offers considerable advantage. We present synthetic aperture radar and coded-aperture imaging as examples in which wavelength-dependent physics makes it impractical to achieve an imaging system using conventional apertures.

#### 7.1a. Synthetic Aperture Radar

In its native form, radar is a sensor that measures the angle and range to an object. The spatial resolution of radar is limited by the same fundamental laws that limit the resolution of a single lens reflex camera and a cellphone camera. Specifically, the resolution is proportional to the wavelength and inversely proportional to the diameter of the collection aperture. To resolve a 10 cm diameter object at a 1 km range with an optical system (assuming a nominal operational wavelength of 0.5  $\mu\text{m}$ ) requires a 12 mm diameter aperture. However, radar systems operate at wavelengths that range from as long as 100 m down to a few millimeters. To achieve the same resolution (10 cm at 1 km) using even a short wavelength radar requires a 100 m aperture. Thus, although it is, in principle, possible to design and even construct such a system, it is not very practical, particularly if the radar is intended for use on an aircraft- or ground-based mobile platform. (A space-based implementation is conceivable but, nonetheless, fraught with challenges.)

Synthetic aperture radar (SAR) [169] uses computational methods to synthesize a coherent aperture and, thereby, overcome limitations on aperture size to form high-resolution radar images. Like our discussion of holography in Section 5, SAR is arguably an example of Computational Imaging that existed well before the term was used. In fact, the demonstration of SAR is linked to the development of off-axis holography [15]. SAR principles are based on encoding phase coherently on a spatial carrier in a manner similar to holography and the first post-detection SAR processor was a coherent optical system for reading off-axis holograms.

The pioneering principles to overcome the resolution limitations of radar originated in coherent radar and Doppler beam shaping [170], which led to the concept of a synthesized aperture [169]. (See Ref. [171] for a detailed tutorial on SAR.) This is accomplished by collecting multiple, spatially displaced measurements using a single physical aperture, as depicted in Fig. 26 for a moving radar platform, and synthesizing a virtual radar aperture from those measurements.

Raw SAR data bears no resemblance to a conventional image. Instead, it is an encoded representation of amplitude and phase measurements made by the radar and stitched together over the space of the virtual aperture. Because the system uses a single coherent reference, it is possible to combine measurements from multiple apertures coherently and, thereby, create a single large aperture. An image results when the encoded data is Fourier transformed. Although the first SAR images were created using a lens to perform the necessary transform, presently, SAR data is transformed

electronically. The resulting SAR image has a resolution limited by the dimensions of the virtual aperture,  $L_{sa}$ :

$$L_{sa} = \frac{\lambda r_o}{D_a}, \quad (55)$$

where  $D_a$  is the length of the physical aperture. The resolution of the synthetic aperture is then given by

$$\delta_{sa} = \frac{\lambda r_o}{2L_{sa}} = \frac{D_a}{2}. \quad (56)$$

The factor of 2 in Eq. (56) results from the path length due to transmission and reception. Therefore, by imaging, as opposed to measuring just range and angle, SAR provides a practical solution to overcome some of the performance limitations of conventional radar, while retaining some of its advantages, including day, night, and all-weather operation.

### 7.1b. Coded-Aperture Imaging

Our second example of Computational Imaging motivated by the impracticality of conventional approaches is coded-aperture imaging. It also was developed before the term Computational Imaging came into use, in particular, to solve some of the challenges faced in  $\gamma$ -ray and x-ray imaging. As mentioned previously, at  $\gamma$ - and x-ray wavelengths, the refractive index of most materials is approximately 1. Thus, fabricating conventional imaging elements, such as lenses and mirrors, is difficult and expensive. A solution to this limitation is to form an image using a pinhole. But, because pinholes are mostly opaque, they are inefficient light collectors. Thus, one is forced to accept long data acquisition times or poor signal-to-noise conditions in the resulting images.

As an alternative to a lens or a pinhole, a binary coded mask,  $P(x, y)$ , can be placed in the imaging aperture [172,173]. Since diffractive effects are minimal at these

**Figure 26**

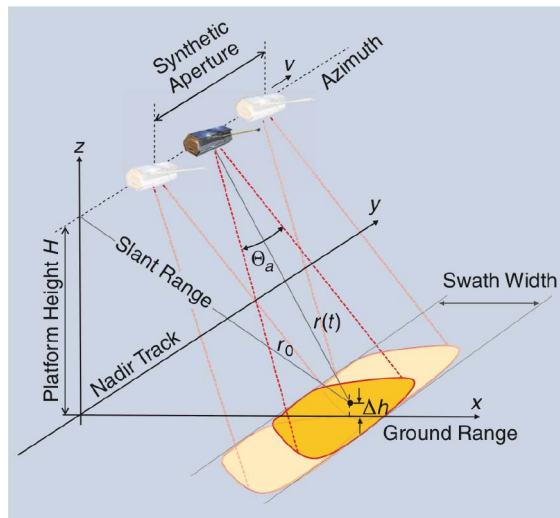


Illustration of synthetic aperture radar on a platform moving in the direction of  $v$ . The initial range is given by  $r_o$ , and the range after time  $t$  is  $r(t)$ . The beamwidth of the radar is  $\Theta_a$ . © 2013 IEEE. Reprinted with permission from Moreira *et al.*, IEEE Geosci. Remote Sens. Mag. 1(1), 6–43 (2013) [171].

wavelengths, the system PSF is essentially a projection of the mask, not its transform. The resulting image is the superposition of the aperture code with the object:

$$i(x, y) = |o(x, y)|^2 * *P(x, y). \quad (57)$$

See Fig. 27.

Although the recorded image may be barely recognizable, an image of  $o(x, y)$  can be recovered by convolving it in post-detection with a filter design based on *a priori* knowledge of  $P(x, y)$ :

$$\begin{aligned} o'(x, y) &= i(x, y) * *T(x, y), \\ &= |o(x, y)|^2 * *[P(x, y) * *T(x, y)]. \end{aligned} \quad (58)$$

If  $P(x, y) * *T(x, y) \approx \delta(x, y)$ ,  $o'(x, y) \approx |o(x, y)|^2$  [173]. Thus, a coded aperture can be used to produce  $\gamma$ -ray and x-ray imagery as effectively as a pinhole with a substantial improvement in acquisition time, SNR, or both.

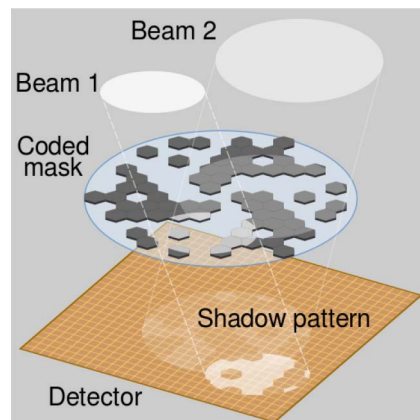
This method of imaging  $\gamma$  rays or x rays was pioneered by the astronomy community (see, for example, [172]), and several coded-aperture systems have been implemented. Coded apertures have also found application in medicine and environmental monitoring [175,176]. A review of coded-aperture imaging systems can be found in Ref. [177].

## 7.2. Possible but Not Optimal

We continue our discussion of the third motivation for Computational Imaging with applications that are entirely possible using conventional methods. The motivation for Computational Imaging in these cases is to achieve some advantage over a conventional approach.

In each of these applications we note the use of active versus passive illumination. Active illumination provides control over the imaging environment and the ability to manipulate the appearance of an object. Active illumination is found in medical

**Figure 27**



Example of a hexagonally uniform redundant array coded aperture. Light from different points in the field and incident on aperture cast spatially shifted projections of the aperture onto the focal plane. Reprinted with permission from Wikipedia [174] Wikimedia Commons under the Creative Commons Attribution-Share Alike 3.0 license.

imaging, diagnostics, quality control, and cooperative security. In contrast, passive illumination relies completely on ambient or natural sources of light, i.e., there is no control over the environment or the object. Passive illumination is widespread, and most common in photography, but specific applications include astronomy, surveillance, and non-cooperative security.

### 7.2a. Superresolution

The relationship between aperture size and resolution in a single image is a fundamental one that is difficult to overcome. With the advent of practical optical holography and the introduction of information processing ideas into imaging, it was recognized that structured illumination and the production of moiré fringes can be used to homodyne high spatial frequency content so that they can be resolved by an imager [178]. This technique does not alter the resolution limits. Instead, it modifies the object so that structure that would otherwise be unresolvable is resolved. However, the reverse is also true. Structure that would otherwise be resolvable is now rendered unresolvable. More recently, it has been shown that the displacement between a structured illumination projector and an imager can also be used to extract depth information from a scene with high lateral spatial resolution [144].

Iterative methods similar to phase retrieval were proposed in the 1970s and 1980s to overcome this fundamental limitation on resolution in passive imaging [179–182], but only marginal results were obtained due, primarily, to noise limitations. Active illumination in combination with multiple images introduces more degrees of freedom, which enables information to be extracted from a single image that is beyond conventional physical limits.

We now present two active approaches to increase resolution in microscopy. The first [183–185] changes the measurement from one of resolution to localization and uses statistical post-detection processing to generate a PSF whose width is less than the resolution limit set by the microscope's aperture. The second method [186,187] performs a series of source-coded measurements of a scene and uses phase retrieval to combine the measurements coherently. A third example that we do not explicitly include in the discussion below, but that deserves to be mentioned, is represented by the work of Gustafsson [188,189]. In Gustafsson's work, spatially structured illumination is used to achieve lateral resolution with a microscope that significantly exceeds the classical diffraction limit.

It is also worth noting that one could argue this section on superresolution methods fits equally well under Motivation 1 or Motivation 3. However, we have made the choice to include it here.

#### *Superresolved Fluorescence Microscopy*

As mentioned in Section 3, the first recorded compound optical instrument was the microscope, invented in 1590, and many imaging principles were derived based on applications in microscopy. The microscope is now a standard scientific instrument in medicine, biology, chemistry, and material science. As is the case for all conventional imagers, the resolution of a microscope with light of wavelength  $\lambda$  in a medium with refractive index  $n$  is limited by the Abbe diffraction limit:

$$\Delta \geq \frac{\lambda}{2n \sin \theta}, \quad (59)$$

where  $2\theta$  is the angle defined by the optical aperture and the point being imaged. The lower limit on  $\Delta$  is approximately half the illumination wavelength (approximately

250 nm in the visible spectrum), which can be 2 orders of magnitude larger than the physical scale of interest for some molecules.

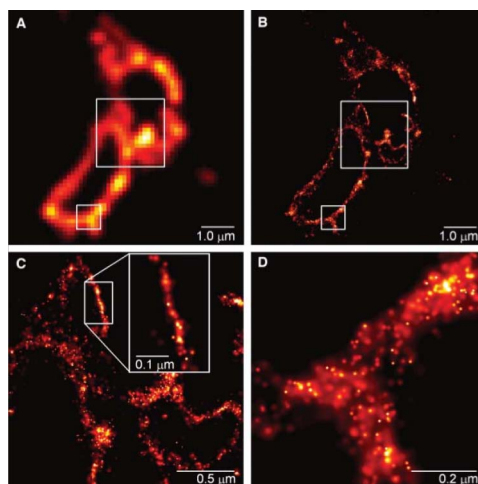
To image nanometer scale objects using visible illumination requires changing the measurement. For example, by using *a priori* information in post-detection estimation, it is possible to *localize* an object point with nanometer precision even when it is not possible to resolve features at this scale. This is the approach taken by Eric Betzig, Stefan Hell, and William Moerner, who shared the 2014 Nobel Prize in Chemistry for their contributions to superresolved fluorescence microscopy (SRFM) [183].

In fluorescence microscopy, a narrowband source illuminates a sample to induce fluorescence in a biological molecule. In a conventional microscope, the source of the fluorescent emission is imaged. In SRFM, the fluorophore is first imaged, and then localized more precisely using statistics of the photon distribution to define the PSF. A particular approach to SRFM, photo-activated localization microscopy (PALM), is explained in Refs. [183,184] and illustrated in Fig. 28.

SRFM relies on the activation of a sparse subset of molecules at one wavelength (e.g., 405 nm) that are imaged at a second wavelength (e.g., 561 nm) until most of the illuminated molecules are bleached. A different sparse subset of molecules is illuminated to produce a second image, and the process is repeated until the entire sample is inactive. Therefore, active illumination is used to select molecules in a particular subset, and each subset of molecules is distributed so that all molecules in the set can be optically resolved. In the example of [183], this is achieved by insuring the distance between molecules is greater than the diffraction limit. Extensions to methods such as stochastic optical reconstruction microscopy (STORM), have enabled additional capability and allowed this condition to be relaxed [185].

Simply summing all measurement frames would result in a diffraction-limited image of the entire sample. However, using photon statistics, it is possible to locate the PSF with a higher precision than that predicted by Rayleigh's two-point criterion. This is possible if one assumes each molecule is a point source and that the probability

Figure 28



Comparison of images produced using (A) total internal reflection fluorescence microscopy and (B) photo-activated localization microscopy. (C) Close-up of the large boxed region in (B) demonstrates molecular localization at approximately 10 nm. (D) Close-up of the small boxed region in (B). From Betzig *et al.*, Science 313, 1642–1645 (2006) [184]. Reprinted with permission from AAAS.

density of photons arriving at the focal plane from that point source is approximately Gaussian [190]:

$$p(x, y) \approx C \exp \left[ -\frac{(x - \mu_x)^2}{2\Delta^2} - \frac{(y - \mu_y)^2}{2\Delta^2} \right]. \quad (60)$$

The term  $C$  is a normalization constant, and  $(\mu_x, \mu_y)$  are the center coordinates of the probability density of photons. The standard deviation of the distribution, which is a measure of the uncertainty in  $(\mu_x, \mu_y)$ , is related to the diffraction limit  $\Delta$  defined in Eq. (59). The minimum uncertainty in estimating the center  $(\mu_x, \mu_y)$  of the PSF  $p(x, y)$  scales with the number of photons collected  $N$ :

$$\Delta_{\min} = \frac{\Delta}{\sqrt{N}} = \frac{\lambda}{2\sqrt{N}n \sin \theta}. \quad (61)$$

Therefore, the error in estimating the centroid location of the molecule is less than the Abbe diffraction limit by a factor of  $1/\sqrt{N}$ . A superresolved image is constructed by combining individually superresolved frames. In this way, SRFM uses post-detection estimation and statistics, instead of optics, to overcome the resolution limit set by diffraction in conventional microscopes.

#### *Fourier Ptychography Microscope*

The design of microscope optics inherently limits the sample size that can be imaged at the required resolution. Stated another way, the aperture size and field-of-view (FOV) limit the SBWP. To increase SBWP, the optics can be redesigned to increase the aperture, the FOV, or both. Unfortunately, this increases optical aberrations, which compromises resolution, and mitigating these aberrations to meet design requirements typically increases the cost of the optics. Alternatively, the sample can be mechanically scanned to increase SBWP. But this requires a translation system with precise position control. Further, mechanical scanning increases only the effective FOV. It provides no improvement in resolution.

In contrast, as opposed to scanning in space, a Fourier ptychography microscope (FPM) overcomes the limits of SBWP using Fourier space encoding to scan a sample with structured illumination [186,187]. Typical FPM illumination consists of an array of light-emitting diodes (LEDs) in the source plane. One measures a sample by illuminating it sequentially using different LEDs in the array.

The essence of FPM source plane encoding is the assumption that illumination from a single LED creates a plane wave incident on the sample at an angle related to the LED's position in the array. Changing the location of the LED changes the angle of illumination. If one assumes the PSF remains unchanged, the shift in source position shifts the location of the coherent transfer function in the Fourier plane. Thus, using a sequence of illumination patterns allows one to make measurements of a sample from different portions of the Fourier plane. Using phase retrieval methods [38–40,91,92], images acquired with different illumination angles can be coherently combined to reconstruct a high-resolution image. The process of reconstruction is represented in Fig. 29 and described in the following steps [186].

In the first step, one defines the Fourier space of the desired high-resolution image by Fourier transforming an initial estimate of the image:

$$G_h = \sqrt{I_h} \exp(i\phi_h). \quad (62)$$

For example, one option would be to start with  $\phi_h = 0$  and set  $I_h$  equal to any up-sampled low-resolution image, or even an image of constant values. In Step 2,

the transform of  $G_h$  is filtered using the coherent transfer function of the microscope objective applied to the regions that correspond to the plane waves in the first illumination pattern. The filtered result is inverse transformed to form a low-resolution image:

$$G_l = \sqrt{I_l} \exp(i\phi_l). \quad (63)$$

The intensity measurement  $I_m$  made using the LED that corresponds to the plane wave incidence angle replaces  $I_l$  to form an estimate of the image:

$$G'_l = \sqrt{I_m} \exp(i\phi_l). \quad (64)$$

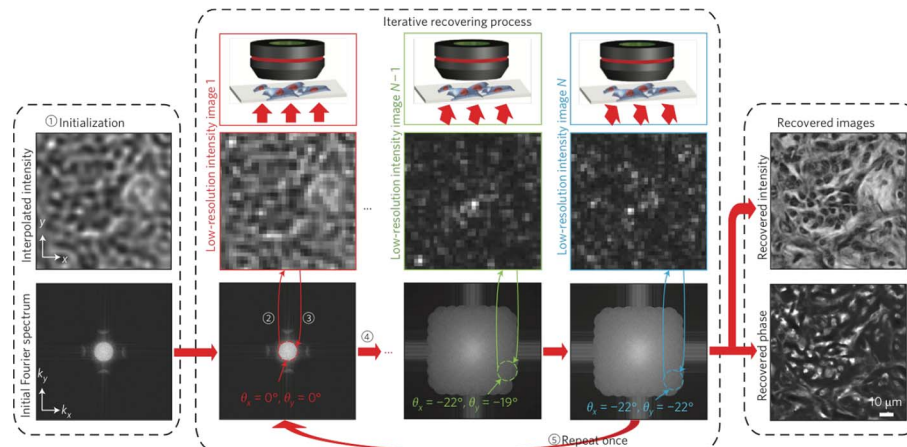
The image  $G'_l$  is again transformed and filtered to complete Step 3. The result produces a patch in Fourier space of a high-resolution image that corresponds to the region defined by the filter used in Step 2. Step 4 repeats Steps 2 and 3 for all of the remaining incidence angles associated with the LED array to produce a new estimate of the high-resolution image  $G_h$ . Steps 2–4 are repeated until the results are consistent.

In this way, it is possible to recover a high-resolution intensity image and a high-resolution phase image with a large FOV and a larger SBWP relative to the SBWP of the underlying conventional microscope. In contrast to SAR, which requires a single reference to synthesize a large coherent aperture, FPM relies on phase retrieval to coherently combine a set of intensity images. The images are generated coherently, but coherence does not exist between the individual intensity images. An additional constraint on the phase of each intensity image allows them to be combined coherently.

### 7.2b. Increased Temporal Resolution

Capturing motion can present certain challenges for imaging. In particular, motion that translates across multiple pixels in a single exposure will produce smearing,

**Figure 29**



FPM image reconstruction. Step 1: Initialize a high-resolution image. Step 2: Generate a low-resolution image by filtering the high-resolution estimate using the Fourier response for the first illumination pattern. Step 3: Replace the amplitude of the low-resolution image using the intensity measurement from the corresponding pattern and update the corresponding region of Fourier space. Step 4: Repeat Steps 2 and 3 using measurements from all patterns. Step 5: Repeat Steps 2–4 to refine the estimate of the high-resolution image. Reprinted by permission from Macmillan Publishers Ltd.: Zheng *et al.*, Nat. Photonics 7, 739–745 (2013) [186]. Copyright 2013.

or motion blur, in the resulting image. The problem becomes more severe as the velocity of motion increases. One approach to reduce motion blur is to reduce the sensor integration time such that it effectively freezes motion, i.e., until movement on the focal plane array is insignificant compared to the pixel dimensions. However, the amount of light collected scales with integration time. Therefore, SNR requirements of the application will place a lower limit on the integration time. If the illumination level can be controlled, this limit can be relaxed to some extent. But illumination control is not always an option.

Motion blur in one dimension can be represented by convolution with a rectangular PSF, which produces a sinc-function multiplication in the frequency domain. The effective bandwidth of the sinc-function scales inversely with the width of the PSF, which is proportional to the sensor exposure time and the motion velocity. Reconstruction of an image using deconvolution techniques is difficult due to the ill-conditioned forward model. High spatial frequency content is lost, and nulls exist at periodic intervals due to the sinc-function. Algorithms based on iterative maximum-likelihood estimation methods are sometimes used when the motion is global and uniform. However, such methods do not work well when, for example, the motion is localized, as in the case of a single object moving through a stationary scene.

One approach to overcoming this problem is to oscillate the imager's position to freeze moving objects in a scene [191,192]. Heuristically, given the imager acceleration, at some point in time the velocity of the imager matches that of the moving object. Moving the imager on a circular path allows one to freeze any motion within a two-dimensional plane. However, this approach does not modify the imaging optics.

Alternatively, since the temporally encoded PSF of a moving object maps exposure time to spatial translation, one can temporally engineer this PSF [193]. For example, one can impose a temporal code on the camera shutter during a single integration time that removes zeros in the corresponding OTF and preserves high spatial frequencies. Reconstruction of an image with motion blur removed requires one to invert the transfer matrix associated with the exposure code. The fidelity of image reconstruction is dependent upon the transfer matrix condition number. Figure 30 compares results of using a short exposure to freeze motion, a long exposure to improve SNR, a code based on a modified uniformly redundant array (MURA), and a custom code.

### 7.2c. Form Factor Constraints

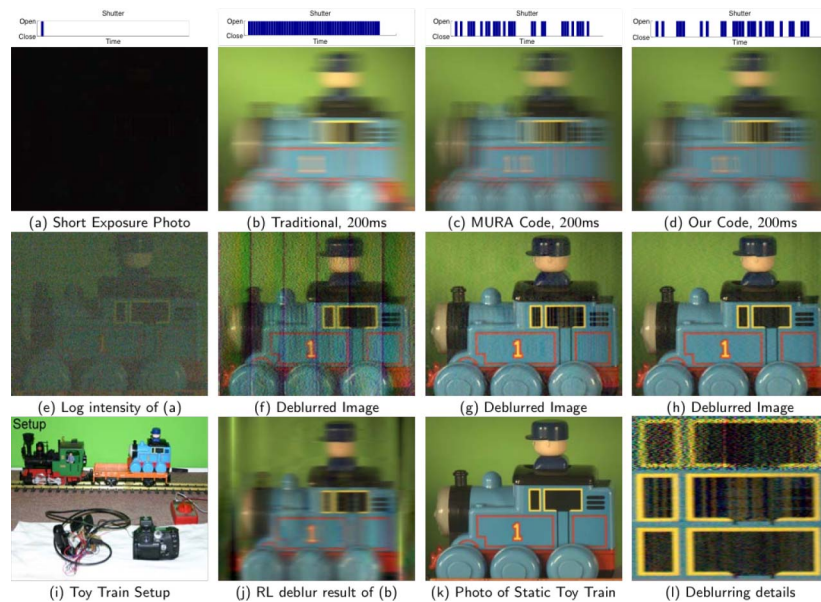
#### Lensless On-Chip Microscopy

In Section 6.2a, we discussed how high numerical apertures in high-resolution optical microscopes limit their SBWP, which limits their FOV. In a laboratory or other controlled environment, scanning can be used to increase FOV. Such an approach is not well suited for use in the field, where immediate diagnoses can be critical and waiting for a scan to complete introduces unacceptable delays.

The constraints on microscope design for field use are high-resolution imaging with a large FOV in a compact package. Given that the focal length of the objective lens is a limiting factor in such a design, one approach is to do away with imaging optics altogether [194,195]. Instead of imaging a sample on a photodetector array, lensless on-chip microscopy places the sample on or in close proximity to the array. One approach to imaging under these conditions is shadow-casting, represented in Fig. 31. If the effects of diffraction can be reduced, e.g., by minimizing the distance between the sample and the detector array, processing to produce an image is unnecessary. In the limit of no diffraction, the resolution is determined by the detector pixel size. However, this approach relies upon proximate imaging, not Computational Imaging.

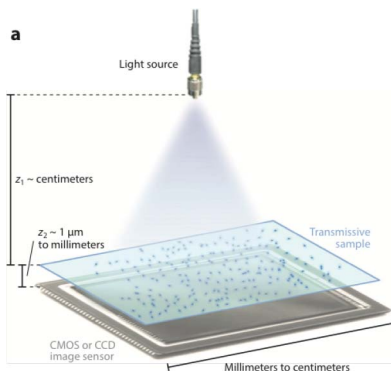
Resolution can also be improved using a microlens array between the sample and the detector array, and stepping the sample along the detector plane. In this mode, the resolution is limited by the microlenses and by the precision with which the sample

Figure 30



Comparison between (a) short and (b) long continuous exposures, (c) an exposure code based on MURA, and (d) a custom code, where the exposure patterns are shown above each image. (d)–(h) Reconstructions using a least-square estimation method. (i) Experimental setup used to acquire the images in (a)–(d). (j) A reconstructed image from the raw image in (b) using the Richardson–Lucy algorithm. (k) A stationary image of the same scene in (a)–(d). A zoomed-in region of (f) on the top, (g) in the middle, and (h) on the bottom. Reprinted with permission from Raskar *et al.*, ACM Trans. Graph. 25, 795–804 [193]. Copyright 2006 Association for Computing Machinery, Inc.

Figure 31



Lensless imaging. A sample placed near the surface of a detector array is illuminated from the opposite side. If the illumination is coherent, digital holography techniques can be used to recover sample amplitude and phase. Reproduced with permission from Ozcan and McLeod, Ann. Rev. Biomed. Eng. 18, 77–102 (2016) [195]. Copyright Annual Reviews, <http://www.annualreviews.org>.

can be scanned. In addition to using scanning, this conventional approach also does not pass the litmus test for Computational Imaging.

Alternatively, resolution can be increased by forming a Gabor hologram. In this case, the sample is illuminated using a monochromatic point source, and the interference between light scattered by the sample  $A_{\text{scat}}(x, y)$  and unscattered light from the reference  $A_{\text{ref}}(x, y)$  is detected [195]. The field in a plane immediately below the sample is

$$E_{\text{sample}}(x, y) = A_{\text{ref}}(x, y) + A_{\text{scat}}(x, y) \exp[j\phi_{\text{scat}}(x, y)], \quad (65)$$

where  $\phi_{\text{scat}}(x, y)$  is the phase delay across the sample. The hologram on the detector array is a convolution of  $E_{\text{sample}}(x, y)$  with a free space propagation kernel  $h(x, y)$ :

$$E_{\text{meas}}(x, y) = |E_{\text{sample}}(x, y) * * h(x, y)|^2. \quad (66)$$

Methods developed in digital holography can be applied to recover phase and amplitude images from  $E_{\text{meas}}(x, y)$  [86]. For example, after separating the encoded content from its conjugate twin and the bias, one can reconstruct the sample using the free-space propagation transfer function to computationally backpropagate the result. In addition to improving the spatial resolution, this method improves signal-to-noise in comparison to the shadow casting.

The value of point-of-care microscopy in medicine has provided a significant impetus for the development of this technology and advanced capabilities of smartphones have accelerated that development. The elimination of a compound optical system in lensless on-chip microscopy results in a system that is potentially more compact and less expensive than a conventional microscope, and highly portable systems based on a cellphone platform have been demonstrated [194]. In addition to those advantages, the FOV for lensless on-chip microscopy can extend over most of the detector array so that the resulting SBWP is substantially improved in comparison to a conventional microscope.

#### *Multi-Aperture Imaging*

Conventional imaging systems typically use a single aperture to collect light and image a scene onto a photodetector array. The performance of these systems is coupled to the imager's geometry. For example, resolution, magnification, and signal-to-noise scale with focal length and aperture size, i.e., increasing the size of the optic improves optical resolution. However, material costs also scale with focal length and aperture size. Thus, increasing the size of the optic also increases the size, weight, and cost of the imager. Using multiple apertures in combination with computation allows one to break this linkage [196–198].

A lens with focal length  $f$  and diameter  $D$  produces an image with an optical resolution in the image plane given approximately by  $\lambda f \#$ . The depth of the imager is proportional to  $f$ . The depth can be reduced by decreasing the focal length and, so long as the lens  $f \#$  is maintained, the image-plane resolution is unchanged. Unfortunately, this reduces resolution in the object plane and FOV, and, if the detector array remains unchanged, detector sampling generates a low-resolution image in comparison to the original image.

To overcome the detector-limited sampling caused by using a smaller lens and gain back resolution, the thin observation module by bound optics (TOMBO) replaces the single lens by an array of lenses [196]. See Fig. 32. Although each microlens forms a low-resolution image on the detector array, each image has a slightly different FOV. This spatial diversity provides the encoding needed to generate a composite image

with a resolution comparable to a single lens over the full aperture and provide performance comparable to a larger, heavier conventional imager. It should be emphasized, however, that TOMBO achieves this performance by reducing the effects of detector-limited sampling, but does not improve on the diffraction-limited resolution.

As mentioned in Section 6, integral imaging [149–151] and light-field cameras [152–156] are also examples of multi-aperture imaging. These imagers share similarities with TOMBO, including a microlens array to multiplex images spatially, but incoherently, on a focal plane. However, they differ in application, which dictates how the incoherent superposition is processed. The objective in TOMBO is to overcome the geometric scaling associated with high-resolution imaging. Multi-apertures introduce a diversity in perspective, which produces sub-pixel offsets between sub-images and allows one to increase resolution. In the light field camera, the diversity in perspective is associated with sampling in  $k$ -space, or angle, which enables digital refocusing.

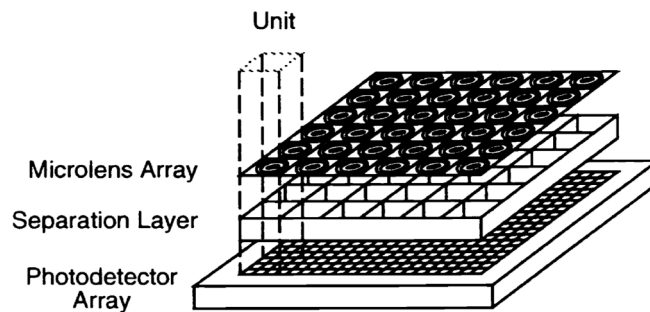
Multi-aperture imaging systems can be divided into two groups: those that use an array of apertures and a single detector array, as just discussed, and those that pair each aperture to a separate detector array. We refer to the latter as a multi-camera system. Multi-camera systems have been demonstrated as another method of acquiring light fields [154], and in a general context referred to as synthetic aperture photography [155] discussed in Section 6. By mapping the individual apertures to other parameters, including transmission coefficients, polarization, and spectrum, multi-camera and multi-aperture designs have also been applied to extended dynamic range imaging, polarimetric imaging, and multispectral imaging [199–201]. A temporal analogue to the spatial method for high dynamic range in a multi-camera system [199] has been implemented in a commercially available compact multi-camera system [198].

Because effective collection area scales linearly with the number of cameras in the array, multi-camera systems have also been used in astronomy as an alternative to large, expensive telescopes [202]. Another multi-camera architecture was developed to address the challenges of off-axis aberrations in acquiring large field, multi-gigapixel images [203]. Like TOMBO, in each of the above examples, the raw data consists of an incoherent superposition of images.

#### 7.2d. Feature-Specific and Compressive Imaging

A variety of applications exist that attempt to extract features important to a specific task, such as classification or identification, using images obtained conventionally.

Figure 32



Schematic of TOMBO. A microlens array is positioned near the surface of a detector array using a separation layer to insure the scene is imaged onto the detector. The separation layer also provides shielding to prevent crosstalk between unit cells. Reprinted with permission from [196]. Copyright 2001 Optical Society of America.

All other information contained in the image is then ignored or discarded. This results in an approach that is inefficient, both in the collection of data and in the collection of photons. The inefficient collection of photons can have a negative impact on SNR. A more efficient approach is one that measures only those features that contribute successfully to performing the task at hand. For example, it is more efficient to measure projections of a scene onto a limited set of basis functions that encompass the set of desired features effectively as opposed to a pixel-based set of measurements.

Optical systems capable of linearly projecting an input image onto specific features were developed contemporaneously with holography and demonstrated as matched filter correlators [204]. Subsequent modifications to coherent optical systems using complex filters in the Fourier plane demonstrated a wider range of linear transforms that can be realized directly in optics [205,206].

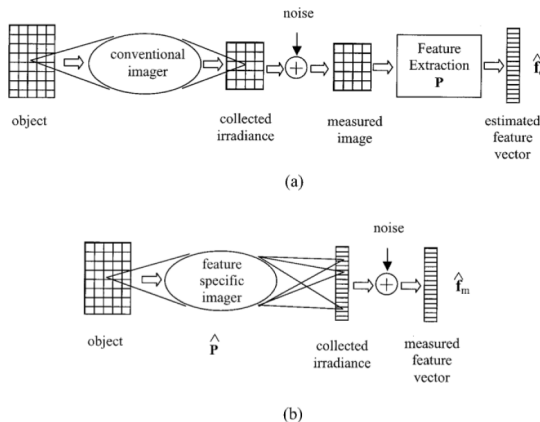
Feature-specific imaging represents a method of projective imaging in which the basis and the number of projections required to perform a specific task is established by the intended application and, more specifically, by the image features most important to the application [207]. Figure 33 compares a conventional imager to a feature-specific imager. Consider the case where both imagers collect the same number of photons,  $N_\nu$ , with fixed detector noise,  $\sigma_n$ , and  $M$  features are required to perform the task. The schematic illustrates how a conventional imager with a square detector array that has  $P^{1/2}$  pixels on a side makes  $P$  measurements regardless of the task and the number of features. The average number of photons per measurement (detector) is  $N_\nu/P$ . The feature-specific imager, instead, makes  $2M \ll P$  measurement, and the number of photons per measurement is  $N_\nu/2M$ . Therefore,

$$\text{SNR}_{\text{CI}} \approx \frac{N_\nu}{P\sigma_n} \ll \frac{N_\nu}{2M\sigma_n} \approx \text{SNR}_{\text{FSI}}, \quad (67)$$

where  $\text{SNR}_{\text{CI}}$  is the signal-to-noise for the conventional imager and  $\text{SNR}_{\text{FSI}}$  is the signal-to-noise for the feature-specific imager.

The potential advantage of feature-specific imaging over conventional imaging has been investigated by simulating the notional systems represented in Fig. 33 applied to facial recognition. Figure 34 compares the mean-squared-error  $\text{MSE}_c$  of the conventional imager to that of the feature-specific imager  $\text{MSE}_M$ , assuming  $M$  of

Figure 33



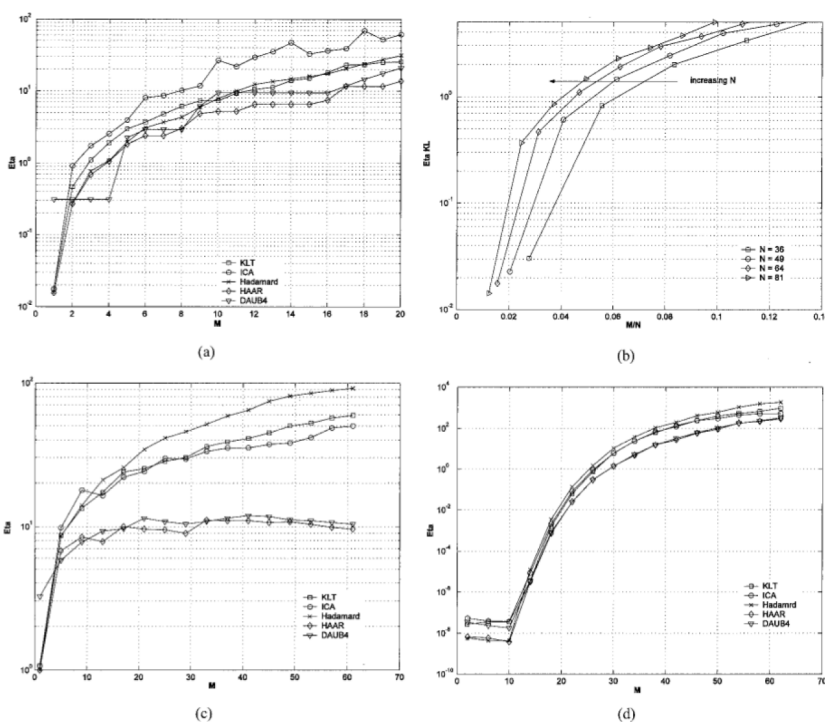
Schematic comparison of (a) a conventional imaging system and (b) a feature-specific imaging system. Reprinted with permission from [207]. Copyright 2003 Optical Society of America.

a possible  $N$  features. These results make the comparison using five different feature types, or projections: Hadamard, Haar wavelets, Daubechies wavelets (DAUB4), Karhunen–Loeve (KLT), and independent component analysis (ICA).

Acquiring a high-resolution, large-field image generally requires the use of a large detector array (i.e., one with a large number of pixels). Although detector arrays with tens of megapixels are quite common and affordable for visible imaging, the development of arrays in other spectral bands, short-wave IR, for example, has not advanced at the same rate. Large arrays for imaging in alternative spectral bands are often prohibitively expensive or simply do not exist. In addition, the data volumes generated by large detector arrays increase demands on data storage, transmission, and processing, which can lead to unacceptably long latencies in system operation. That the data volume scales with the number of pixels for a conventional imaging system is due, in part, to the inefficient spatial sampling strategy of point-to-point imaging.

Compressive imaging, which is a more general method of projective imaging than feature-specific imaging, allows one to reduce the demand for ever-increasing detector array sizes. Compressive imaging acquires and reconstructs images using projections of a scene onto a set of basis functions instead of mapping the scene onto a detector using point-to-point imaging. The minimum number of projection measurements required to reconstruct an image is determined by the sparsity of the scene, i.e., the number of terms necessary to expand the scene in a pre-specified basis, and the scene

**Figure 34**



Relative feature fidelity,  $\eta = \text{MSE}_M / \text{MSE}_c$ , as a function of the number of features. Features simulated include KLT, ICA, Hadamard, Haar wavelets, and DAUB4. The plots in (a) assume additive white Gaussian noise (AWGN) for  $N = 64$ . (b) Simulates results for KL features for  $N = 36, 49, 64$ , and  $81$ . (c), (d) Same results as (a) for shot noise (c) and quantization noise (d). Reprinted with permission from [207]. Copyright 2003 Optical Society of America.

SNR. In addition to finite extent and positivity, the scene sparsity represents additional *a priori* information one can apply as a constraint in post-detection processing.

Compressive imaging is a subset of the broader area known as compressive sensing [208,209]. The following discussion is based on the concise description of compressive sensing presented in Ref. [210]. The method relies on an image  $x$  being sparse in some basis.

Consider a basis described by a set of vectors  $\psi_i$ . Sparsity implies that, when  $x$  is expanded in a finite series of  $N$  basis functions,

$$x = \sum_{i=1}^N \alpha_i \psi_i, \quad (68)$$

only  $K$  values of the coefficients  $\alpha_i$  are nonzero, where  $K \ll N$ . Compression is achieved when one stores only the  $K$  most significant coefficients. However, compression is also possible if one limits the number of measurements to  $M < N$ , where the measurements can be written

$$y = \Phi x = \Phi \Psi \alpha. \quad (69)$$

The term  $\Psi$  in Eq. (69) corresponds to the vectors  $\psi_i$  stacked into a  $1 \times N$  column vector, and  $\Phi$  is a set of measurement vectors  $\phi_m$ , where  $m = 1$  to  $M$  stacked into rows to form a  $M \times N$  matrix. In general, the number of solutions to  $x$  can be infinite, but careful design of  $\Phi$  enables  $x$  to be well-approximated from the measured values. Because  $M < N$  in Eq. (69), reconstruction requires solving an under-determined system of equations. Traditional methods of image reconstruction are, therefore, insufficient to recover  $x$ . As an alternative,  $\ell_1$  optimization can be applied where

$$\hat{\alpha} = \arg \min \|\alpha'\|_1 \quad \text{such that } \Phi \Psi \alpha' = y. \quad (70)$$

The  $\ell_1$  optimization makes it possible to reconstruct  $K$ -sparse vectors with as few as  $M \geq O(K \log(N/K))$  random measurements. In the likely event that the measurement contains noise with an upper magnitude bound of  $\epsilon$  and  $\ell_2$  error  $\sigma_K$  resulting from approximating  $\alpha$  with the  $K$  most significant terms, then the alternative  $\ell_1$  minimization is applied:

$$\hat{\alpha} = \arg \min \|\alpha'\|_1 \quad \text{such that } \|y - \Phi \Psi \alpha'\|_2 < \epsilon. \quad (71)$$

For noise and approximation error amplification constants given by  $C_N$  and  $C_K$ , respectively, Eq. (71) usually yields a solution for which  $\|\hat{\alpha} - \alpha\| < C_N \epsilon + C_K \sigma_K(x)$ .

An example of compressive imaging is the single-pixel camera [210] represented in Fig. 35. The system uses a digital micromirror device (DMD) as a spatial light modulator to encode a two-dimensional  $N^{1/2} \times N^{1/2}$  binary pattern corresponding to  $\phi_m$ . An intermediate image of the scene  $x$  is formed on the DMD and the resulting projection  $\phi_m x$  is spatially integrated by a lens onto a single photodetector to obtain a measurement of  $\alpha_m$ . The process is repeated for an additional  $M - 1 \ll N$  random cases of  $\phi_m$ . The resolution of the reconstructed image is limited by the resolution of the DMD instead of the resolution of the detector.

In most cases, compressive sensing techniques enable a given performance to be achieved with fewer measurements than required with conventional sampling methods. This makes it possible to increase image resolution for a fixed measurement time, reduce acquisition time for a fixed resolution, increase the volume of imaged areas, or perform dynamic imaging. Consequently, the impact of compressed sensing has been

much broader than is reflected by the single example described above. Other examples where compressed sensing has been applied include spectral imaging [134] and super-resolution microscopy [185]. MRI in particular has benefited significantly from the introduction of compressive sensing methods [211].

### 7.3. Adaptive Systems

Implicit in the imagers we have presented to this point is that their optical function is static. Although the instrument may make a multitude of measurements over time to form a single image, the imager's optical function does not change during this period. The development of dynamic optical elements, or spatial light modulators (SLMs), alters this construct. An SLM enables an imager to alter its PSF over time and, when combined with post-detection processing, enables feedback in imaging. Thus, it is possible to alter the measurement made at the present time based on prior measurements.

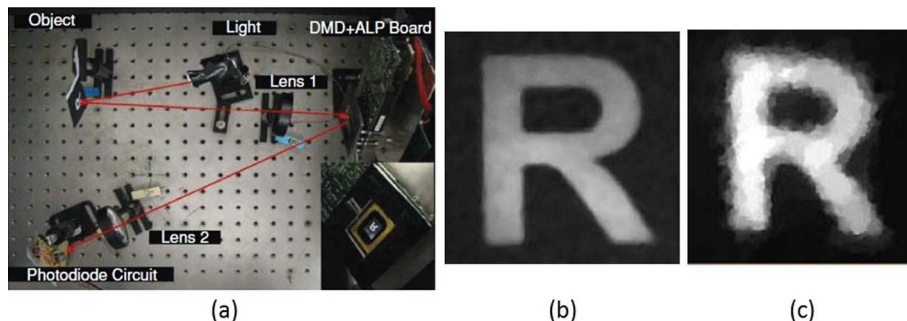
In this section, we present examples of this type of imaging. The goal of feedback in adaptive optics is to form the “best” image possible by canceling aberrations present in the environment. Alternatively, adaption can be based on measures of information content throughout an image. In so doing, it is possible to insure regions that exhibit high measures of information receive proportionally more imaging resources. Similarly, in adaptive lidar, knowledge of the scene based on prior measurements is used to maximize the energy incident on an object of interest.

#### 7.3a. Adaptive Optics

Deviations (e.g., from noise and diffraction) to an optical wavefront as it propagates limit the quality of an image. Some deviations are due to the imaging system, e.g., the optics used to collect the wavefront. Others are due to the environment encountered by a wavefront while propagating to the imaging system. Atmospheric distortion is most significant when a wavefront propagates through the atmosphere, e.g., in a ground-based telescope, or over long horizontal paths in the atmosphere, e.g., in free-space optical communication systems.

Methods to correct wavefront distortions, whose development started in 1953 [212], have resulted in the widespread use of adaptive optics in a variety of applications, including astronomy, free-space optical communications, and microscopy. The essence of the technique is to measure the wavefront, estimate distortions, and modify the optics to remove distortions. Although the goal is to realize a PSF with reduced aberrations,

Figure 35



Single-pixel camera. (a) Experimental setup. The object is imaged by Lens 1 onto the DMD displaying a function  $\phi_m$ . Their product is imaged by Lens 2 onto an integrating photodetector. (b) Conventionally imaged  $256 \times 256$  object. (c) Image reconstructed using 1300 random measurements. © 2008 IEEE. Reprinted with permission from Duarte *et al.*, IEEE Signal Process. Mag. 25(2), 83–91 (2008) [210].

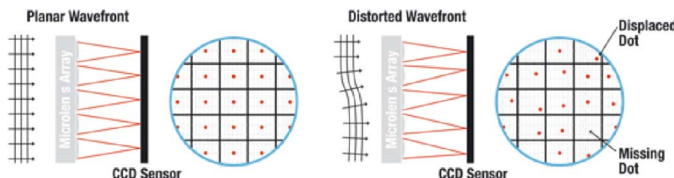
the measurements of distortion and their application to reduce aberrations render the system computational.

To estimate wavefront distortions, one can use a device such as the Shack–Hartmann wavefront sensor represented in Fig. 36. The sensor consists of an array of microlenses, which, when illuminated by an undistorted reference point source (or guide star), produce a regular array of point images. See the figure on the left in Fig. 36. As shown on the right, distortions in the wavefront cause the array of point images to become irregularly spaced. Since the displacement from the optic axis of each microlens is proportional to the tilt in the wavefront over that region, one can use the pattern measured by the sensor to estimate wavefront distortion. A deformable mirror in the optical path of the system uses this estimate to reshape the wavefront and remove the distortions.

This is illustrated in Fig. 37. Since a flat mirror does not alter the inherent properties of an incident wavefront after reflection, an unaberrated wavefront is reflected as an unaberrated wavefront, as shown in Fig. 37(a), and an aberrated wavefront retains its aberrations as represented in Fig. 37(b). In Fig. 37(c), the aberrated wavefront is corrected by the deformable mirror. The bottom row of Fig. 37 illustrates two deformable mirror implementations: a shape-controlled membrane (left image) and independently controlled segments (right image).

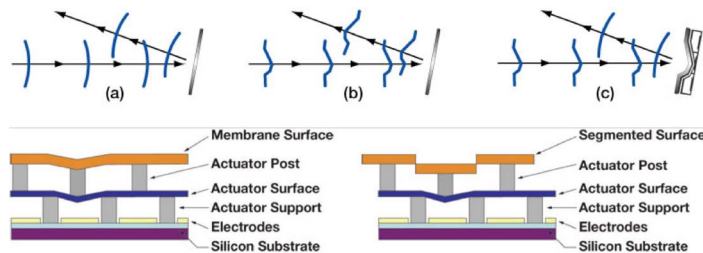
Feedback between the wavefront sensor and the mirror controller help the imager maintain a well-corrected PSF even under dynamic circumstances. Generation of

**Figure 36**



Plane wave incident received by a Shack–Hartmann sensor is shown on the left. In this case, the microlenses form spots on the detector array in a uniform grid. When the wavefront contains aberrations, the spots will be displaced, as illustrated on the right, corresponding to the shape of the wavefront. Reprinted with permission from Thorlabs [213].

**Figure 37**



(a) Unaberrated wavefront remains unaberrated and (b) an aberrated wavefront remains aberrated after reflection from a flat mirror. (c) A deformable mirror is able to correct an aberrated wavefront. The bottom row illustrates two different MEMS-based approaches to implementing a deformable mirror. Reprinted with permission from Thorlabs [213].

the signal that drives the feedback requires an indirect measurement that is made in parallel to the imaging system and, thus, renders the system computational.

### 7.3b. Adaptation-Based on Information

The objective in adaptive optics and the generation of the feedback signal are both grounded in physical notions of imaging. In contrast, other adaptive systems use concepts from information theory as a foundation for adaptation. These systems redistribute imaging resources to insure that measurements are made predominantly in regions that exhibit high information content [214–216].

PANOPTES [215,216], in particular, seeks to extract relevant information from a scene, yet it is capable of adapting to various situations. Since spatial information in a scene is not uniformly distributed, PANOPTES matches imaging resources to the information content of a scene. It uses micromirror technology to realize an adaptable and steerable FOV version of TOMBO. Using an array of subimagers allows the system to be thinner than it might otherwise be.

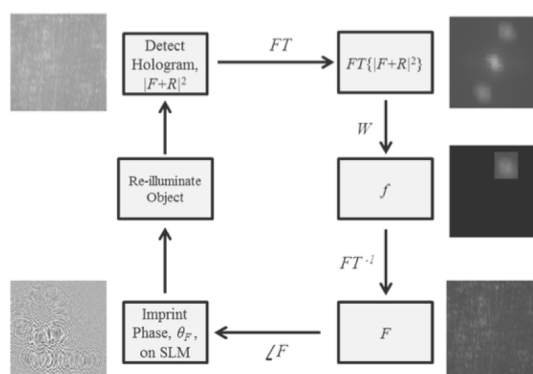
The micromirrors are located within the pupil of the imaging system, which allows them to steer the FOV of the detector array. This enables the FOVs of several subimagers to overlap, which improves angular resolution. The FOVs are steered based on a measurement of the local entropy, measured as the average normalized power spectral density in the region of interest. Regions with high information content are viewed by more subimagers.

### 7.3c. Adaptive Lidar

Conventional imaging systems generally require an unobscured line of sight to the object plane of interest. Therefore, the usefulness of such systems for imaging through obscurations, such as a forest canopy or other foliage, is severely limited. Range-gated laser radar systems have proven to be effective at imaging through such obscurants. However, their performance is limited by the amount of illumination that penetrates the foliage to reach the object plane and returns to the transmitter. Furthermore, strong returns directly from the foliage can overwhelm the actual signal.

A method based on digital holography and optical phase conjugation has been demonstrated that addresses these challenges by removing the illumination from the foliage in the foreground and concentrating it on the object plane [217–220]. The approach is represented in Fig. 38. A Fourier hologram of an object  $f(x, y)$  is recorded using a coherent reference source  $r(x, y)$ , i.e., the hologram records the interference

**Figure 38**



Adaptive lidar system. Reprinted with permission by Watnik and Lebow, Proc. SPIE 8843, 88430E (2013) [217]. Copyright 2013.

between the transforms  $F(u, v)$  and  $R(u, v)$ . The phase of the reference  $R(u, v)$  is set using an SLM. The initial reference phase is random.

As shown in the upper right of Fig. 38, the digital inverse transform of the hologram produces the three terms identified in Eq. (36): an off-axis real image, its conjugate, and an on-axis bias term. The image  $f(x, y)$  is extracted and forward transformed to yield an estimate of  $F(u, v)$ . When the phase of  $F(u, v)$  is displayed on the SLM, the reference is now phase-conjugate to the object. Applying this process iteratively increases the light energy that illuminates the object and increases SNR.

One should note the similarities between Figs. 8 and 38. For phase retrieval, constraints in the image and Fourier domains were applied iteratively but off-line to generate a Fourier magnitude and phase that was consistent with physics and measurements. In adaptive lidar, the iterative constraints are applied in real-time to produce a structured illumination pattern. That pattern accounts for obstructions in the line of sight between target plane and imager and, thereby, increases the irradiating illumination on those elements of the target plane that are visible from the imager.

## 8. FUTURE OF COMPUTATIONAL IMAGING

As dictated by the nature of a review article, all the material we have presented to this point has looked back. We began with a definition of imaging and a history of imaging that highlighted the state of optical design up to the introduction of electronic detection and post-detection processing. We then identified the distinguishing features of Computational Imaging and presented numerous examples of computational imagers.

As we close, we turn our attention forward. In this section, we assess the future of Computational Imaging by considering its strengths, weaknesses, opportunities, and threats. This approach, typically used by organizations like the ones we work for, is useful to develop bold strategic visions that are, nonetheless, grounded in science and technology.

### 8.1. Strengths

Computational Imaging's greatest strength is that it represents a new paradigm in optical design, a centuries-old discipline. The features of this paradigm include altering the nature of the optical measurement to achieve a desired result (the most appropriate measurement may not result from a traditional point-to-point mapping of a scene) and balancing image formation and information extraction between the physical and computational domains. Applying concepts from information theory allows optical designers to exploit fully the processing potential embedded in physical optics.

The revolutionary nature of this new paradigm is apparent when one observes that the performance and capabilities of optical elements are governed by, and hence constrained by, physical laws, such as Maxwell's Equations. In contrast, computational power has grown exponentially for the past half-century according to Moore's Law. Consequently, Computational Imaging enables capabilities that *cannot* be realized using conventional techniques.

### 8.2. Weaknesses

For imagers designed with an eye toward Motivation 3, the advantage argument, one must weigh the costs associated with computational and conventional approaches to imaging against a projected improvement in utility. Costs considered include, for example, those associated with the physical instantiation used to make nontraditional measurements, the data volume generated by measurements, and the impact of physical models and calibration on processing load. Because assessing such costs is not presently an exact science, we highlight some of the uncertainties in the process.

A fundamental principle of Computational Imaging is balancing the power of physics to transform fields with that of digital computation to process measurements. This dictum keeps one from replacing mass-produced lenses with expensive specialized optics or, at the other extreme, simplifying the optics to a point where the computational load increases to unacceptable levels. The former point is a caution about the promise and potential of optical technologies, such as gradient-index optics and free-form surfaces, to improve optical performance. If “simpler” optics requires specialized fabrication, the optics are not simple. The latter point indicates there exists a trade-off between glass and electrical power. Given the processing capacity of a lens, there need to be compelling technical reasons to replace it with a less capable element like a random phase mask.

Unfortunately, the ease with which one can develop a processing algorithm can obscure issues related to the implementation of a Computational Imager in the real world. Computational Imaging requires that one embed a model of the optical system within the computation. If that model does not realistically reflect the complexity of the optical system, the advantages of Computational Imaging may be lost. This could be the case if, for example, the model simplifies the optics to a few objective parameters that ignore the wave nature of light, aberrations, or system sensitivity to temperature variations. Designers are faced with the conundrum that simplistic models may not generate useful results, and realistic models may require high processing loads and long processing times. Practical considerations include the condition of the forward model and the ease with which it can be inverted, the sensitivity of the measurement code to noise, and the level of artifacts introduced by post-processing.

Integral to the optical system models used in computation is the robustness of the computation [221], in particular, robustness to variations in performance of a single system over time and to variations between multiple systems in an ensemble. Calibration is therefore essential to Computational Imaging. Initial calibration and periodic updates are costs that designers ignore at their own peril.

A key distinguishing feature of Computational Imaging, the joint design of optics and computation, runs counter to modular open system design, a powerful trend in modern technology. Modular designs with standardized interfaces allow one, for example, to use a Nikon lens with a Panasonic focal plane or to port a high dynamic range imaging app across a wide range of hardware platforms. Such modularity and standardization in interfaces is what has led to mass manufacturing, affordability, and the spread of sophisticated consumer devices. Computational Imaging systems must provide an overwhelming advantage in performance, utility, or human interface to overcome this dominant paradigm of modular design.

Additionally, for commercial systems, one needs to assess the organizational costs associated with delivering a computational imager [222]. The development of such a system requires a multidisciplinary team and, presently, rare is the individual who is proficient in both optical physics and information processing. The attraction of an individual to one discipline as opposed to another is reflected in the stovepiped organizational structure of some companies. Unfortunately, stovepipes that are simple to manage can hinder cross-disciplinary engagement. Thus, any performance advantage claimed by Computational Imaging must be sufficiently large to convince management to cross organizational bounds. This is especially true for manufacturers of expensive instruments with an established and broad consumer base, such as MRI and CT. To warrant an instrument redesign, the advantages of Computational Imaging must be significant.

Even the nature of the claimed advantage is not well defined. Is it sufficient to compare technical performance or is it more important to consider an advantage in terms of

use? For scientific applications, the former is paramount. But, for commercial systems, the latter is key. A commercial system must provide a market advantage, not just a technical one, for example, reduce the exposure to radiation in medical imaging or reduce waiting times at security checkpoints [222]. In short, the weaknesses of Computational Imaging are inherent when one considers translating an abstract paradigm into practice.

### 8.3. Opportunities

We noted under Strengths that Moore's Law can be used to overcome limitations from Maxwell's Equations. (This was, in fact, an early theme in Computational Imaging.) However, interest in using Computational Imaging for capabilities that *can* be realized conventionally is increasing. To assess the potential for computational techniques to impact future imaging systems, we consider three broad application areas: scientific and medical; commercial and industrial; and safety, security, and defense.

We note that observing with curiosity is the beginning of science. The first optical instruments, telescopes and microscopes, led to advances in astronomy, medicine, and biology, and today's optical instruments continue to push the boundaries of science. Gravity waves were detected using a laser interferometer. Further, the computer, with its ability to enhance the detection and understanding of patterns in observations, and to aid in making predictions, has been critical as an instrument in advancing science [223]. It stands to reason that the marriage of imaging and computation was a major step in the development of scientific instruments. In fact, scientific applications can best justify the large data processing loads and long data processing times required by Computational Imaging.

This has been recognized in microscopy and, as evidenced by the literature, in x-ray science [95,224,225]. Scientific applications such as these take full advantage of the enhanced capabilities enabled by active imaging. Although, by its nature, astronomy remains a passive imaging application, future discoveries can be enabled by adaptive optics and multi-dimensional imaging, especially spatial-spectral.

Commercial and industrial applications, in which the goal is to monitor human behavior or enterprise operations, have the advantage that the environment is cooperative, if not completely under user control. This enables information extraction through active imaging techniques. Virtual and augmented reality systems, in particular, are seen as potentially profitable markets in which Computational Imaging can play a role. These systems still need to overcome the psychophysical effects of representing a three-dimensional environment on a two-dimensional display.

For safety, security, and defense, designers must assume the environment and other conditions are non-cooperative. Imagers must be non-intrusive and they, therefore, remain primarily passive. For surveillance, reconnaissance, and situational awareness, spatial-spectral imagers (which measure detailed spectral signatures at spatial locations) and multi-band imagers (which make image measurements across disparate and non-contiguous spectral bands, e.g., the visible, short-wave, and long-wave IR bands) can significantly increase capabilities.

For spectral bands other than visible, such as the x-ray, ultraviolet, near-IR, IR, terahertz (THz), and gigahertz (GHz) regimes [226–228], there exist considerable opportunities for Computational Imaging. In these bands, phenomenology plays a key role in the development of materials and technology. In particular, x-ray, GHz, and THz bands lack integrated detectors and require expensive optics. The lack of a broad industrial infrastructure in these bands suggests considerable opportunity. So long as making measurements in these regimes remains expensive, Computational Imaging will have a role to play.

Computational Imaging offers potential opportunities at both ends of the complexity-volume scale. For high-complexity–low-volume applications, such as molecular imaging or space-based telescopes, performance is the most critical parameter. For these applications, the stakes are sufficiently high to justify a significant investment of resources, including human expertise, organizational complexity, optical fabrication, computation, and power.

At the other end of the scale, high-volume integrated systems, such as cellphone cameras, offer opportunities in special purpose systems. Such systems can be customized to use resources efficiently while meeting the demands of a narrow range of tasks. The imager for three-dimensional facial capture on the iPhone X, for example, is just such a system. It includes sophisticated illumination, image capture, and post-processing in a very small package. The intimate integration of sensing, processing, storage, display, and communication that exists in present smartphones represents fertile ground for innovation in Computational Imaging.

Three general imaging capabilities that have broad application are three-dimensional imaging, imaging through scattering media, and adaptive imaging. Three-dimensional imaging plays an important role in medicine, security, and human–computer interface. With the invention of touch-sensitive screens and swipe-gesture-based control of displays, human–computer interfaces have gone through a revolution. The next advance, touch-free interfaces, intrinsically requires imaging to sense the position and pose of a human body or body part to remotely control a computer or display.

This capability is particularly critical to home gaming. Consider the experience of a Kinect-enabled X-box game as compared to other games. In this application, Computational Imaging offers a unique approach to privacy concerns. In a touch-free interface based on conventional imaging techniques, the high-resolution video of a user captured for the purposes of controlling a computer also captures the user’s surroundings. To keep this information from being used for other than its intended purposes, extra technology or legal protections need to be developed. In contrast, a Computational Imager can make non-pixel-based measurements to extract only information necessary for the interface to function and, thereby, preserve privacy in a fundamental way.

Imaging through scattering media, such as biological tissue, rain, ice, fog, and even optical fiber, also has broad application. Such situations are encountered in transportation (air, ground, and sea), environmental monitoring, and medicine. In such environments, where the visibility of an object is significantly reduced in comparison to scattered light, physics imposes harsh constraints. To enhance visibility, it is difficult to conceive of techniques that do not rely heavily on computation. This is also true for non-line-of-sight imaging off diffusely scattering surfaces.

A final capability that has broad application is adaptive imaging, i.e., an imager whose next measurement is determined based on prior measurements. An imager that adapts to scene content requires developments in adaptive optics, such as wavefront modulators, and in incorporating feedback from processed data [215–220] as well as the exploitation layer. Sources in the exploitation layer include both experts interfaced via wearable technology and “the wisdom of the crowds” processed via big data techniques that reside in the cloud [229].

Whereas these capabilities enable the space of imaging applications to expand, it is an unavoidable truth that the performance of all imagers is limited by the physics of reflection, refraction, and diffraction. Thus, interest in techniques to improve resolution and increase FOV will always exist. In light of this, the development of new analysis tools, such as phase-space optics [230], takes on increased importance.

Further, although we have argued that computation offers avenues for significant improvement in imaging, some researchers have taken a more fundamental approach by re-examining the law of refraction [231,232]. This re-examination is driven in large part by advances in fabrication techniques that allow one to structure optical elements at the scale of nanometers. Consequently, it is possible to use structured surfaces to reshape wavefronts in ways that are more extreme than a conventional application of Snell's Law might predict [233–235]. Although the input angles and the wavelength of operation over which the devices work are limited, this materials approach to overcoming physical limits provides an avenue to advance imaging that is an adjunct to computational methods.

#### 8.4. Threats

Given that applications within Motivation 3 are technology based, the mass availability of imaging technology represents the greatest threat to Computational Imaging, especially in the visible regime. Visible cameras are today a technology commodity. This is due to optics, detector arrays, and processing chips that are mass reproducible, and to the fabrication technology that allows them to be integrated into wafer-scale cameras. Further, the broad availability of smartphone platforms reduces entry costs for application developers.

That smartphones with integrated imagers appear in both Opportunities and Threats is indicative of the tension between Computational Imaging's joint design and optimization philosophy and the philosophy of modular design and standardized interfaces that underlies commodity electronics. This tension can be released by referring to the motivations for Computational Imaging outlined in this review. If functionality, including intangible factors such as privacy concerns, cannot be achieved through conventional means, an integrated smartphone platform can enable Computational Imaging solutions. If, however, functionality can be achieved using conventional means, the same integrated platform raises substantially the barrier to a Computational Imaging approach.

Consequently, the advantage threshold for Computational Imaging is high. For visible imaging, especially, the high advantage threshold represents a glass ceiling that Computational Imaging must break through. (Pun intended.)

In the future, we expect imaging technology will be embedded in every new appliance (refrigerator, garbage pail, or vacuum), conveyance (automobile, plane, or boat), building (private and commercial), and processing platform. In fact, arrays of cameras will soon be available on our cellphones. It is likely that the emphasis in the future will shift from modifying what a camera does to simply combining images for information extraction. When presented with such a prognosis, the role of the optical physicist is to determine how one computationally combines images in a coherent manner to increase the potential for information extraction.

### 9. CONCLUSION AND SUMMARY REMARKS

For centuries, optical design was dominated by principles developed to augment and enhance human vision. We are now in an era where optical design is dominated by enabling computers to see. Consequently, all imagers produced today include computation. As evidence of this, consider that few cameras sold today have a viewfinder through which a photographer can access an optical image prior to recording it.

However, computation in imaging is not the same as Computational Imaging. The essence of Computational Imaging is not making a direct optical measurement of the parameter one ultimately wants. Instead, one makes an optical measurement, or multiple measurements, from which the desired information is derived.

We identified three motivations for using Computational Imaging: when a direct measurement of the desired parameter is physically impossible, when the dimensionality of the desired parameter is incompatible with present technology, and when making an indirect measurement is more advantageous than making a direct one.

In our objective assessment in Section 8 we avoided using the word success. To conclude our review, we allow ourselves a personal assessment of Computational Imaging's successes. By success, we mean the influence the topic has had over the past three decades on the development of imaging systems. We cannot take credit for the development of stellar interferometry, holography, SAR, coded-aperture imaging, CT, and MRI.

At an intellectual level, Computational Imaging, and its notion of indirect versus direct measurements, has been accepted, as evidenced by texts from Brady [236] and Khare [237]. The IEEE even launched a journal, *IEEE Transactions on Computational Imaging*, in 2015 dedicated to the topic [238].

The scientific impact of Computational Imaging is evident by recent advances in microscopy. Lensless microscopy and ptychographic microscopy have the potential to impact significantly biomedical applications. The ability of superresolved fluorescence microscopy to image single molecules garnered the 2014 Nobel Prize for Chemistry for its inventors, Betzig, Hell, and Moerner.

However, a commercial success for Computational Imaging has been elusive. The cubic phase approach to extended DOF was marketed by CDM Optics, a company founded by Tom Cathey and his doctoral student, Ed Dowski in the late 1990s. Omnivision purchased CDM in 2005 with the intent to include it in a cellphone camera and, thereby, remove the need to focus. The venture was ultimately unsuccessful due to competing technologies that offered the same capability more cheaply. This should not be surprising since, as we noted, imagers driven by Motivations 2 and 3 are dependent upon technology. Further, as we alluded to under Threats in Section 8, the three-dimensional imaging capabilities of the Microsoft Kinect and Apple iPhone X can either be a boon or a bust for Computational Imaging.

When compared to the near-immediate impact Abbe's physical analysis had on Zeiss' commercial success, Computational Imaging is left wanting. Yet, such success can be achieved if the community finds ways to exploit materials, measurement, and computation to overcome some of the fundamental physical limits identified by Abbe.

## ACKNOWLEDGMENT

We acknowledge the US Army Research Laboratory (ARL, Adelphi, Maryland) and the Leibniz Institute for Photonic Technologies (IPHT, Jena, Germany) for, respectively, granting and supporting a nine-month sabbatical to one of us (JNM) to prepare this review. Special thanks go to former ARL Director Dr. Tom Russell, present ARL Director Dr. Phil Perconti, and Prof. Dr. Hartmut Bartelt, IPHT, for their support. It was inspiring to consider the future of imaging while sitting, literally, in the shadow of Zeiss, Abbe, and Schott.

We also acknowledge the thorough and careful reading of our manuscript by the reviewers. Their comments were detailed, constructive, and complete, and truly helped us improve the presentation of our manuscript. Finally, the affiliation of one of us (GWE) with the MITRE Corporation is provided for identification purposes only, and is not intended to convey or imply MITRE's concurrence with, or support for, the positions, opinions or viewpoints expressed by the author. Approved by MITRE for Public Release; Distribution Unlimited. Case Number 18-0107.

## REFERENCES

1. J. N. Mait, "A history of imaging: revisiting the past to chart the future," *Opt. Photon. News* **17**(2), 22–27 (2006).
2. H. H. Barrett and K. J. Myers, *Foundations of Image Science* (Wiley, 2003).
3. R. Raskar, "Computational photography," in *Frontiers in Optics 2009/Laser Science XXV/Fall 2009 OSA Optics & Photonics*, Technical Digest (2009), paper CTuA1.
4. C. Zhou and S. Nayar, "Computational cameras: convergence of optics and processing," *IEEE Trans. Image Process.* **20**, 3322–3340 (2011).
5. J. Schwartzman, "Advanced imaging used in cinematography," [https://www.osa.org/en-us/media\\_library/plenary\\_keynote\\_sessions/](https://www.osa.org/en-us/media_library/plenary_keynote_sessions/).
6. E. Abbe, "Beiträge zur theorie des mikroskops und der mikroskopischen wahrnehmung," *Archiv für mikroskopische Anatomie* **9**, 413–418 (1873).
7. C. E. Shannon, "A mathematical theory of communication," *Bell Syst. Tech. J.* **27**, 379–423 (1948).
8. G. T. di Francia, "Resolving power and information," *J. Opt. Soc. Am.* **45**, 497–501 (1955).
9. E. H. Linfoot, "On resolving power and information," *J. Opt. Soc. Am.* **46**, 72 (1956).
10. G. T. di Francia, "On resolving power and information," *J. Opt. Soc. Am.* **46**, 72 (1956).
11. D. Gabor, "Light and information," *Prog. Opt.* **1**, 109–153 (1961).
12. G. T. di Francia, "Degrees of freedom of an image," *J. Opt. Soc. Am.* **59**, 799–804 (1969).
13. P.-M. Duffieux, *L'intégrale de fourier et ses applications à l'optique* (1946). Privately published by Oberthur in Rennes.
14. J. W. Goodman, *Introduction to Fourier Optics*, 3rd ed. (Roberts, 2005).
15. L. J. Cutrona, E. N. Leith, C. J. Palermo, and L. J. Porcello, "Optical data processing and filtering systems," *IRE Trans. Inf. Theory* **6**, 386–400 (1960).
16. E. N. Leith and J. Upatnieks, "Reconstructed wavefronts and communication theory," *J. Opt. Soc. Am.* **52**, 1123–1130 (1962).
17. E. N. Leith and J. Upatnieks, "Wavefront reconstruction with diffused illumination and three-dimensional objects," *J. Opt. Soc. Am.* **54**, 1295–1301 (1964).
18. W. S. Boyle and G. E. Smith, "Information storage devices," U.S. patent 3,858,232 (December 31, 1974).
19. M. F. Tompsett, "Charge transfer imaging devices," U.S. patent 4,085,456 (April 19, 1978).
20. J. W. Cooley and J. W. Tukey, "An algorithm for the machine calculation of complex Fourier series," *Math. Comput.* **19**, 297–301 (1965).
21. Intel, "The story of the Intel 4004—Intel's first microprocessor: its invention, introduction, and lasting influence," <https://www.intel.com/content/www/us/en/history/museum-story-of-intel-4004.html>.
22. R. A. Athale, G. W. Euliss, and J. N. Mait, "Computation imaging: old wine in new bottles?" in *Frontiers in Optics* (Optical Society of America, 2006), paper FWH2.
23. W. T. Cathey, B. R. Frieden, W. T. Rhodes, and C. K. Rushforth, "Image gathering and processing for enhanced resolution," *J. Opt. Soc. Am. A* **1**, 241–250 (1984).
24. R. M. Matic and J. W. Goodman, "Optimal pupil screen design for the estimation of partially coherent images," *J. Opt. Soc. Am. A* **4**, 2213–2227 (1987).
25. R. M. Matic and J. W. Goodman, "Comparison of optical predetection processing and postdetection linear processing for partially coherent image estimation," *J. Opt. Soc. Am. A* **6**, 213–228 (1989).

26. R. M. Matic and J. W. Goodman, "Optical preprocessing for increased system throughput," *J. Opt. Soc. Am. A* **6**, 428–440 (1989).
27. W. Veldkamp, "Wireless focal planes 'on the road to amacronic sensors,'" *IEEE J. Quantum Electron.* **29**, 801–813 (1993).
28. E. R. Dowski and W. T. Cathey, "Extended depth of field through wave-front coding," *Appl. Opt.* **34**, 1859–1866 (1995).
29. J. van der Gracht, E. R. Dowski, W. T. Cathey, and J. P. Bowen, "Aspheric optical elements for extended depth-of-field imaging," *Proc. SPIE* **2537**, 279–288 (1995).
30. J. van der Gracht, E. R. Dowski, M. G. Taylor, and D. M. Deaver, "Broadband behavior of an optical-digital focus-invariant system," *Opt. Lett.* **21**, 919–921 (1996).
31. M. Descour and E. Dereniak, "Computed-tomography imaging spectrometer: experimental calibration and reconstruction results," *Appl. Opt.* **34**, 4817–4826 (1995).
32. M. A. Neifeld, "Information, resolution, and space-bandwidth product," *Opt. Lett.* **23**, 1477–1479 (1998).
33. D. L. Marks, R. A. Stack, and D. J. Brady, "Three-dimensional coherence imaging in the Fresnel domain," *Appl. Opt.* **38**, 1332–1342 (1999).
34. F. O. Huck, C. L. Fales, and Z.-U. Rahman, "An information theory of visual communication," *Philos. Trans. R. Soc. London A* **354**, 2193–2248 (1996).
35. J. N. Mait, *U.S. Army Workshop on Integrated Imaging*, Research Triangle Park, December 17, 1999.
36. OSA Topical Meeting on Integrated Image Gathering and Processing, Albuquerque, New Mexico, Optical Society of America, 2001.
37. J. N. Mait, R. Athale, and J. van der Gracht, "Evolutionary paths in imaging and recent trends," *Opt. Express* **11**, 2093–2101 (2003).
38. J. R. Fienup, "Reconstruction of an object from the modulus of its Fourier transform," *Opt. Lett.* **3**, 27–29 (1978).
39. J. R. Fienup, "Iterative method applied to image reconstruction and to computer-generated holograms," *Opt. Eng.* **19**, 297–305 (1980).
40. J. R. Fienup, "Phase retrieval algorithms: a comparison," *Appl. Opt.* **21**, 2758–2769 (1982).
41. E. J. Candes and M. B. Wakin, "An introduction to compressive sampling," *IEEE Signal Process. Mag.* **25**(2), 21–30 (2008).
42. E. Wolf, *Introduction to the Theory of Coherence and Polarization of Light* (Cambridge University, 2007).
43. W. Martienssen and E. Spiller, "Coherence and fluctuations in light beams," *Am. J. Phys.* **32**, 919–926 (1964).
44. H. Bartelt, S. K. Case, and R. Hauck, "Incoherent-optical processing," in *Applications of Optical Fourier Transforms*, H. Stark, ed. (Academic, 1982), pp. 499–536.
45. A. W. Lohmann and W. T. Rhodes, "Two-pupil synthesis of optical transfer functions," *Appl. Opt.* **17**, 1141–1151 (1978).
46. J. R. Fienup, "Phase retrieval for the Hubble Space Telescope using iterative propagation algorithms," *Proc. SPIE* **1567**, 327–332 (1991).
47. H. Andrews and B. Hunt, *Digital Image Restoration* (Prentice-Hall, 1977).
48. W. H. Richardson, "Bayesian-based iterative method of image restoration," *J. Opt. Soc. Am.* **62**, 55–59 (1972).
49. E. Y. Lam and J. W. Goodman, "Iterative statistical approach to blind image deconvolution," *J. Opt. Soc. Am. A* **17**, 1177–1184 (2000).
50. G. A. Farulla, M. Indaco, D. Rolfo, L. O. Russo, and P. Trotta, "Evaluation of image deblurring algorithms for real-time applications," in *9th IEEE*

- International Conference on Design and Technology of Integrated Systems in Nanoscale Era* (2014).
51. J. Rosen and D. Abookasis, "Seeing through biological tissues using the fly eye principle," *Opt. Express* **11**, 3605–3611 (2003).
  52. D. Loterie, S. Farahi, I. Papadopoulos, A. Goy, D. Psaltis, and C. Moser, "Digital confocal microscopy through a multimode fiber," *Opt. Express* **23**, 23845–23858 (2015).
  53. G. Kim, K. Isaacson, R. Palmer, and R. Menon, "Lensless photography with only an image sensor," *Appl. Opt.* **56**, 6450–6456 (2017).
  54. G. Kuo, N. Antipa, R. Ng, and L. Waller, "Diffusercam: diffuser-based lensless cameras," in *Imaging and Applied Optics (3D, AIO, COSI, IS, MATH, pcAOP)* (Optical Society of America, 2017), paper CTu3B.2.
  55. H. B. Wach, E. R. Dowski, and W. T. Cathey, "Control of chromatic focal shift through wave-front coding," *Appl. Opt.* **37**, 5359–5367 (1998).
  56. K. S. Kubala, E. R. Dowski, and W. T. Cathey, "Reducing complexity in computational imaging systems," *Opt. Express* **11**, 2102–2108 (2003).
  57. E. R. Dowski and K. S. Kubala, "Design and optimization of computational imaging systems," *Proc. SPIE* **5299**, 155–162 (2004).
  58. K. S. Kubala, E. R. Dowski, J. Kobus, and R. Brown, "Design and optimization of aberration and error invariant space telescope systems," *Proc. SPIE* **5524**, 54–65 (2004).
  59. D. G. Stork and M. D. Robinson, "Theoretical foundations for joint digital-optical analysis of electro-optical imaging systems," *Appl. Opt.* **47**, B64–B75 (2008).
  60. M. D. Robinson and D. G. Stork, "Joint digital-optical design of superresolution multiframe imaging systems," *Appl. Opt.* **47**, B11–B20 (2008).
  61. J. N. Mait, R. D. Martin, C. A. Schuetz, and D. W. Prather, "Millimeter wave imaging with engineered point spread functions," *Opt. Eng.* **51**, 091606 (2012).
  62. O. S. Cossairt, D. Miau, and S. K. Nayar, "Scaling law for computational imaging using spherical optics," *J. Opt. Soc. Am. A* **28**, 2540–2553 (2011).
  63. O. S. Cossairt, M. Gupta, and S. K. Nayar, "When does computational imaging improve performance?" *IEEE Trans. Image Process.* **22**, 447–458 (2013).
  64. M. Gupta, O. S. Cossairt, and A. Veeraraghavan, "A framework for analysis of computational imaging systems: role of signal prior, sensor noise and multiplexing," *IEEE Trans. Pattern Anal. Mach. Intell.* **36**, 1909–1921 (2014).
  65. Lord Rayleigh, "XXXI. Investigations in optics, with special reference to the spectroscope," *London Edinb. Dublin Philos. Mag. J. Sci.* **8**, 261–274 (1879).
  66. Lord Rayleigh, "XV. On the theory of optical images, with special reference to the microscope," *London Edinb. Dublin Philos. Mag. J. Sci.* **42**, 167–195 (1896).
  67. A. W. Lohmann, "The space-bandwidth product, applied to spatial filtering and holography," Research Paper RJ-438 (IBM San Jose Research Laboratory, 1967).
  68. A. W. Lohmann, R. G. Dorsch, D. Mendlovic, C. Ferreira, and Z. Zalevsky, "Space-bandwidth product of optical signals and systems," *J. Opt. Soc. Am. A* **13**, 470–473 (1996).
  69. S. K. Park and R. Hazra, "Aliasing as noise: a quantitative and qualitative assessment," *Proc. SPIE* **1961**, 2–13 (1993).
  70. D. E. Marshall, Jr., "Focal plane array design for optimum system performance," *Infrared Imaging Syst. Technol.* **226**, 66–73 (1980).
  71. P. Fellgett and E. Linfoot, "On the assessment of optical images," *Philos. Trans. R. Soc. London A* **247**, 369–407 (1955).
  72. B. R. Frieden, "Information, and the restorability of images," *J. Opt. Soc. Am.* **60**, 575–576 (1970).

73. C. L. Fales, F. O. Huck, and R. W. Samms, "Imaging system design for improved information capacity," *Appl. Opt.* **23**, 872–888 (1984).
74. F. O. Huck, N. Halyo, K. Stacy, R. W. Samms, and C. L. Fales, "Image gathering and processing: information and fidelity," *J. Opt. Soc. Am. A* **2**, 1644–1666 (1985).
75. F. O. Huck, J. A. McCormick, S. K. Park, and C. L. Fales, "Image-gathering system design for information and fidelity," *J. Opt. Soc. Am. A* **5**, 285–299 (1988).
76. W.-C. Chou, M. A. Neifeld, and R. Xuan, "Information-based optical design for binary-valued imagery," *Appl. Opt.* **39**, 1731–1742 (2000).
77. G. W. Euliss and J. van der Gracht, "Information-theoretic analyses of a birefringent blur filter," *Appl. Opt.* **40**, 6492–6504 (2001).
78. J. N. Mait, J. van der Gracht, and G. W. Euliss, "Design of a diffractive anti-aliasing filter using information density," *Proc. SPIE* **4736**, 107–115 (2002).
79. B. R. Frieden, *Science from Fisher Information: a Unification* (Cambridge University, 2004).
80. H. H. Barrett, J. Denny, R. F. Wagner, and K. J. Myers, "Objective assessment of image quality. II. Fisher information, Fourier crosstalk, and figures of merit for task performance," *J. Opt. Soc. Am. A* **12**, 834–852 (1995).
81. A. A. Michelson, "Visibility of interference-fringes in the focus of a telescope," *London Edinb. Dublin Philos. Mag. J. Sci.* **31**(190), 256–259 (1891).
82. F. Zernike, "Das phasenkontrastverfahren bei der mikroskopischen beobachtung," *Phys. Zeitschr.* **36**, 848–851 (1935).
83. M. W. Davidson, "Frits Zernike," <https://micro.magnet.fsu.edu/optics/timeline/people/zernike.html>.
84. D. Gabor, "A new microscopic principle," *Nature* **161**, 777–778 (1948).
85. B. R. Brown and A. W. Lohmann, "Complex spatial filtering with binary masks," *Appl. Opt.* **5**, 967–969 (1966).
86. J. W. Goodman and R. W. Lawrence, "Digital image formation from electronically detected holograms," *Appl. Phys. Lett.* **11**, 77–79 (1967).
87. M. A. Kronrod, N. S. Merzlyakov, and L. P. Yaroslavski, "Reconstruction of holograms with a computer," *Sov. Phys. Tech. Phys.* **17**, 333–334 (1972).
88. S. Nakadate, T. Yatagai, and H. Saito, "Electronic speckle pattern interferometry using digital image processing techniques," *Appl. Opt.* **19**, 1879–1883 (1980).
89. L. Onural and P. D. Scott, "Digital decoding of in-line holograms," *Opt. Eng.* **26**, 1124–1132 (1987).
90. U. Schnars and W. Jüptner, "Direct recording of holograms by a CCD target and numerical reconstruction," *Appl. Opt.* **33**, 179–181 (1994).
91. J. R. Fienup, "Reconstruction of a complex-valued object from the modulus of its Fourier transform using a support constraint," *J. Opt. Soc. Am. A* **4**, 118–123 (1987).
92. J. R. Fienup, "Lensless coherent imaging by phase retrieval with an illumination pattern constraint," *Opt. Express* **14**, 498–508 (2006).
93. J. R. Fienup, "Phase retrieval algorithms: a personal tour," *Appl. Opt.* **52**, 45–56 (2013).
94. Y. Shechtman, Y. C. Eldar, O. Cohen, H. N. Chapman, J. Miao, and M. Segev, "Phase retrieval with application to optical imaging: a contemporary overview," *IEEE Signal Process. Mag.* **32**(3), 87–109 (2015).
95. J. Miao, P. Charalambous, J. Kirz, and D. Sayre, "Extending the methodology of x-ray crystallography to allow imaging of micrometre-sized non-crystalline specimens," *Nature* **400**, 342–344 (1999).
96. T. B. Pittman, Y. H. Shih, D. V. Strekalov, and A. V. Sergienko, "Optical imaging by means of two-photon quantum entanglement," *Phys. Rev. A* **52**, R3429–R3432 (1995).

97. R. W. Boyd, K. W. C. Chan, A. Jha, M. Malik, C. O'Sullivan, H. Shin, and P. Zerom, "Quantum imaging: enhanced image formation using quantum states of light," *Proc. SPIE* **7342**, 73420B (2009).
98. M. J. Padgett and R. W. Boyd, "An introduction to ghost imaging: quantum and classical," *Philos. Trans. R. Soc. London A* **375**, 20160233 (2017).
99. J. H. Shapiro and R. W. Boyd, "The physics of ghost imaging," *Quantum Inf. Process.* **11**, 949–993 (2012).
100. R. J. C. Spreeuw, "A classical analogy of entanglement," *Found. Phys.* **28**, 361–374 (1998).
101. B. N. Simon, S. Simon, F. Gori, M. Santarsiero, R. Borghi, N. Mukunda, and R. Simon, "Nonquantum entanglement resolves a basic issue in polarization optics," *Phys. Rev. Lett.* **104**, 023901 (2010).
102. K. H. Kagalwala, G. D. Giuseppe, A. F. Abouraddy, and B. E. A. Saleh, "Bell's measure in classical optical coherence," *Nat. Photonics* **7**, 72–78 (2013).
103. S. Berg-Johansen, F. Töppel, B. Stiller, P. Banzer, M. Ornigotti, E. Giacobino, G. Leuchs, A. Aiello, and C. Marquardt, "Classically entangled optical beams for high-speed kinematic sensing," *Optica* **2**, 864–868 (2015).
104. R. S. Bennink, S. J. Bentley, and R. W. Boyd, "'Two-photon' coincidence imaging with a classical source," *Phys. Rev. Lett.* **89**, 113601 (2002).
105. R. S. Bennink, S. J. Bentley, R. W. Boyd, and J. C. Howell, "Quantum and classical coincidence imaging," *Phys. Rev. Lett.* **92**, 033601 (2004).
106. J. H. Shapiro, "Computational ghost imaging," *Phys. Rev. A* **78**, 061802 (2008).
107. B. R. Frieden, "Optical transfer of the three-dimensional object," *J. Opt. Soc. Am.* **57**, 56–66 (1967).
108. N. Streibl, "Fundamental restrictions for 3-D light distributions," *Optik* **66**, 341–354 (1984).
109. N. Streibl, "Three-dimensional imaging by a microscope," *J. Opt. Soc. Am. A* **2**, 121–127 (1985).
110. D. N. Sitter and W. T. Rhodes, "Three-dimensional imaging: a space invariant model for space variant systems," *Appl. Opt.* **29**, 3789–3794 (1990).
111. J. J. M. Braat and A. J. E. M. Janssen, "Derivation of various transfer functions of ideal or aberrated imaging systems from the three-dimensional transfer function," *J. Opt. Soc. Am. A* **32**, 1146–1159 (2015).
112. M. Minsky, "Microscopy apparatus," U.S. patent 3,013,467 (December 19, 1961).
113. M. Minsky, "Memoir on inventing the confocal scanning microscope," *Scanning* **10**, 128–138 (1988).
114. L. Yu and M. K. Kim, "Wavelength-scanning digital interference holography for tomographic three-dimensional imaging by use of the angular spectrum method," *Opt. Lett.* **30**, 2092–2094 (2005).
115. T.-C. Poon, "Optical scanning holography - a review of recent progress," *J. Opt. Soc. Korea* **13**, 406–415 (2009).
116. T. G. Mayerhöfer, H. Mutschke, and J. Popp, "Employing theories far beyond their limits-the case of the (Boguer-) Beer-Lambert law," *ChemPhysChem* **17**, 1948–1955 (2016).
117. A. Vallebona and V. Maragliano, "Radiography with great enlargement (micro-radiography) and a technical method for the radiographic dissociation of the shadow," *Radiology* **17**, 340–341 (1931).
118. F. Natterer, *The Mathematics of Computerized Tomography, Classics in Applied Mathematics* (SIAM, 2001).
119. G. T. Herman, *Fundamentals of Computerized Tomography: Image Reconstruction from Projection*, 2nd ed. (Springer, 2009).
120. J. Radon, "Über die bestimmung von funktionen durch ihre integralwerte längs gewisser mannigfaltigkeiten," *Berichteüber die Verhandlungen der*

- Königlich-Sächsischen Akademie der Wissenschaften zu Leipzig, Mathematisch-Physische Klasse **69**, 262–277 (1917).
121. J. Radon, “On the determination of functions from their integral values along certain manifolds,” IEEE Trans. Med. Imaging **5**, 170–176 (1986).
  122. Wikipedia, “CT scan,” [https://en.wikipedia.org/wiki/CT\\_scan](https://en.wikipedia.org/wiki/CT_scan).
  123. P. C. Lauterbur, “Image formation by induced local interactions: examples employing nuclear magnetic resonance,” Nature **242**, 190–191 (1973).
  124. P. Mansfield and P. K. Grannell, “Diffraction and microscopy in solids and liquids by NMR,” Phys. Rev. B **12**, 3618–3634 (1975).
  125. E. H. Adelson and J. Y. A. Wang, “Single lens stereo with a plenoptic camera,” IEEE Trans. Pattern Anal. Mach. Intell. **14**, 99–106 (1992).
  126. J. C. Maxwell, “Experiments on colour, as perceived by the eye, with remarks on colour-blindness,” Earth Environ. Sci. Trans. R. Soc. Edinburgh **21**, 275–298 (1857).
  127. B. E. Bayer, “Color imaging array,” U.S. patent 3,971,065 (July 20, 1976).
  128. Wikipedia, “Bayer filter,” [https://en.wikipedia.org/wiki/Bayer\\_filter](https://en.wikipedia.org/wiki/Bayer_filter).
  129. F. Yasuma, T. Mitsunaga, D. Iso, and S. K. Nayar, “Generalized assorted pixel camera: postcapture control of resolution, dynamic range, and spectrum,” IEEE Trans. Image Process. **19**, 2241–2253 (2010).
  130. T.-H. Chao, J. W. Yu, L.-J. Cheng, and J. L. Lambert, “Acousto-optic tunable filter imaging spectrometer for NASA applications: breadboard demonstration,” Proc. SPIE **1347**, 655–663 (1990).
  131. T. Okamoto and I. Yamaguchi, “Simultaneous acquisition of spectral image information,” Opt. Lett. **16**, 1277–1279 (1991).
  132. T. Okamoto, A. Takahashi, and I. Yamaguchi, “Simultaneous acquisition of spectral and spatial intensity distribution,” Appl. Spectrosc. **47**, 1198–1202 (1993).
  133. T. V. Bulygin and G. N. Vishnyakov, “Spectrotomography: a new method of obtaining spectrograms of two-dimensional objects,” Proc. SPIE **1843**, 315–322 (1992).
  134. M. E. Gehm, R. John, D. J. Brady, R. M. Willett, and T. J. Schulz, “Single-shot compressive spectral imaging with a dual-disperser architecture,” Opt. Express **15**, 14013–14027 (2007).
  135. A. A. Wagadarikar, N. P. Pitsianis, X. Sun, and D. J. Brady, “Spectral image estimation for coded aperture snapshot spectral imagers,” Proc. SPIE **7076**, 707602 (2008).
  136. H. Arguello and G. R. Arce, “Code aperture optimization for spectrally agile compressive imaging,” J. Opt. Soc. Am. A **28**, 2400–2413 (2011).
  137. C. V. Correa, H. Arguello, and G. R. Arce, “Snapshot colored compressive spectral imager,” J. Opt. Soc. Am. A **32**, 1754–1763 (2015).
  138. A. Parada-Mayorga and G. R. Arce, “Spectral super-resolution in colored coded aperture spectral imaging,” IEEE Trans. Comput. Imaging **2**, 440–455 (2016).
  139. G. R. Arce, D. J. Brady, H. Arguello, L. Carin, and D. S. Kittle, “Compressive coded aperture spectral imaging: an introduction,” IEEE Signal Process. Mag. **31** (1), 105–115 (2014).
  140. J. Ojeda-Castañeda and C. M. Gómez-Sarabia, “Tuning field depth at high resolution by pupil engineering,” Adv. Opt. Photon. **7**, 814–880 (2015).
  141. G. Häulser and F. Willomitzer, “A stroll through 3D imaging and measurement,” Int. Commission Opt. Newsletter **104**, 1–5 (2015).
  142. F. Willomitzer, S. Ettl, C. Faber, and G. Häusler, “Single-shot three-dimensional sensing with improved data density,” Appl. Opt. **54**, 408–417 (2015).
  143. F. Willomitzer and G. Häusler, “Single-shot 3D motion picture camera with a dense point cloud,” Opt. Express **25**, 23451–23464 (2017).

144. P. Rangarajan, I. Sinharoy, P. Milojkovic, and M. P. Christensen, "Active computational imaging for circumventing resolution limits at macroscopic scales," *Appl. Opt.* **56**, D84–D107 (2017).
145. A. Greengard, Y. Y. Schechner, and R. Piestun, "Depth from diffracted rotation," *Opt. Lett.* **31**, 181–183 (2006).
146. S. Quirin and R. Piestun, "Depth estimation and image recovery using broadband, incoherent illumination with engineered point spread functions," *Appl. Opt.* **52**, A367–A376 (2013).
147. S. R. P. Pavani, A. Greengard, and R. Piestun, "Three-dimensional localization with nanometer accuracy using a detector-limited double-helix point spread function system," *Appl. Phys. Lett.* **95**, 021103 (2009).
148. G. M. Lippmann, "La photographic intégrale," *Compt. Rend. Acad. Sci.* **146**, 446–451 (1908).
149. H. Arimoto and B. Javidi, "Integral three-dimensional imaging with digital reconstruction," *Opt. Lett.* **26**, 157–159 (2001).
150. J.-S. Jang and B. Javidi, "Improved viewing resolution of three-dimensional integral imaging by use of nonstationary micro-optics," *Opt. Lett.* **27**, 324–326 (2002).
151. X. Xiao, B. Javidi, M. Martinez-Corral, and A. Stern, "Advances in three-dimensional integral imaging: sensing, display, and applications," *Appl. Opt.* **52**, 546–560 (2013).
152. R. Ng, M. Levoy, M. Brédif, G. Duval, M. Horowitz, and P. Hanrahan, "Light field photography with a hand-held plenoptic camera," Stanford Tech. Rep. CTSR 2005-02 (2005).
153. R. Ng, "Digital light field photography," Ph.D. thesis (Stanford University, 2006).
154. J. C. Yang, M. Everett, C. Buehler, and L. McMillan, "A real-time distributed light field camera," in *Proceedings of the 13th Eurographics Workshop on Rendering* (2002), pp. 77–86.
155. B. Wilburn, N. Joshi, V. Vaish, E.-V. Talvala, E. Antunez, A. Barth, A. Adams, M. Horowitz, and M. Levoy, "High performance imaging using large camera arrays," *ACM Trans. Graph.* **24**, 765–776 (2005).
156. M. Levoy, "Light fields and computational imaging," *Computer* **39**, 46–55 (2006).
157. J. E. Solomon, "Polarization imaging," *Appl. Opt.* **20**, 1537–1544 (1981).
158. G. P. Nordin, J. T. Meier, P. C. Deguzman, and M. W. Jones, "Micropolarizer array for infrared imaging polarimetry," *J. Opt. Soc. Am. A* **16**, 1168–1174 (1999).
159. P. C. Deguzman and G. P. Nordin, "Stacked subwavelength gratings as circular polarization filters," *Appl. Opt.* **40**, 5731–5737 (2001).
160. T. Colomb, P. Dahlgren, D. Beguin, E. Cuche, P. Marquet, and C. Depeursinge, "Polarization imaging by use of digital holography," *Appl. Opt.* **41**, 27–37 (2002).
161. C. Zhang, B. Zhao, and B. Xiangli, "Wide-field-of-view polarization interference imaging spectrometer," *Appl. Opt.* **43**, 6090–6094 (2004).
162. T. Nomura, B. Javidi, S. Murata, E. Nitanai, and T. Numata, "Polarization imaging of a 3D object by use of on-axis phase-shifting digital holography," *Opt. Lett.* **32**, 481–483 (2007).
163. V. Gruev, J. V. der Spiegel, and N. Engheta, "Dual-tier thin film polymer polarization imaging sensor," *Opt. Express* **18**, 19292–19303 (2010).
164. J. L. Pezzaniti and R. A. Chipman, "Mueller matrix imaging polarimetry," *Opt. Eng.* **34**, 1558–1568 (1995).
165. L. B. Wolff, "Polarization vision: a new sensory approach to image understanding," *Image Vision Comput.* **15**, 81–93 (1997).

166. A. G. Andreou and Z. K. Kalayjian, "Polarization imaging: principles and integrated polarimeters," *IEEE Sens. J.* **2**, 566–576 (2002).
167. L. B. Wolff and A. G. Andreou, "Polarization camera sensors," *Image Vision Comput.* **13**, 497–510 (1995).
168. J. S. Tyo, D. L. Goldstein, D. B. Chenault, and J. A. Shaw, "Review of passive imaging polarimetry for remote sensing applications," *Appl. Opt.* **45**, 5453–5469 (2006).
169. L. Cutrona, W. Vivian, E. Leith, and G. Hall, "A high-resolution radar combat-surveillance system," *IRE Trans. Military Electron.* **MIL-5**, 127–131 (1961).
170. C. A. Wiley, "Pulsed Doppler radar methods and apparatus," U.S. patent 3,196,436 (July 20, 1965).
171. A. Moreira, P. Prats-Iraola, M. Younis, G. Krieger, I. Hajnsek, and K. P. Papathanassiou, "A tutorial on synthetic aperture radar," *IEEE Geosci. Remote Sens. Mag.* **1**(1), 6–43 (2013).
172. J. G. Ables, "Fourier transform photography: a new method for x-ray astronomy," *Publ. Astron. Soc. Aust.* **1**, 172–173 (1968).
173. E. E. Fenimore and T. M. Cannon, "Coded aperture imaging with uniformly redundant arrays," *Appl. Opt.* **17**, 337–347 (1978).
174. Wikipedia, "Coded aperture," [https://en.wikipedia.org/wiki/Coded\\_aperture](https://en.wikipedia.org/wiki/Coded_aperture).
175. R. Accorsi, F. Gasparini, and R. C. Lanza, "A coded aperture for high-resolution nuclear medicine planar imaging with a conventional Anger camera: experimental results," *IEEE Trans. Nucl. Sci.* **48**, 2411–2417 (2001).
176. P. Durrant, M. Dallimore, I. Jupp, and D. Ramsden, "The application of pinhole and coded aperture imaging in the nuclear environment," *Nucl. Instrum. Methods Phys. Res. A* **422**, 667–671 (1999).
177. M. J. Cieślak, K. A. Gamage, and R. Glover, "Coded-aperture imaging systems: past, present and future development: a review," *Radiat. Meas.* **92**, 59–71 (2016).
178. W. Lukosz and M. Marchand, "Optischen abbildung unter Überschreitung der beugungsbedingten auflösungsgrenze," *Opt. Acta* **10**, 241–255 (1963).
179. R. W. Gerchberg, "Super-resolution through error energy reduction," *Opt. Acta* **21**, 709–720 (1974).
180. A. Papoulis, "A new algorithm in spectral analysis and bandlimited extrapolation," *IEEE Trans. Circuits Syst.* **22**, 735–742 (1975).
181. R. J. Marks and D. K. Smith, "Iterative coherent processor for bandlimited signal extrapolation," *Proc. SPIE* **231**, 106–111 (1980).
182. R. J. Marks, "Gerchberg's extrapolation algorithm in two dimensions," *Appl. Opt.* **20**, 1815–1820 (1981).
183. The Royal Swedish Academy of Sciences, "The Nobel Prize in Chemistry 2014 Eric Betzig, Stefan W. Hell, William E. Moerner," [https://www.nobelprize.org/nobel\\_prizes/chemistry/laureates/2014/press.html](https://www.nobelprize.org/nobel_prizes/chemistry/laureates/2014/press.html).
184. E. Betzig, G. H. Patterson, R. Sougrat, O. W. Lindwasser, S. Olenych, J. S. Bonifacino, M. W. Davidson, J. Lippincott-Schwartz, and H. F. Hess, "Imaging intracellular fluorescent proteins at nanometer resolution," *Science* **313**, 1642–1645 (2006).
185. L. Zhu, W. Zhang, D. Elnatan, and B. Huang, "Faster STORM using compressed sensing," *Nat. Methods* **9**, 721–723 (2012).
186. G. Zheng, R. Horstmeyer, and C. Yang, "Wide-field, high-resolution Fourier ptychographic microscopy," *Nat. Photonics* **7**, 739–745 (2013).
187. L. Tian, X. Li, K. Ramchandran, and L. Waller, "Multiplexed coded illumination for Fourier ptychography with an LED array microscope," *Biomed. Opt. Express* **5**, 2376–2389 (2014).
188. M. G. Gustafsson, "Surpassing the lateral resolution limit by a factor of two using structured illumination microscopy," *J. Microsc.* **198**, 82–87 (2000).

189. M. G. L. Gustafsson, "Nonlinear structured-illumination microscopy: wide-field fluorescence imaging with theoretically unlimited resolution," *Proc. Natl. Acad. Sci. USA* **102**, 13081–13086 (2005).
190. M. A. Thompson, M. D. Lew, and W. Moerner, "Extending microscopic resolution with single-molecule imaging and active control," *Ann. Rev. Biophys.* **41**, 321–342 (2012).
191. A. Levin, P. Sand, T. S. Cho, F. Durand, and W. T. Freeman, "Motion-invariant photography," *ACM Trans. Graph.* **27**, 71 (2008).
192. Y. Bando, B.-Y. Chen, and T. Nishita, "Motion deblurring from a single image using circular sensor motion," *Comput. Graph. Forum* **30**, 1869–1878 (2011).
193. R. Raskar, A. Agrawal, and J. Tumblin, "Coded exposure photography: motion deblurring using fluttered shutter," *ACM Trans. Graph.* **25**, 795–804 (2006).
194. D. Tseng, O. Mudanyali, C. Oztoprak, S. O. Isikman, I. Sencan, O. Yaglidere, and A. Ozcan, "Lensfree microscopy on a cellphone," *Lab Chip* **10**, 1787–1792 (2010).
195. A. Ozcan and E. McLeod, "Lensless imaging and sensing," *Ann. Rev. Biomed. Eng.* **18**, 77–102 (2016).
196. J. Tanida, T. Kumagai, K. Yamada, S. Miyatake, K. Ishida, T. Morimoto, N. Kondou, D. Miyazaki, and Y. Ichioka, "Thin observation module by bound optics (TOMBO): concept and experimental verification," *Appl. Opt.* **40**, 1806–1813 (2001).
197. R. Athale, D. M. Healy, D. J. Brady, and M. A. Neifeld, "Reinventing the camera," *Opt. Photon. News* **19**(3), 32–37 (2008).
198. Light, "The light L16 camera," <https://light.co/>.
199. R. J. Plemmons, S. Prasad, S. Matthews, M. Mirotznik, R. Barnard, B. Gray, V. P. Pauca, T. C. Torgersen, J. van der Gracht, and G. Behrmann, "PERIODIC: integrated computational array imaging technology," in *Computational Optical Sensing and Imaging* (Optical Society of America, 2007), paper CMA1.
200. D. B. Cavanaugh, M. Dombrowski, and B. Catanzaro, "Spatially corrected full-cubed hyperspectral imager," U.S. patent 7,433,042 (October 7, 2008).
201. R. Horstmeyer, G. Euliss, and R. Athale, "Flexible multimodal camera using a light field architecture," in *IEEE International Conference on Computational Photography* (2009).
202. P. G. Van Dokkum, R. Abraham, and A. Merritt, "First results from the dragonfly telephoto array: the apparent lack of a stellar halo in the massive spiral galaxy M101," *Astrophys. J. Lett.* **782**, L24 (2014).
203. D. J. Brady, M. E. Gehm, R. A. Stack, D. L. Marks, D. S. Kittle, D. R. Golish, E. Vera, and S. D. Feller, "Multiscale gigapixel photography," *Nature* **486**, 386–389 (2012).
204. A. V. Lutg, "Signal detection by complex spatial filtering," *IEEE Trans. Inf. Theory* **10**, 139–145 (1964).
205. J. R. Leger and S. H. Lee, "Coherent optical implementation of generalized two-dimensional transforms," *Opt. Eng.* **18**, 518–523 (1979).
206. J. R. Leger and S. H. Lee, "Hybrid optical processor for pattern recognition and classification using a generalized set of pattern functions," *Appl. Opt.* **21**, 274–287 (1982).
207. M. A. Neifeld and P. Shankar, "Feature-specific imaging," *Appl. Opt.* **42**, 3379–3389 (2003).
208. E. J. Candes, J. K. Romberg, and T. Tao, "Stable signal recovery from incomplete and inaccurate measurements," *Commun. Pure Appl. Math.* **59**, 1207–1223 (2006).
209. D. L. Donoho, "Compressed sensing," *IEEE Trans. Inf. Theory* **52**, 1289–1306 (2006).

210. M. F. Duarte, M. A. Davenport, D. Takbar, J. N. Laska, T. Sun, K. F. Kelly, and R. G. Baraniuk, "Single-pixel imaging via compressive sampling," *IEEE Signal Process. Mag.* **25**(2), 83–91 (2008).
211. M. Lustig, D. L. Donoho, J. M. Santos, and J. M. Pauly, "Compressed sensing MRI," *IEEE Signal Process. Mag.* **25**(2), 72–82 (2008).
212. H. W. Babcock, "The possibility of compensating astronomical seeing," *Publ. Astron. Soc. Pac.* **65**, 229–236 (1953).
213. Thorlabs, "AO tutorial," <https://www.thorlabs.com/tutorials.cfm?tabID=96a6f477-757e-43fa-9772-5a83e1acf6c1>.
214. M. P. Christensen, G. W. Euliss, M. J. McFadden, K. M. Coyle, P. Milojkovic, M. W. Haney, J. van der Gracht, and R. A. Athale, "Active-eyes: an adaptive pixel-by-pixel image-segmentation sensor architecture for high-dynamic-range hyperspectral imaging," *Appl. Opt.* **41**, 6093–6103 (2002).
215. M. P. Christensen, V. Bhakta, D. Rajan, T. Mirani, S. C. Douglas, S. L. Wood, and M. W. Haney, "Adaptive flat multiresolution multiplexed computational imaging architecture utilizing micromirror arrays to steer subimager fields of view," *Appl. Opt.* **45**, 2884–2892 (2006).
216. M. Somayaji, M. P. Christensen, E. Faramarzi, D. Rajan, J.-P. Laine, P. Sebelius, A. Zachai, M. Chaparala, G. Blasche, K. Baldwin, B. Ogunfemi, and D. Granquist-Fraser, "Prototype development and field-test results of an adaptive multiresolution PANOPTES imaging architecture," *Appl. Opt.* **51**, A48–A58 (2012).
217. A. T. Watnik and P. S. Lebow, "Dynamic holography for extended object beam shaping," *Proc. SPIE* **8843**, 88430E (2013).
218. A. T. Watnik and P. S. Lebow, "Limits of bootstrapping in a weak-signal holographic conjugator," *Appl. Opt.* **53**, 3841–3847 (2014).
219. A. T. Watnik and P. S. Lebow, "Weak-signal iterative holography," *Appl. Opt.* **54**, 2615–2619 (2015).
220. P. S. Lebow, A. T. Watnik, and J. R. Lindle, "Gated holographic imaging for structured illumination through obscurations," *Opt. Lett.* **42**, 2543–2546 (2017).
221. M. E. Gehm and D. J. Brady, "Compressive sensing in the EO/IR," *Appl. Opt.* **54**, C14–C22 (2015).
222. J. N. Mait, A. Mahalanobis, M. A. Neifeld, and R. A. Athale, "Compressive sensing focus issue: introduction," *Appl. Opt.* **54**, CS1–CS3 (2015).
223. W. S. Parker, "An instrument for what? Digital computers, simulation and scientific practice," *Spontaneous Gener.* **4**, 39–44 (2010).
224. J. Miao, T. Ishikawa, I. K. Robinson, and M. M. Murnane, "Beyond crystallography: diffractive imaging using coherent x-ray light sources," *Science* **348**, 530–535 (2015).
225. R. Karl, C. Bevis, R. Lopez-Rios, J. Reichanadter, D. Gardner, C. Porter, E. Shanblatt, M. Tanksalvala, G. F. Mancini, M. Murnane, H. Kapteyn, and D. Adams, "Spatial, spectral, and polarization multiplexed ptychography," *Opt. Express* **23**, 30250–30258 (2015).
226. J. N. Mait, D. A. Wikner, M. S. Mirotznik, J. van der Gracht, G. P. Behrmann, B. L. Good, and S. A. Mathews, "94-GHz imager with extended depth of field," *IEEE Trans. Antennas Propag.* **57**, 1713–1719 (2009).
227. C. F. Cull, D. A. Wikner, J. N. Mait, M. Mattheiss, and D. J. Brady, "Millimeter-wave compressive holography," *Appl. Opt.* **49**, E67–E82 (2010).
228. J. N. Mait, C. Harrity, R. D. Martin, C. A. Schuetz, S. Shi, and D. W. Prather, "Minimum bias image processing with a distributed-aperture millimeter-wave imager," *Appl. Opt.* **56**, A52–A61 (2017).

229. G. Leifman, T. Swedish, K. Roesch, and R. Raskar, "Leveraging the crowd for annotation of retinal images," in *37th Annual International Conference of the IEEE Engineering in Medicine and Biology Society* (2015), pp. 7736–7739.
230. M. Testorf, B. Hennelly, and J. Ojeda-Castaneda, *Phase-Space Optics: Fundamentals and Applications* (McGraw-Hill, 2009).
231. R. A. Shelby, D. R. Smith, and S. Schultz, "Experimental verification of a negative index of refraction," *Science* **292**, 77–79 (2001).
232. J. B. Pendry, "Negative refraction," *Contemp. Phys.* **45**, 191–202 (2004).
233. J. B. Pendry, D. Schurig, and D. R. Smith, "Controlling electromagnetic fields," *Science* **312**, 1780–1782 (2006).
234. U. Leonhardt, "Optical conformal mapping," *Science* **312**, 1777–1780 (2006).
235. O. Tzang, A. Agrawal, and R. Piestun, "Materials degrees of freedom for optical design," in *Imaging and Applied Optics (3D, AIO, COSI, IS, MATH, pcAOP)* (Optical Society of America, 2017), paper IW3E.3.
236. D. J. Brady, *Optical Imaging and Spectroscopy* (Wiley, 2009).
237. K. Khare, *Fourier Optics and Computational Imaging* (Wiley, 2015).
238. IEEE, "IEEE Transactions on Computational Imaging," <http://ieeexplore.ieee.org/servlet/opac?punumber=6745852>.



**Joseph Mait** has been with the U.S. Army Research Laboratory and its predecessor organizations since 1988. From 2013 to 2017, he was the laboratory's Chief Scientist, responsible for technical forecasting and strategic planning. Prior to his government career, he was an assistant professor of Electrical Engineering at the University of Virginia. He has held visiting positions at the Lehrstuhl für Angewandte Optik, Universität Erlangen-Nürnberg, Germany, the Center for Technology and National Security Policy at the National Defense University in Washington D.C., and the Leibniz Institute for Photonic Technologies, Jena, Germany. His research interests include diffractive optics, graded-index optics, and computational imaging. He received his BSEE from the University of Virginia in 1979 and his MSEE and Ph.D. from the Georgia Institute of Technology in 1980 and 1985, respectively. He is a Fellow of SPIE and The Optical Society (OSA), and a senior member of IEEE. From 2009-2015, he was Editor-in-Chief of *Applied Optics*.



**Gary Euliss** currently works at the MITRE Corporation in McLean, Virginia, as a Principal Scientist with the Computational Imaging and Sensing group in the Emerging Technologies department. In this role, he has been responsible for leading and supporting a number of activities in the development of unconventional sensor architectures, ranging from initial conceptualization to prototype demonstration. From 1994 to 2001, he worked as a Physicist at the U.S. Army Research Laboratory where his research interests included optics, microphotonics, optical processing, and imaging. This is also where he developed an interest in Computational Imaging, including information theoretic design and optimization of imaging systems. After leaving ARL, he worked for a short time at Applied Photonics and continued to do research in computational imaging as well as optical interconnects for high-performance computing. He received a B.S. in Physics from Missouri State University, a M.S. in Physics from Kansas State University, and a Ph.D. in Information Technology with an emphasis in Electrical Engineering from George Mason University.



**Ravi Athale** was a Program Officer at the Office of Naval Research (ONR) when this work was prepared. At ONR, he managed research in imaging sensors, optical computing, and nanophotonics. He received his Ph.D. in Electrical Engineering from UC San Diego in 1980. Prior to ONR, he held research, teaching, and program management positions at the Naval Research Laboratory, BDM Corporation, George Mason University, DARPA, and MITRE Corporation. His research and programmatic interests are optical processing, optical interconnects, nanophotonics, and imaging sensors. He is a Fellow of The Optical Society (OSA) and received OSA's Leadership Award, and the Secretary of Defense Medal for Exceptional Public Service.